



UNIVERSITÀ
DEGLI STUDI
DI PADOVA

Sede Amministrativa: Università degli Studi di Padova

Dipartimento di Ingegneria dell'Informazione

SCUOLA DI DOTTORATO DI RICERCA IN INGEGNERIA DELL'INFORMAZIONE

INDIRIZZO: SCIENZA E TECNOLOGIA DELL'INFORMAZIONE

CICLO: XXX

High Efficiency Interfacing Converters for Distributed Energy Systems

Direttore della Scuola: Ch.mo Prof. Andrea Neviani

Supervisore: Ch.mo Prof. Giorgio Spiazzi

Dottorando: Davide Biadene



UNIVERSITÀ
DEGLI STUDI
DI PADOVA

Head Office: Università degli Studi di Padova

Department of Information Engineering

PH.D. COURSE ON INFORMATION ENGINEERING

SECTION: INFORMATION AND COMMUNICATION TECHNOLOGIES (I.C.T.)

CYCLE: XXX

High Efficiency Interfacing Converters for Distributed Energy Systems

Coordinator: Ch.mo Prof. Andrea Neviani

Supervisor: Prof. Giorgio Spiazzi

Ph.D. Candidate: Davide Biadene

Contents

List of Acronyms	iii
List of Figures	vii
List of Tables	ix
Abstract	xi
Acknowledgments	xv
1 Introduction	1
1.1 Distributed Energy Systems	2
1.2 Dissertation Outline	5
2 Development Methodology and Tool	7
2.1 Multi-Objective Optimization and Pareto Optimum	8
2.1.1 MOO Solving Methods	13
2.2 MOOP in EPC Design	16
2.3 Summary	19
3 Theoretical and Technical Background	21
3.1 Magnetic Device Losses	23
3.1.1 Core Loss Modelling	23
3.1.2 Winding Loss Modelling	26
3.2 Semiconductor Device Losses	26

3.2.1	LH Transition	27
3.2.2	HL Transition	29
3.3	Summary	30
4	Steady-State Converter Analysis	33
4.1	Generalized State-Space Model	35
4.1.1	Sampled Steady-State Trajectories	35
4.1.2	Normalized Output Power	39
4.1.3	Voltage Conversion Ratio	42
4.1.4	General Considerations	42
4.2	Case Study 1: PSM SR DHB Converter	43
4.2.1	Functional Description	43
4.2.2	State-Space Analysis	43
4.3	Case Study 2: IBCI Converter	46
4.3.1	Functional Description	47
4.3.2	State-Space Analysis	48
4.3.3	Simulations and Experimental Verification	61
4.4	Summary	63
5	Test Case	67
5.1	Multi-Cell SST	67
5.2	PFC Boost Optimization	70
5.2.1	MV-DC Link	70
5.2.2	Boost Inductor	72
5.2.3	Switching Device Losses	81
5.2.4	Magnetic Device Losses	91
5.2.5	Thermal Management	102
5.3	Pareto Analysis	102
5.4	Summary	107
6	Conclusions	109

List of Acronyms

AC Alternate Current

AM Amplitude Modulation or Modulated

CCM Continuous Conduction Mode

CCM Discontinuous Conduction Mode

DC Direct Current

DER Distributed Energy Resource

DHB Dual Half Bridge

DS Design Space

EPC Electronic Power Converter

ES Energy Storage

FHA First Harmonic Approximation

FM Frequency Modulation or Modulated

FPGA Field Programmable Gate Array

GSE Generalized Steinmetz Equation

HV High-Voltage

i²GSE improved iGSE

IBCI Interleaved Boost with Coupled Inductors

ICT Information and Communication Technology

iGSE improved Generalized Steinmetz Equation

LV Low-Voltage

MOO Multi-Objective Optimization

MPPT Maximum Power Point Tracking

MSE Modified Steinmetz Equation

MV Medium-Voltage

PFC Power Factor Correction

PSM Phase Shift Modulation or Modulated

PV Photo-voltaic

PWM Pulse Width Modulation or Modulated

PWMD Digital Pulse Width Modulation

RMS Root Mean Square

SE Steinmetz Equation

SPA State Space Analysis

SRC Series Resonant Converter

SST Solid State Transformer

UPS Uninterruptible Power Supply

VHDL VHSIC Hardware Description Language

VHSIC Very High Speed Integrated Circuits

ZCS Zero Current Switching

ZVS Zero Voltage Switching

List of Figures

1.1	Conceptual smart grid system	3
1.2	Distributed Energy System scheme	4
2.1	Multi-Objective Optimization Concept	11
2.2	Simple example of MOOP: Feasible Region	12
2.3	Simple example of MOOP: Objective Space and Pareto Front	13
2.4	Typical MOOP Solving Methods	16
2.5	MOOP in EPC Design	18
3.1	Hysteresis in magnetic components	24
3.2	Equivalent circuit for the Switching Loss estimation	27
3.3	Equivalent LH Transition Model	29
4.1	Generalized DC-DC conversion involving a current shaping impedance	34
4.2	Generalized DC-DC Series Resonant Converter	35
4.3	Angle convention	38
4.4	Scheme and main waveforms of SR PSM DHB converter	43
4.5	Current comparison between FHA and SPA models of PSM SR DHB	44
4.6	Power comparison between FHA and SPA models of PSM SR DHB	46
4.7	Interleaved Boost with Couple Inductors (IBCI)	47
4.8	Main converter waveforms of IBCI converter	49
4.9	CCM ₁ operating region	54
4.10	Current waveforms at phase <i>a</i> in CCM ₁ mode	60
4.11	Mutual inductor models	62

4.12	Operating regions obtained via simulation	64
4.13	Theoretical and experimental voltage conversion ratio	64
5.1	Multi-cell SST configuration	68
5.2	Structure of the IBE-based Multi-Cell SST	69
5.3	Power flow in a IBE-based SST cell	71
5.4	Modulation scheme of IBE-based multi-cell SST	74
5.5	Main waveforms of IBE SST	76
5.6	Phasor description of input SST quantities	77
5.7	SST input voltage and current waveforms in a switching period	77
5.8	Comparison between $\Delta I_{g,r}$ and $\Delta I_{g,e}$	78
5.9	Grid current ripple the approximated envelope	79
5.10	Boost Inductor Current Spectrum	80
5.11	Boost Inductor Value L_g	81
5.12	iTCM modulation scheme	82
5.13	Main waveforms of iTCM	83
5.14	Normalized current and voltage waveforms in the ZVS impedance	84
5.15	Sign of the normalized current J_0	85
5.16	Local stationary points of j_L in the (d, F) -plane	86
5.17	Local stationary points of u_C in the (d, F) -plane	89
5.18	Conduction and switching losses in the considered design space	92
5.19	Inductor Base Model	93
5.20	Geometry of the base inductor model	93
5.21	Magnetic core paths in a E-core	95
5.22	Closed line integral of the magnetic field H	98
5.23	Pareto Front of ZVS Inductor design	101
5.24	Pareto Analyses of overall SST PFC Boost Stage	104
5.25	Pareto Fronts of overall SST PFC Boost Stage	106

List of Tables

4.1	Base and Normalized Variable Definitions	35
4.2	Definition of $\mathbf{q}_A, \mathbf{q}_B$ and δ_i for SR PSM DHB	44
4.3	Definition of $\mathbf{q}'_A, \mathbf{q}'_B$ and δ_i for CCM ₁ mode	51
4.4	Voltage and power mode boundaries definitions of λU_g and Γ	55
4.5	Initial state \mathbf{x}_0 for CCM _{<i>i</i>} , DCM _{<i>i</i>} modes	57
4.6	CCM mode regions and $\lambda U_g/\Gamma$ -boundaries	58
4.7	DCM mode regions and $\lambda U_g/\Gamma$ -boundaries	58
4.8	Normalized power Γ for CCM _{<i>i</i>} , DCM _{<i>i</i>} modes	59
4.9	Characteristic angles φ_i, α_i for CCM _{<i>i</i>} , DCM _{<i>i</i>} modes	59
4.10	Switching node current at LH and HL transitions	61
4.11	Prototype parameters	63
5.1	IBE-based Multi-Cell SST specifications	70
5.2	Maximum harmonic current amplitude limit	72
5.3	Definition of $U_{Z,i}$ and δ_i for ZVS impedance	83

Abstract

The ever-growing amount of renewable energy sources connected to the grid call for a revision of the traditional concept of energy distribution network. In addition, the world climate change issue is becoming a major task for the green energy technology development in the last decades. In the last years, the *smart grids* are the promising paradigm shift for the low- and medium-voltage grids. The term smart grid indicates the symbiosis of the traditional distribution network with a deeply branched ICT infrastructure. The fundamental benefits of this cooperation is an increase in efficiency, reliability and stability of the whole electrical system, and a minimization of the costs and environmental impacts. The main differences with respect to the traditional distribution grid are the growing arrays of customer-sited distributed energy resources (DERs), including renewable energy sources and storage systems, instead of the large and centralized power plants present in the traditional grid. To control and monitor the overall grid system, the ICT infrastructure must be able to manage the present agents, i.e. DERs, and the latter need to be interfaced with the distribution network through Electronic Power Converters (EPCs) forming a micro-, nano-, pico-grid according to the geographical extension. A typical example of pico-grid is a smart building: renewable energy sources, e.g. photovoltaic (PV) panel or wind generator, and energy storage systems, e.g. battery and/or supercapacitor, are connected together through a common DC Link bus. The interface between DERs and DC Link is demanded to EPCs that manage the power flow, optimize the source utilization or the time-profile generation via the energy storage. The power transfer, besides taking place among the connected DERs, can occur between the DC link and the grid through an AC/DC converter (inverter).

The main aim of the presented work is to look into the EPC design procedure to achieve a deep integration of DERs in the future smart grid. To this end, the efficiency and the

power density are considered the main performance indices to achieve a more effective EPC design.

Since the design process involves the optimization of many performance indices, the first part of this work is dedicated to a general overview of Multi-Objective Optimization problem is discussed to provide the sufficient theoretical background to handle with new methodology. Initially, an example of application of MOO is presented to introduce the notation and show the methodology in a simple case, then the EPC optimization is included.

The central part of the dissertation focuses on the needed background to allow a proper converters modelling. The considered objectives, i.e. efficiency and power density of the considered EPC, are related to the losses, that occurs during the power transfer in the EPC, and the final volume of the converter. Because of this, the estimation of the losses and volume for each electronic components of EPC becomes mandatory. However, the choice of the accuracy of the models used to predict losses and volume is a degree of freedom, since it greatly impacts on computational time. Since this approach is considered in this dissertation a first valuation to make comparison between innovative solutions and the state of the art, the models consider only the main contribution of each loss phenomenon and the main volume contributions. In this way, the MOO analysis doesn't become a high time- and data-consumption tool. The series resonant converters will be treated in detail because of their many advantages: inherent short circuit protection, higher operation frequency, lower electromagnetic interferences and soft-switching modulation. An innovative mathematical framework is proposed for their steady-state analysis, providing the closed-form solutions of the sampled resonant impedance state, the voltage conversion ratio and the transferred power in a single matrix formulation. This tool has been validated by means of a high efficiency DC/DC topology for renewable source interfacing: the Interleaved Boost with Coupled Inductors (IBCI). The proposed framework has allowed to identify six different operating modes providing the closed-form expressions of the voltage conversion ratios and the operating boundaries. Furthermore, the sampled state variable trajectories lays out some soft switching considerations. The testcase demonstrates the effectiveness of the proposed method also with complex topologies avoiding simulation-based or approximated analysis.

In the latter part of the work, the input stage of an AC/DC converter is presented to validate the usage of the MOO approach: the Power Factor Correction (PFC) Boost stage design in a Medium Voltage Solid State Transformer . The analysis is carried out to obtain the concrete benefits introduced by the implementation of a proposed solution to reduce the losses in the switches.

Acknowledgments

I wish to thank, first and foremost, my supervisors Prof. Giorgio Spiazzi for his invaluable support during my Ph.D. studies. Without his guidance and persistent help this dissertation would not have been possible. Moreover, his method and patience have been crucial for my personal and technical growth.

I would like to show my warm thank to all the people of the Power Electronics Group of the University of Padova, Prof. Paolo Tenti, Prof. Paolo Mattavelli, Prof. Simone Buso, Prof. Luca Corradini, Prof. Leopoldo Rossetto, and Dr. Marco Stellini for their helpful suggestions.

Special thanks go also to my Ph.D. colleagues Tommaso Caldognetto, Luca Scandola, Stefano Lissandron, Francesco Bez, Stefano Marconi, Eslam Abdelhamid, Qing Liu, with whom I have had the pleasure to share this experience.

My gratitude goes also to my dear classmates Tommaso Caldognetto and Francesco Cavazzana, who have been a constant and pleasant presence in all the phases of my University experience.

I want also to express my gratitude to all the people of the Power Electronic Systems Laboratory of the Department of Information Technology and Electrical Engineering, ETH Zurich, Switzerland. In particular, to the Director of the PES Laboratory, Prof. Dr. Johann Walter Kolar for giving me the possibility of taking part to such a stimulating environment like is their research group. Also I would like to thank all the very dedicated research assistants, Ph.D and master students with whom I could collaborate, in particular, Dr. Jonas Huber and Dr. Daniel Rothmund. A special thanks to Monica Kohn for giving me all the helps I needed during my visiting period.

Finally, endless thanks to my Mom, Dad and Grandma, family members and friends,

without whom I was nothing; they not only assisted me financially but also extended their support morally and emotionally.

Chapter 1

Introduction

The term electrical power system indicates the technological infrastructure is given over to generating, distributing, storing, and using the electric power. The traditional distribution grid is characterized by a hierarchical structure: all the distribution grid branches grow out from few large power plants, which are demanded the power generation and storage. In this kind of systems, the energy reliability is only ensured through high-level connection redundancies, over-designed infrastructures, controlled system reconfigurations, using electromechanics switches, and protections. Furthermore, the system stability is demanded to the conspicuously slow dynamics of the sources: grid frequency is kept constant by mechanical inertia of the rotating synchronous generators in AC systems, while DC voltage is anchored through batteries in DC systems. These key points of the traditional distribution grid makes the latter to be inherently slow, inefficient, and unreliable [1].

In addition, the world climate change issue is putting pressure on the decarbonization process to reduce drastically the CO_2 emissions mostly produced by electric power sector. For this reason, a boost was given to entire scientific community and national governments to achieve the Paris Agreement's goals that are aligned with the existing technical background, in principle. The most feasible and promising concept has been identified in the *smart grid*. The term smart grid indicates the cooperation between the traditional distribution network with a deeply branched ICT infrastructure to increase the efficiency, reliability and stability of the whole electrical infrastructure, and the minimization of the costs and environmental impacts. A smart grid not only collects the centralised power plants of the

traditional power system, but also the array of customer-sited Distributed Energy Resources (DERs), i.e. both source and storage. Given the opportunity to local control each DER within the grid, optimization techniques can be applied to optimise the use of grid assets, e.g. in terms of power capacity, transient power response and renewable source generation profile [2]–[3]. A first example was reported in [1] by means of the AC-DC mixed hierarchical structure depicted in Fig. 1.1. To achieve so high-level of distributed control required in the smart grid scenario, [1] proposed to interface each DERs and each grid layer with Energy Control Centers (ECCs). An ECC is essentially composed by an Electronic Power Converter (EPC) and remote-controlled breaker. The ECC carries out the communication tasks with the power utility operator providing information about the connected DER or the power flow from/toward the connected grid, to allow an overall description of the grid state quality.

In the next section, the Distributed Energy Systems are described more in detail to provide the operating scenario where this dissertation focusses on.

1.1 Distributed Energy Systems

The term Distributed Energy System (DES) represents a varied array of generation, storage and energy monitoring and control solutions. DES categories encompass power generation, combined heat and power, and energy storage, including the exploitation of electric vehicles [2]–[4]. The even-growing penetration of grid-tie renewable energies in the low-voltage distribution system, mainly photovoltaic and wind power, represents a starting point of DES implementation, but it is still far from taking full advantage of the DES potential due to the lacking ICT infrastructure. In addition to their energetic relevance, DESs represent also an excellent opportunity for society growing in off-grid rural areas, especially where communities depend on expensive, unsustainable fossil fuels to generate electricity.

A concrete and already implemented DES can be depicted by smart building depicted in Fig. 1.2: renewable sources, like photovoltaic (PV) panels, micro wind turbine (μ WT) and fuel cells (FC), are connecting together with different kinds of energy storage (ES) system, e.g. battery and/or supercapacitor stacks, by means of a DC Link bus, typically

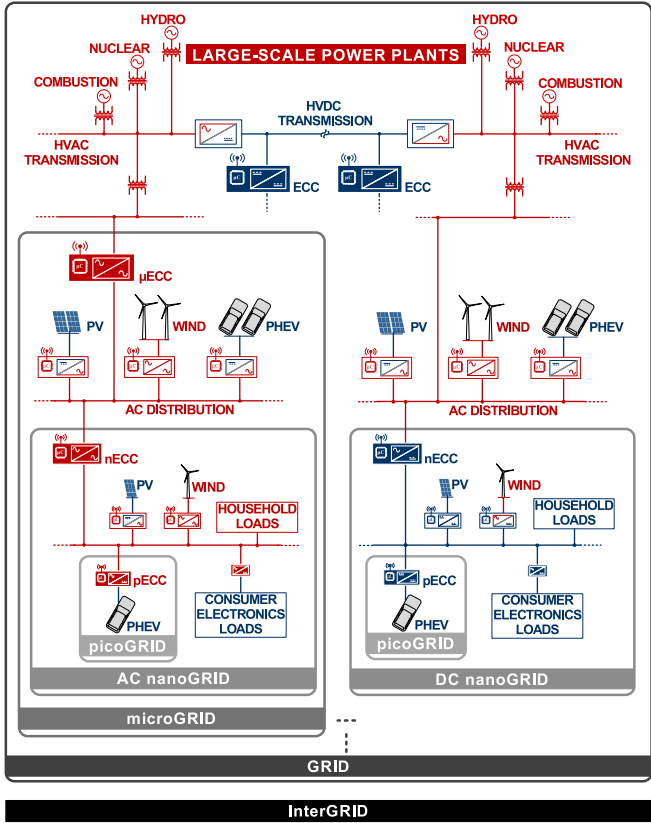


Figure 1.1: Conceptual smart grid system composed by a hierarchically interconnected AC and DC sub-grids [1].

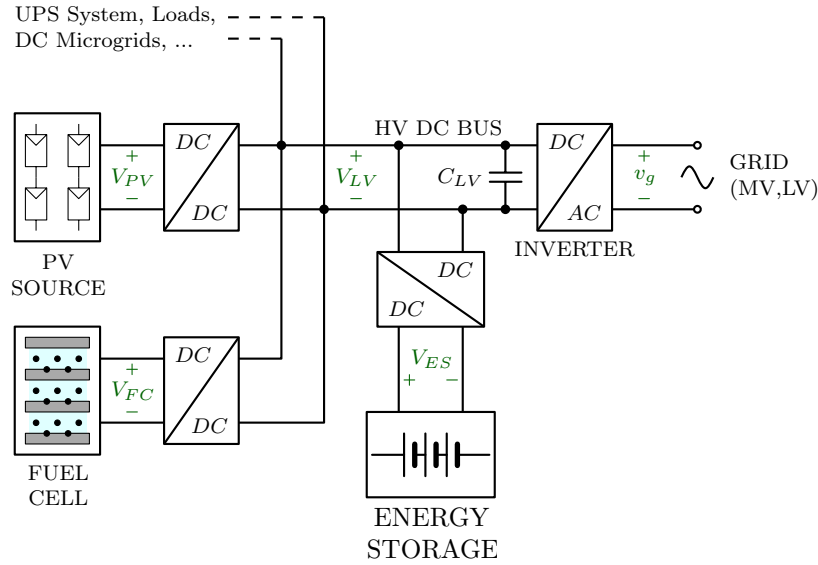


Figure 1.2: Distributed Energy System scheme (Smart Building).

operating at high voltage ($\simeq 400\text{V}$). The PV,FC and ES systems are characterized to be Low Voltage (LV), high current DC devices, so they need to be interfaced via high step-up DC/DC converters to the HV DC Link. On the other hand, μWT can be or a LV-DC source needing a DC/DC converter too, or a variable-frequency HV-AC source requiring an AC/DC converter to be interfaced. The power transfer takes place among the connected DERs, exchanging the available renewable power and the stored one, and the grid through an AC/DC converter (inverter).

This local distribution structure permits also to implement or be connected to a DC micro grid. The achieved benefits can be summered in a reliability, robustness and efficiency gain. The latter can be highlighted when DC loads are connected directly to the DC Link bus via a single stage DC/DC converter avoiding the further AC/DC conversion step.

The afore described structure makes a widespread usage of EPC converter to interface and control each connected DER unit. For this reason is mandatory to deal with EPC design in order to make DES implementation easier. The main figures of merit characterizing the EPCs and affecting their spread could be recognized by efficiency, power density and cost. However the last index is not easier to take into account so could be useful making the simplistic assumption that is inverse proportional to the power density due a better exploitation of EPC components. The following work focusses on the simultaneously optimization

of the identified figures of merit in EPC design with the aim to achieve a feasible design methodology.

1.2 Dissertation Outline

The dissertation includes six chapters. The current chapter, Ch. 1, introduces the scenario where the work is settled, i.e. in a Distributed Energy System, highlighting which are the potential benefits and how a rapid diffusion of DES technologies can be reached optimizing the different figures of merit in EPC design. In Ch. 2 is described the mathematical framework used to simultaneously optimize different tasks. It is a well-know problem of Game Theory that has been extensively treated along the last centuries. Besides the basic concept, the most common solving methods are described and, finally, the concept relocation is done moving toward the power system design. The EPC optimization process goes through the estimation of the losses and volume of the converter components. For this reason, in Ch. 3, the main loss phenomena in a converter are analysed recalling also their modelling. However, the component models need to know which are the electrical quantities, i.e. voltage and current, in the considered topologies. A particular and detailed study is proposed for the Series Resonant Converters (SRC) because their own inherent advantages. The Ch. 4 described a matrix formulation of the well-know analysis approach for the SRC, i.e. the State Plane analysis. The illustrated framework provides a fast computation tool avoiding simulation- or approximation-based approaches. The topics so far treated, are used in the Ch. 5 where the optimization of the input stage of a Solid State Transformer is discussed. The design procedure shows the several modelling steps that occur during the optimization problem definition. Finally, Ch. 6 reports the conclusions of the herein work.

Chapter 2

Development Methodology and Tool

The aim of this dissertation is to explore the EPC design optimization in the distributed energy system scenario. As before mentioned, the optimization process involves more than one objective that requires to find a trade-off between the considered performance indices. This problem concerns a branch of the Game Theory, precisely the multi-criteria decision-making. One of the first researcher in this field was Vilfredo Pareto (1848-1923), an Italian engineer, economist and sociologist. He started to treat economic problems with mathematical tools for the first time in the history, and while he was having the Chair of Political Economy at the University of Lausanne in Switzerland, he developed one of his most famous theories: the Pareto Optimum.

This chapter describes his methodology regarding Multi-Objective Optimization Problem (MOOP) providing, in the first section, the theoretical framework to get used with the basic concept and the specific terminology. The illustrated theory is so applied to the EPC design in the next chapter, specially in Ch. 5. To cope with the complexity of MOOP, the precision level of the several models needed to describe the power converter behaviour must be considered in term of time- and data-consumptions. Often, the huge amount of data produced by this approach can lead the designer far from having a good grasp of the key points in the design process. Hence the potential benefits arising from a widespread design comparison could be a limitation as well.

2.1 Multi-Objective Optimization and Pareto Optimum

Many engineering branches have to deal with Multi-Objective Optimization Problems (MOOPs): in automotive or aeronautics applications, for example, resilience, volume and weight are few of the involved cost functions that engineers have to monitor simultaneously and find a trade-off to achieve the standards. An analytic formulation to handle this problems is described in [5]–[6], the definition of MOOP is given as follow:

Definition 1 (Multi-Objective Optimization Problem). *The MOOP is defined as*

$$\begin{array}{ll} \underset{\mathbf{x}}{\text{minimize}} & \mathbf{y} = \mathbf{f}(\mathbf{x}) \\ \text{subject to} & \mathbf{g}(\mathbf{x}) \leq 0, \quad \mathbf{h}(\mathbf{x}) = 0, \quad \mathbf{x}^L \leq \mathbf{x} \leq \mathbf{x}^H, \end{array}$$

where

$\mathbf{x} = [x_1, x_2, \dots, x_n] \in \mathbb{X}$ is a decision vector in the Decision Space \mathbb{X} ,

$\mathbf{y} = [y_1, y_2, \dots, y_m] \in \mathbb{Y}$ is a objective vector in the Objective Space \mathbb{Y} ,

$\mathbf{f}(\mathbf{x}) = [f_1(\mathbf{x}), f_2(\mathbf{x}), \dots, f_m(\mathbf{x})]$ is the objective function $f : \mathbb{X} \mapsto \mathbb{Y}$,

$\mathbf{g}(\mathbf{x}) = [g_1(\mathbf{x}), g_2(\mathbf{x}), \dots, g_p(\mathbf{x})]$ describes the inequality constrained space,

$\mathbf{h}(\mathbf{x}) = [h_1(\mathbf{x}), h_2(\mathbf{x}), \dots, h_q(\mathbf{x})]$ describes the equality constrained space,

$\mathbf{x}^{L,H} = [x_1^{L,H}, x_2^{L,H}, \dots, x_n^{L,H}] \in \mathbb{X}$ is the vector of lower/upper bound.

As described in Defn. 1, the MOOP maps through the function \mathbf{f} the decision vector \mathbf{x} in related objective vectors \mathbf{y} as depicted in Fig. 2.1. The given constraints over the Decision Space \mathbb{X} identifies the following subset:

Definition 2 (Feasible Set). *The Feasible Set $\mathbb{S} \subseteq \mathbb{X}$ (or Feasible Region) is defined as the set of decision vectors that satisfy all the equality and inequality constraints and the decision variable bounds:*

$$\mathbb{S} = \{ \mathbf{x} \in \mathbb{X} \mid \mathbf{g}(\mathbf{x}) \leq 0 \wedge \mathbf{h}(\mathbf{x}) = 0 \wedge x_1^L \leq x_i \leq x_i^H \forall i = 1, \dots, n \}$$

In other words, the Feasible Set identifies the limited set where the MOOP can sweep to identify the optimum points. Now, let's take into account the projection of the Feasible Set on the Objective Space, i.e. $f(\mathbb{S})$. As Pareto observed, since the Objective Space has cardinality more than one, $\dim \mathbb{S} > 1$, the objective vectors cannot be totally ordered, but only partially ordered. However some binary relations ($=$, \leq , $<$) can be defined.

Definition 3. For any two objective vectors \mathbf{u} and \mathbf{v} ,

$$\mathbf{u} = \mathbf{v} \quad \text{iff} \quad \forall i \in \{1, \dots, m\} : u_i = v_i;$$

$$\mathbf{u} \leq \mathbf{v} \quad \text{iff} \quad \forall i \in \{1, \dots, m\} : u_i \leq v_i;$$

$$\mathbf{u} < \mathbf{v} \quad \text{iff} \quad \mathbf{u} \leq \mathbf{v} \wedge \mathbf{u} \neq \mathbf{v}.$$

For example, as shown In Fig. 2.1b, the objective points \mathbf{y}_E and \mathbf{y}_F cannot be related since \mathbf{y}_E minimizes the objective function component f_1 respect to \mathbf{y}_F while vice versa for f_2 . For this reason Pareto introduced the concept of *dominance* to reflect the relation in the Objective Space \mathbb{Y} on the Decision Space \mathbb{X} .

Definition 4 (Pareto Dominance). For two decision vectors \mathbf{a} and \mathbf{b} three conditions arise:

$$\mathbf{a} \preceq \mathbf{b} \quad \text{iff} \quad \mathbf{f}(\mathbf{a}) \leq \mathbf{f}(\mathbf{b}) \quad (\mathbf{a} \text{ weakly dominates } \mathbf{b})$$

$$\mathbf{a} \prec \mathbf{b} \quad \text{iff} \quad \mathbf{f}(\mathbf{a}) < \mathbf{f}(\mathbf{b}) \quad (\mathbf{a} \text{ dominates } \mathbf{b})$$

$$\mathbf{a} \sim \mathbf{b} \quad \text{iff} \quad \mathbf{f}(\mathbf{a}) \not\leq \mathbf{f}(\mathbf{b}) \wedge \mathbf{f}(\mathbf{b}) \not\leq \mathbf{f}(\mathbf{a}) \quad (\mathbf{a} \text{ is indifferent to } \mathbf{b})$$

The Defn. 4 introduces the order relation between the decision points in the Decision Space \mathbb{X} examining the related objective points in Objective Space \mathbb{Y} . The defined binary relations, i.e. $\{\preceq, \prec, \sim\}$, allow to establish an optimality criterion for MOOP based on Defn. 4. For example, let us consider the decision point $F \in \mathbb{X}$ in Fig. 2.1b. It is mapped into the objective point $\mathbf{y}_F \in \mathbb{Y}$ through the objective function $\mathbf{f}(\cdot)$. Some considerations are easily derived just by looking at the position of the points in the Objective Space \mathbb{Y} :

- F dominates G ($F \prec G$) since $\mathbf{y}_F < \mathbf{y}_G$ that corresponds to have $f_1(F) < f_1(G)$ and $f_2(F) < f_2(G)$ following the definition given in Defn. 3;

- B and C dominate F ($B, C \succ F$) for the aforementioned reasons;
- A weakly dominates F ($A \succeq F$) because $\mathbf{y}_F \leq \mathbf{y}_A$, in fact, $f_1(A) < f_1(F)$ but $f_2(A) = f_2(F)$ causing the weak dominance;
- F is indifferent to E ($F \sim E$) since $\mathbf{y}_F \not\leq \mathbf{y}_E$ and $\mathbf{y}_E \not\leq \mathbf{y}_F$, in fact $f_1(E) < f_1(F)$ and $f_2(F) < f_2(E)$. The same consideration can be done for $F \sim D$.

Now, let us consider the decision point $A \in \mathbb{X}$. It is worth noting that \mathbf{y}_A is never dominated by the other points B, \dots, G , because $\mathbf{y}_{B\dots G} \not\prec \mathbf{y}_A$. Exploiting this properties is possible to define the meaning of optimum in presence of several objectives.

Definition 5 (Pareto Optimality). *A decision vector $\mathbf{x} \in \mathbb{X}$ is said to be non-dominated regarding a set $\mathbb{A} \subseteq \mathbb{S}$ iff*

$$\nexists \mathbf{a} \in \mathbb{A} : \mathbf{a} \prec \mathbf{x}$$

Extended the previous concept of Defn. 5 to the whole Decision Space \mathbb{S} , the following sets and frontier can be defined:

Definition 6 (Pareto Set and Front). *Let $\mathbb{A} \subseteq \mathbb{S}$. The operator $\mathcal{P}(\mathbb{A})$ gives the set of non-dominated decision vectors in \mathbb{A} :*

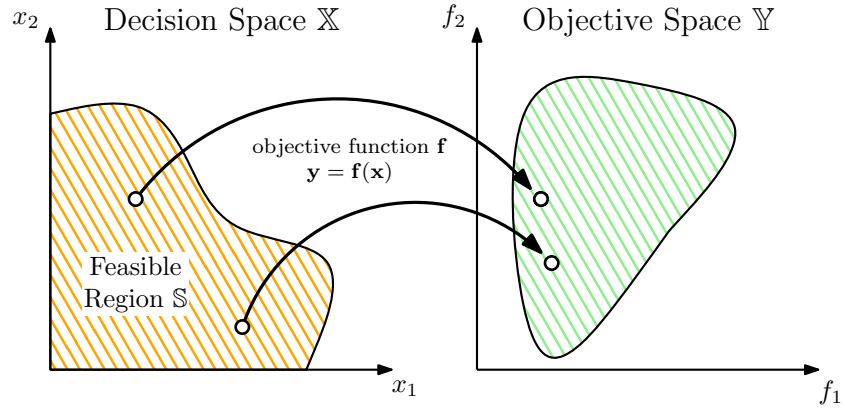
$$\mathcal{P}(\mathbb{A}) = \{\mathbf{a} \in \mathbb{A} \mid \mathbf{a} \text{ is non-dominated regarding } \mathbb{A}\} .$$

The set $\mathcal{P}(\mathbb{A})$ is the non-dominated set regarding \mathbb{A} , the corresponding set of objective vectors $\mathbf{f}(\mathcal{P}(\mathbb{A}))$ is the non-dominated front regarding \mathbb{A} .

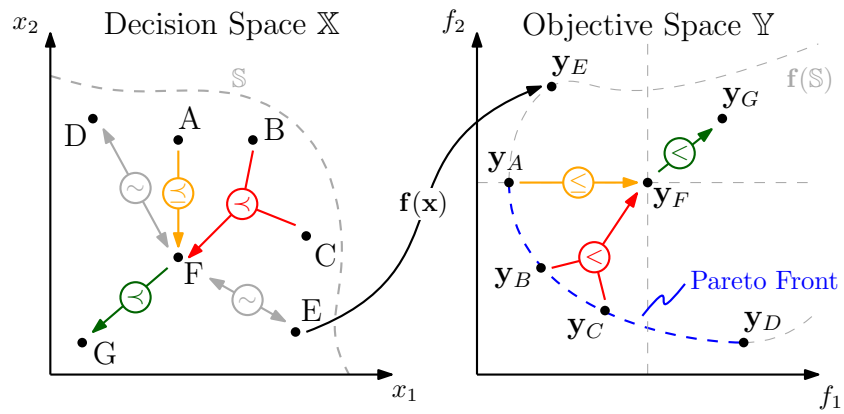
*Furthermore, the set $\mathbb{X}_{\mathcal{P}} = \mathcal{P}(\mathbb{S})$ is called the **Pareto-optimal** set and the set $\mathbb{Y}_{\mathcal{P}} = \mathbf{f}(\mathbb{X}_{\mathcal{P}})$ is denoted as the **Pareto-Optimal Front**, or simply **Pareto Front**.*

As shown in Fig. 2.1b, the decision points A, B, C, D represent the Pareto-Optimal set $\mathbb{X}_{\mathcal{P}}$ since their projections on the Objective Space $\mathbf{f}(\mathbb{X}_{\mathcal{P}})$ is a non-dominated set regarding \mathbb{S} . Furthermore, $\mathbf{f}(\mathbb{X}_{\mathcal{P}})$ is the Pareto Front in the Objective Space \mathbb{Y} .

The definitions for a maximization problem ($\geq, >, \succ, \succeq, \sim$) are equivalent.



(a) Basic concept



(b) Decision and Objective point relations

Figure 2.1: Multi-Objective Optimization Concept: (a) a basic description of the involved sets and map function, (b) an example of the binary relations that exist among vectors in both sets.

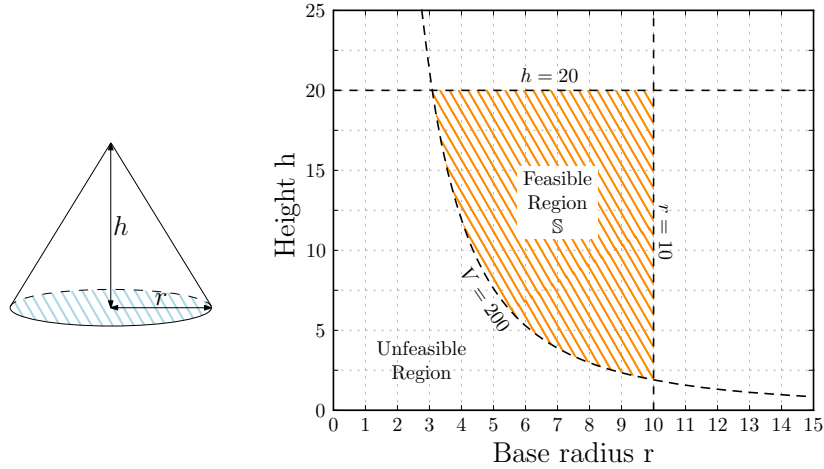


Figure 2.2: Simple example of MOOP: minimization of the lateral and total surface of a cone subject to a volume and radius/height constraints.

Dummy Example

For sake of clarity, a simple example is now reported to show the application of the MOO for a geometrical problem. Let suppose to minimize the lateral and total surface, S and T , of a cone described by its base radius r and height h . The decision space is bounded to $r \in [0, 10]$ and $h \in [0, 20]$, while the inequality constrained space considers only the decision vector which cone volume is greater than $V = 200$. Using MOO formalism, the problem becomes:

$$\begin{aligned} & \underset{\mathbf{x}}{\text{minimize}} && \mathbf{f}(\mathbf{x}) = [S, T] = \left[\pi r \sqrt{r^2 + h^2}, \pi r (r + \sqrt{r^2 + h^2}) \right] \\ & \text{subject to} && \mathbf{g}(\mathbf{x}) = V - \frac{\pi r^2 h}{3} \leq 0, \quad 0 \leq r \leq 10, 0 \leq h \leq 20, \end{aligned}$$

In this case the equality design space is not defined. In Fig. 2.2, the Feasible Region \mathbb{S} is highlighted along with the constraints on the decision variables. The simplest way to maps the Feasible Region to the Objective Space is to generate uniformly distributed coordinate points inside the decision range, then discard the ones not belonging to the inequality constraint space. The result of this procedure is shown in Fig. 2.3a where the red region identifies the points not satisfying the volume constraint. Zoom on the lower side of the mapped Feasible Region, i.e. the points belonging to the $\mathbf{f}(\mathbb{S})$, the Pareto Front can be located as depicted in Fig. 2.3b. However, more efficiency approaches to find the

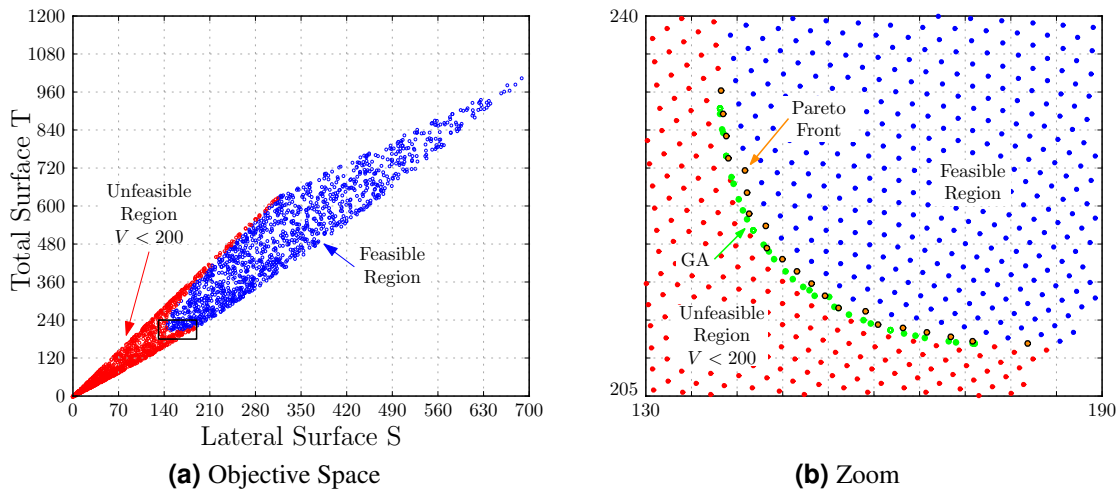


Figure 2.3: Objective Space of the MOOP for the lateral and total surface for a cone. (a) The mapped feasible region is indicated with blue dots while the decision vectors not satisfying the volume constraint are in red. (b) Zoom on the Pareto Front obtained from uniformly distributed decision space (orange) and using Genetic Algorithm (green).

Pareto Front of MOOP exist in literature instead of a brute-force approach. In the following paragraph the commonly used algorithms are described.

2.1.1 MOO Solving Methods

Multi-objective solution methods are classified according to how the vector-valued objective function $f(\mathbf{x})$ is treated in the process providing a common division between scalarizing and non-scalarizing techniques [7],[8]. In the former, the objective function is reduced to a scalar value reshaping the problem in a Single-Objective Optimization Problem (SOOP) while in the latter it is taken as it is. The Weighed Global Criterion Method for the scalarizing technique class and the Evolutionary Method for the non-scalarizing one.

Weighed Global Criterion (WGC) Method

As aforementioned, the MOOP is converted to a SOOP by a linear combination of the objectives, i.e. the problem becomes:

$$\begin{aligned} & \underset{\mathbf{x}}{\text{minimize}} && y = f(\mathbf{x}) = \sum_{i=1}^m w_i f_i(\mathbf{x}) \\ & \text{subject to} && \mathbf{g}(\mathbf{x}) \leq 0, \quad \mathbf{h}(\mathbf{x}) = 0, \quad \mathbf{x}^L \leq \mathbf{x} \leq \mathbf{x}^H, \end{aligned}$$

where w_i are called weights and, without loss of generality, normalized such that

$$\sum_{i=1}^m w_i = 1.$$

Sweeping different values of the weights w_i and collecting the solutions of related SOOP, the Pareto Front is so obtained. The main disadvantage of WGC method is to provide only a subset of the Pareto Front in case the latter is non-convex. In fact, let suppose the MOOP has two objectives $f_{1,2}$ as in the treated example. Defining the two weights $w_{1,2}$ such that $w_2 = 1 - w_1$, for each value of w_1 , the linked SOOP describes a straight line in the Objective Space $\mathbb{Y} = (f_1, f_2)$, i.e. $w_1 f_1 + w_2 f_2 - y = 0$. The slope is defined by the ratio of weights, so the minimum of y is found when the line is tangent to the Pareto Front of the mapped Feasible Space $\mathbf{f}(\mathbb{S})$. If the Pareto Front is convex, all the solutions of SOOP represent the whole Pareto Front, instead in case of a non-convex Front, the SOOP returns only the convex part, since the other parts are discarded during the minimization. An example is depicted in Fig. 2.4a, where for a given line slope three tangent points are found. However the point \mathbf{y}_X corresponds to a higher y value compared with points $\mathbf{y}_{B,C}$, and it is thus disregarded.

Evolutionary Methods

Evolutionary Methods belong to the non-scalarizing technique since they force the MOOP to keep the objective function in its vectorial format [9]–[10]. A subclass of the Evolutionary Methods are the Genetic Algorithms (GA). The GA are global optimization techniques,

which means they converge to the global solution rather than to a local one as implemented by the WGC methods. The advantages of this method can be summarized as:

- explores the Decision Space in multiple directions, so potential large spaces could be considered;
- does not impose any particular mathematical requirement for the objective function and the constraints, e.g. convex Pareto Front in WGC;
- performs well when the Objective Space is complex (discontinuous, with many local minima).

In Fig. 2.4b, the basic structure of a Genetic Algorithm is illustrated. Starting from an initial set of Decision Vector \mathbb{X}_0 , the algorithm maps the set to the Objective Space using the objective function, i.e. $f(\mathbb{X}_0)$. If the termination criteria are met, e.g. maximum number of iterations, minimum number of Pareto Front points or maximum distance among them, the algorithm returns the resulted Pareto Front otherwise it generates a new set of Decision Vector \mathbb{X}_1 . The principles with how the new generation \mathbb{X}_1 is obtained are essentially three:

- Selection: the non-dominated set regarding \mathbb{X}_i , i.e. $\mathbb{X}_{\mathcal{P},i}$, is passed on the next generation \mathbb{X}_{i+1} since represents the best solutions in the current iteration.
- Crossover: the components x_n of non-dominated decision set $\mathbf{x} \in \mathbb{X}_{\mathcal{P},i}$ are shuffled among vectors to generate new elements for the next population.
- Mutation: in a very limited set of non-dominated decision set $\mathbf{x} \in \mathbb{X}_{\mathcal{P},i}$, some components x_n are changed arbitrarily. This procedure is vital to ensuring genetic diversity within the next population.

An example of its application is reported in Fig. 2.3b where the Pareto Front of the cone optimization was also implemented via GA. The outcomes are the green point set, and it's worth noting how they are more accurate respect to the brute-force approach.

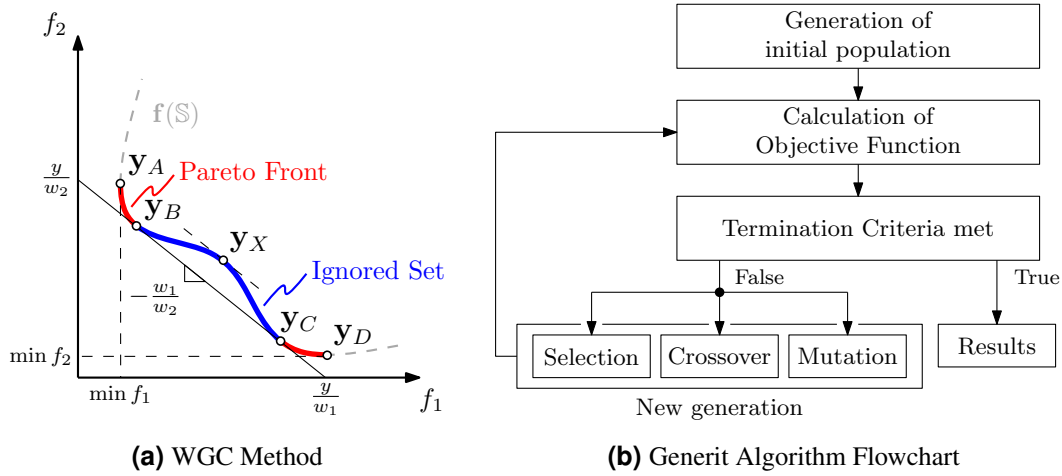


Figure 2.4: Typical MOOP Solving Methods: (a) Weighted Global Criterion where is highlighted the issue with non-convex Pareto Front; (b) generic Genetic Algorithm flowchart.

2.2 MOOP in EPC Design

After the basic principles of the Multi-Objective Optimization Problem are given, their application regarding the optimization of Electronic Power Converters (EPCs) can be introduced. In the last decades the literature provided a wide set of applications, as reported in [11]– [15]. For a power converter different objectives, or rather Performance Indices, can be defined in order to take into account which are the desired features to optimize. The more incisive indices in EPC design can be listed as follows:

- Efficiency, defined as the ratio of the output available power P_o to the input processed power P_i :

$$\eta = \frac{P_o}{P_i}.$$

This performance index is dimensionless since ratio of two power terms.

- Power Density, measured as the nominal output power P_o and the overall volume V or weight W of the converter:

$$\rho = \frac{P_o}{V} \left(\frac{\text{kW}}{\text{m}^3}, \frac{\text{VA}}{\text{m}^3} \right),$$

$$\gamma = \frac{P_o}{W} \left(\frac{\text{kW}}{\text{kg}}, \frac{\text{VA}}{\text{kg}} \right),$$

where γ is especially useful for mobile application, i.e. automotive.

- Relative Costs, as the ratio between the nominal output power P_o and the final cost C_{EPC} of the EPC:

$$\sigma = \frac{P_o}{C_{EPC}} \left(\frac{\text{kW}}{\text{€}}, \frac{\text{VA}}{\text{€}} \right),$$

that represents an important industrial Performance Index.

The Performance Indices considered in the next chapter will be the efficiency η and the *volumetric* power density ρ . The choice to optimize the efficiency η is justified by the fact that this index gives a direct measure of losses that degrade the power conversion in EPC. On the other hand, the optimization of the power density ρ has been chosen under the strong hypothesis that it's related to the quality and cost of EPC design. For clarity, the chief contribution in volume in an EPC are given by the magnetic components, the capacitors and the cooling system. The minimization of EPC components volume has a dual effect: a cost reduction of the raw materials, e.g. core, winding and heatsink materials, and a better exploitation of the converter components. To cope with the aforementioned objectives, models that estimate the losses and volume of the converter components become mandatory. The Decision Space, or rather Design Space in this case, could be really wide due to the huge degrees of freedom, e.g. component values and types, switching frequency, modulation strategies and selected topology. In the perspective of this dissertation, the MOO represents a valid tool to guide the design process to compare different solutions among them or with the related State of Art. In this way, the models can be set to consider only the main loss phenomena and volume contributions reducing drastically the time-consumption too.

A useful flowchart of MOOP in EPC Design can be found in [11], also reported in Fig. 2.5. As aforesaid, from the nominal specifications, e.g. input/output voltage, nominal power and output voltage ripple, a converter topology and its related modulation scheme are chosen and the electrical quantities in the components are derived from the circuit model. In this way, for each kind of component, a specific model estimates losses and volume. Moreover, inner optimization loops can be implemented to find the Pareto Front designs for a given component value. This practice could be necessary due to the presence of

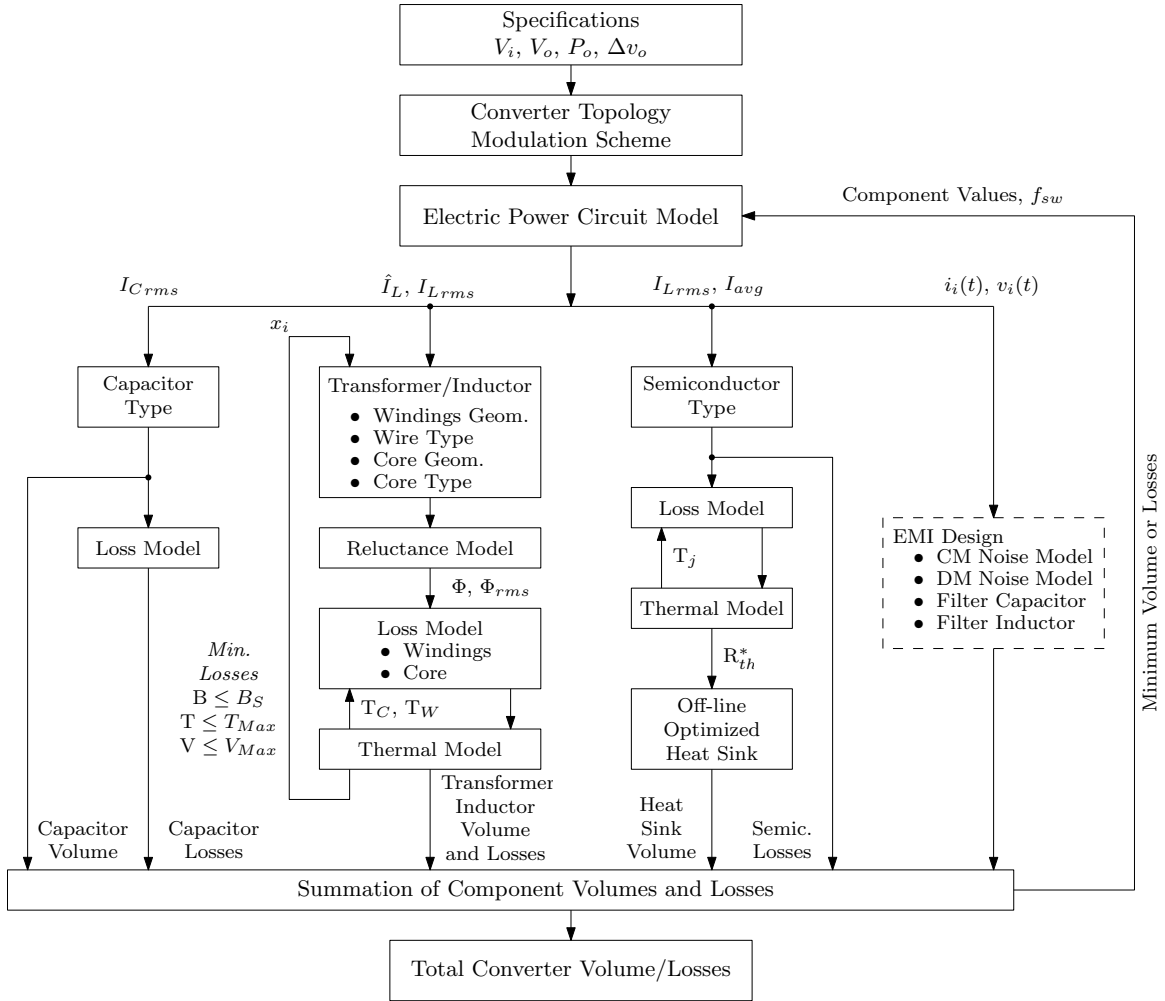


Figure 2.5: MOOP in EPC Design proposed in [11].

magnetic components, i.e. inductor or transformer, since they permit different arrangement in terms of core shapes and winding arrangements that require to be investigated. In the next chapter, the considered loss phenomena are briefly described, while, in the last chapter, the considered test case will permits to discuss also the magnetic component optimization.

2.3 Summary

In this chapter, the Multi-Objective Optimization Theory has been treated to supply the relative background necessary for the next chapter. Starting from the basic definitions of Decision and Objective Space, the introduced concept of Pareto Dominance permits to define the binary relations in a partially ordered set. Moreover, a simple geometrical example has been discussed to report the different step in the MOOP definition. To deal with the MOOP resolution, a brief overview about the common solving methods is provided, highlighting their pros and cons. At the end, the aforementioned theory is applied on the EPC design, showing which could be the different objective functions and the considered decision space. A flowchart of MOO design process is also reported to highlight the different models that are required.

Chapter 3

Theoretical and Technical Background

This chapter outlines the theoretical background of the component modelling presented herein. As described in Sec. 2.2, the Multi-Objective Optimization Problem (MOOP) requires the definition of the vector-value objective function, i.e. $f(\cdot)$, to map the feasible Design Space \mathbb{X} to the Objective Space \mathbb{Y} . In the Distributed Energy System scenario, the optimization of the EPC design has been set by means of efficiency and volumetric power density. Given the nominal power as a project specification, these two figures of merit are only dependent on the losses and the volume of the converter components. Keeping in mind the aim of the optimization process, i.e. an reasonable estimation of the Performance Indices, only the principal phenomena of losses and volume can be taken into account. A description of considered losses and volume for each main component in a EPC is reported to follow.

Magnetic Devices This category include inductors, transformers and mutual inductors, namely each component that includes a magnetic core. The volume is dependent on the device geometry, thus the physical dimensions of the selected core and the kind of wire are needed. Instead, the component losses can be subdivided in core losses and winding losses, depending on where they take place. The modelling and the optimization of the magnetic components is widely described in detail in [16]. A brief description of the origin of losses and their different modelling is discussed in Sec. 3.1.

Capacitor Their volume depends on the construction technology and is quite linear with the maximum stored energy. In this case, a simple fitting function for the capacitor volume can be obtained in the form of $k_T C V_{C,max}^2$, where C is the capacitance value, $V_{C,max}$ is the maximum rated voltage and k_T is a technology parameter [17]. Regarding the losses, the Equivalent Series Resistance is considered to estimate the Joule losses. The quality factor $\tan \delta$, that is defined as $\tan \delta = \frac{ESR}{2\pi f C}$, since is quite constant for each technology, can parametrize the ESR as a function of the capacitance values and the fundamental frequency of the flowing current.

Semiconductor Devices This category includes a wide sorts of switching devices, e.g. diode, SRC (Silicon Controlled Rectifier), thyristor, GTO (Gate Turn-Off thyristor), Triac, BJT, MOSFET, IGBT and so on. In this dissertation only the MOSFET devices are contemplate because of their use in Ch. 5. Their volume depends of the chosen package so it is an initial condition in the MOOP. Instead their losses can be separated in two contributes: the conduction and the switching ones. The first occur when the device is in full conduction state and are related to the channel resistance. They can easily estimated knowing the On-Drain-Source resistance and the RMS current in the device. The second, i.e. the switching losses, occurs when the device is commutating from a blocking state to a conducting state and vice versa. The dissipated energy depends on the drain current and drain-source voltage at the commutation. Several switching loss modelling are described in the literature that accuse the MOSFET output capacitance of dissipating energy during the switching transition, [18]–[20]. In Sec. 3.2 the used model for switching loss estimation is described in the Sec. 5.2.3. However the model does not consider the dissipate energy due the gate driver.

Heatsink Commonly in the power converter, the semiconductor devices are unable to dissipate on their own the generate losses. For this reason, an heat exchanger is mandatory to regulate the devices' temperature at optimal levels. The heat is transferred to a fluid medium, often air or a liquid coolant, in passive or active way. Passive heatsink is an aluminum-finned radiator that dissipates heat through convection, while an active heatsink needs to supply some cooling device, e.g. a fan or a Peltier cell. In

this dissertation, only the volume contribution is taken into account with the Cooling System Performance Index (CSPI) described in Sec. 5.2.5.

3.1 Magnetic Device Losses

The magnetic devices are affected by the losses arise from the magnetization process of core. The magnetic flux density B is not a single-value function of the external applied magnetic field H as consequence of a *phase lag* between the two variables, as plotted in Fig. 3.1a.

This phenomenon is called hysteresis and it is indicative of out-of-equilibrium process where an irreversible energy transformation takes place. In the magnetic materials, the losses are derived by local rearrangement of the magnetic domains presented in the core. In Fig. 3.1b the magnetic domain are showed highlighting the orientation of the magnetization vector M . Applying an external field, the minimum energy domain configuration is destroyed and the domains move toward a new stable configuration. This jumps between two consecutive stable configurations are the so called Barkhausen jumps. The local flux changes around the Barkhausen jumps generate eddy currents in the closer volume, causing the core losses.

The physical treatment of the hysteresis in the magnetic medium is broadly outlined in [21] where the energy and thermodynamic aspects regarding the domain configuration are considered. From the point of view of modelling the core losses, [16] represents the current State of Art. In the following section a brief description of the different modelling equations are provides.

3.1.1 Core Loss Modelling

Different degrees of accuracy can be achieved in the core loss estimation depending on the available information and the desired computation effort. Basically, the core losses P can be split in three terms:

$$P = P_{hyst} + P_{cl} + P_{ex} = C_0 f + C_1 f^2 + C_3 f^{3/2}, \quad (3.1)$$

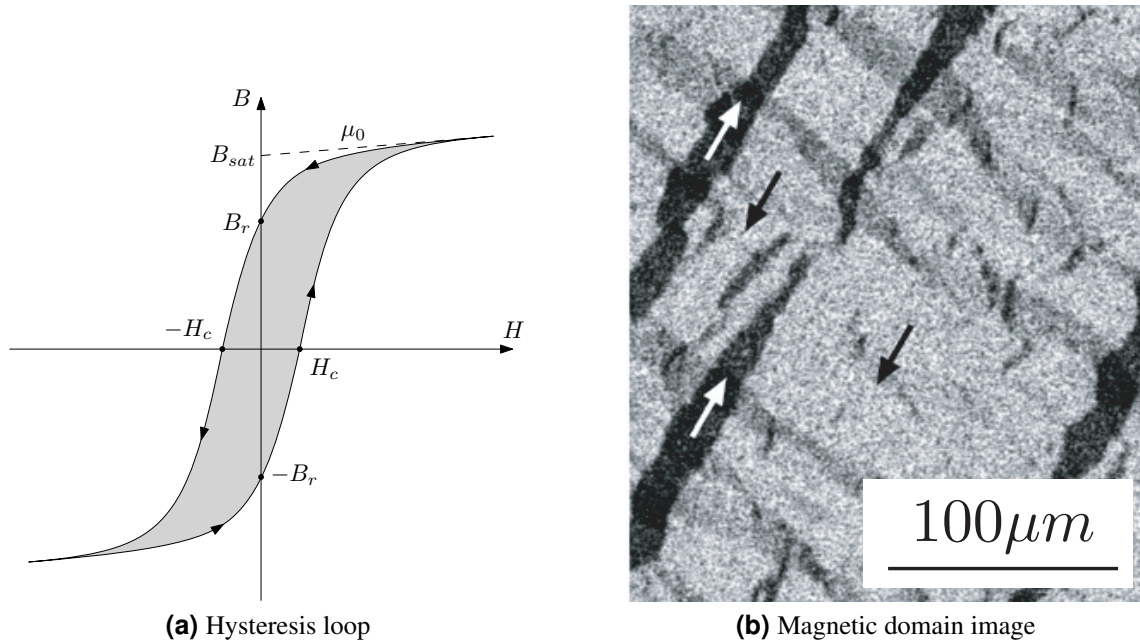


Figure 3.1: Hysteresis in magnetic components: (a) hysteresis loop in the (H, B) -plane; (b) magnetic domain image obtained by double wavelength microscopy of NiFe sample [22].

where $C_{1,2,3}$ are experimental parameters and f is the frequency of the magnetization signal. The hysteresis loss P_{hyst} are associated to Barkhausen jumps, while the classical losses P_{cl} describe the loss calculated from the solution of the Maxwell's equation in a homogeneous material without any domain structure, then geometrically defined. Finally, the excess loss occurs from the eddy current surrounding the active domain wall motion under the action of the external field [23]. However this simple model has to be tailored through experimental measures so it cannot be a valid estimation model for the MOOP.

The most reasonable and useful model is provided by the Steinmetz equation and its further improvements. They are characterized by few material parameters, i.e. k , α and β , that can be easily extracted by the core material datasheet. It is worthy to noting that the outcome of these equations is a power loss density, thus expressed in kW/m^3 . The above concerns are set out in more detail individually below in order of accuracy.

Steinmetz Equation (SE) It represents the simplest and oldest equation regarding loss calculation. It is valid only for sinusoidal flux density, and the power loss density P_V is

given by:

$$P_V = k f^\alpha B^\beta \quad (3.2)$$

where B is the amplitude of the sinusoidal flux density [24].

Modified Steinmetz Equation (MSE) To include in (3.2) the rate-dependent losses, an equivalent frequency f_{eq} is calculated from the rate of change of the induction B , providing the following equation:

$$f_{eq} = \frac{1}{\Delta B} \int_0^T \left(\frac{dB}{dt} \right)^2 dt \quad (3.3)$$

$$P_V = k f_{eq}^{\alpha-1} B^\beta f \quad (3.4)$$

where ΔB is the peak to peak value of the induction B [25].

General Steinmetz Equation (GSE) The further step, it was supposed that the instantaneous loss power is a function of the flux density and its derivative, i.e. $P_V(t) = P_d \left(\frac{dB}{dt}, B \right)$, where P_d is an unknown power dissipation function. Both (3.5) and (3.7) are different solutions for the average integral when equalized to SE in case of sinusoidal flux density [26], [27].

$$P_V = \frac{1}{T} \int_0^T k_i \left| \frac{dB}{dt} \right|^\alpha |B(t)|^{\beta-\alpha} dt \quad (3.5)$$

$$k_i = \frac{k}{(2\pi)^{\alpha-1} \int_0^{2\pi} |\cos \theta|^\alpha |\sin \theta|^{\beta-\alpha} d\theta} \quad (3.6)$$

improved General Steinmetz Equation (iGSE)

$$P_V = \frac{1}{T} \int_0^T k_i \left| \frac{dB}{dt} \right|^\alpha \Delta B^{\beta-\alpha} dt \quad (3.7)$$

$$k_i = \frac{k}{(2\pi)^{\alpha-1} \int_0^{2\pi} |\cos \theta|^\alpha 2^{\beta-\alpha} d\theta} \quad (3.8)$$

improved² General Steinmetz Equation (i²GSE) The last one considers the relation process, discussed in [28], that occurs when the domain configuration moves toward a

new thermal equilibrium in the core. The energy released in this process can be described as a first-order system which time constant is $\tau_0 = 1\text{ps} \div 10\text{ns}$ [29].

Other noteworthy models can be found in the literature: Hysteresis Model [30] is an empirical description of the hysteresis loop using, for example, hyperbolic functions, and the Preisach Model [31] is a stochastic description of the magnetization process.

The aim of this dissertation calls for a quite accurate model and easy to be implement. For this reason, the iGSE model has been identified as a good candidate for the magnetic loss estimation.

3.1.2 Winding Loss Modelling

The losses that occurs in the winding of a magnetic core device derives from the current density distribution inside the conductor [32]–[34]. At high frequency, the current density in a conductor becomes larger near the surface and decreases towards the centre, namely skin effect. Furthermore, when currents are flowing through more close conductors, the magnetic field produced by each one affected the others. The resulting current distribution is crowded around the maximum magnetic field region, namely proximity effect. All this phenomena can be summarized in few coefficient that scale the DC nominal resistance of the wire, such that the final value of the winding resistance R_{ac} can be obtained as

$$R_{ac} = R_{dc} \sum_i k_i \quad (3.9)$$

In Sec. 5.2.4 the application of this concept is reproposed in detail.

3.2 Semiconductor Device Losses

In this section the switching loss modelling is presented following in part the approach described in [20]. Let suppose the commutation occurs as depicted in Fig. 3.2 where the two switches $S_{1,3}$ are complementary driven with a dead time t_d between the two commands of S_1 and S_2 , and $C_{1,3}$ are the output capacitance C_{oss} provided in the MOSFET datasheet.

In the following analysis two stronger hypotheses are made:

Hp. 1 the switching losses are entirely associated to the device output capacitances, that is equivalent to assume that the switches $S_{1,3}$ in Fig. 3.2 are ideal during the commutations;

Hp. 2 the switching node current i_x remains constant during the whole dead time interval.

In the following sections the Low-to-High (LH) and High-to-Low(HL) transitions are both described. The first occurs when the voltage v_x in Fig. 3.2 is set from 0 to V_{DC} while in second case vice versa. For clarity, the functions E_{tot} , E_{oss} and Q_{oss} are obtained from numerical interpolation or integration of datasheet graphs.

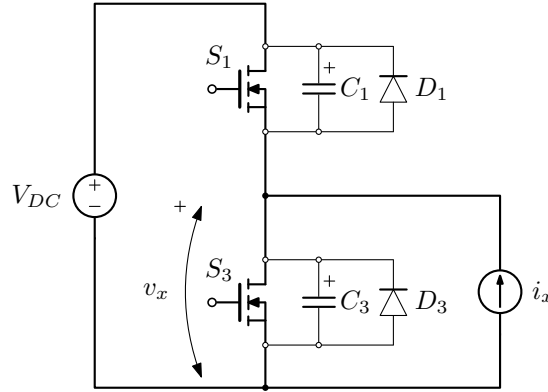


Figure 3.2: Equivalent circuit for the Switching Loss estimation.

3.2.1 LH Transition

At the beginning of the commutation, S_3 is conducting and the relative output capacitance C_3 is discharged ($v_x(0) = v_3(0) = 0$), while S_1 is off and C_1 is charged at $v_1(0) = V_{DC}$. It's worth to remember that the analysis is limited in the case of $i_x = I_{LH}$ is constant during the whole commutation interval (t_d).

Hard Switching Hard Switching occurs when $I_{LH} < 0$. In this case the dissipated energy is calculated from datasheet, fitting the function of $E_{tot}(I_{DS}@V_{DS})$ and scaling to the operating voltage V_{DC} :

$$E_{LH} = E_{tot}(I_{LH}@V_{DS}) \frac{V_{DC}}{V_{DS}} \quad (3.10)$$

where V_{DS} represents the DC voltage used in the datasheet measurement setup.

Soft Switching To achieve Zero Voltage Switching (ZVS) or partial ZVS (pZVS), necessary condition is $I_{LH} > 0$. To distinguish which one occurs, the voltage at the swithing node has to be calculated.

The Kirchoff's law applied at the node is

$$i_x = -C_1(v_1) \frac{dv_1}{dt} + C_3(v_3) \frac{dv_3}{dt} \quad (3.11)$$

Integrating both terms of (3.11) in the dead time t_d , the charge balance gives

$$\begin{aligned} \int_0^{t_d} i_x dt &= \int_0^{t_d} \left[-C_1(v_1) \frac{dv_1}{dt} + C_3(v_3) \frac{dv_3}{dt} \right] dt \\ I_{LH} t_d &= - \int_{v_1(0)}^{v_1(t_d)} C_1(v_1) dv_1 + \int_{v_3(0)}^{v_3(t_d)} C_3(v_3) dv_3 \\ &= -Q_{oss}(v_1) \Big|_{V_{DC}}^{V_{DC}-v_{LH}} + Q_{oss}(v_3) \Big|_0^{v_{LH}} \\ &= -Q_{oss}(V_{DC} - v_{LH}) + Q_{oss}(V_{DC}) + Q_{oss}(v_{LH}) - \underbrace{Q_{oss}(0)}_0 \end{aligned} \quad (3.12)$$

where v_{LH} is the v_x voltage value at the end of the dead time, i.e. $v_x(t_d^-) = v_{LH}$.

Solving the following non-linear equation, the voltage v_x at the S_1 turn on can be found:

$$v_{LH} = \{v | v \in [0, V_{DC}] : Q_{oss}(V_{DC}) - Q_{oss}(V_{DC} - v) + Q_{oss}(v) - I_{LH} t_d = 0\} \quad (3.13)$$

that imposes $I_{LH} > 0$ to have a solution in (3.13).

At time t_d , as showed in Figure 3.3, S_1 turns on and the energy stored in the output capacitance of the devices, i.e. C_1 and C_3 , changes. For the sake of clarity, the behaviour of each device output capacitance is individually taken into account:

C_1 the stored energy is completely dissipated in the S_1 on-resistance R_{on} , thus its component in the switching losses is equal to $E'_{LH} = E_{oss}(V_{DC} - v_{LH})$.

C_3 the capacitance is charged to V_{DC} via R_{on} . The energy dissipated in the device S_1 during the C_3 charging process is equal to the difference between the energy delivered

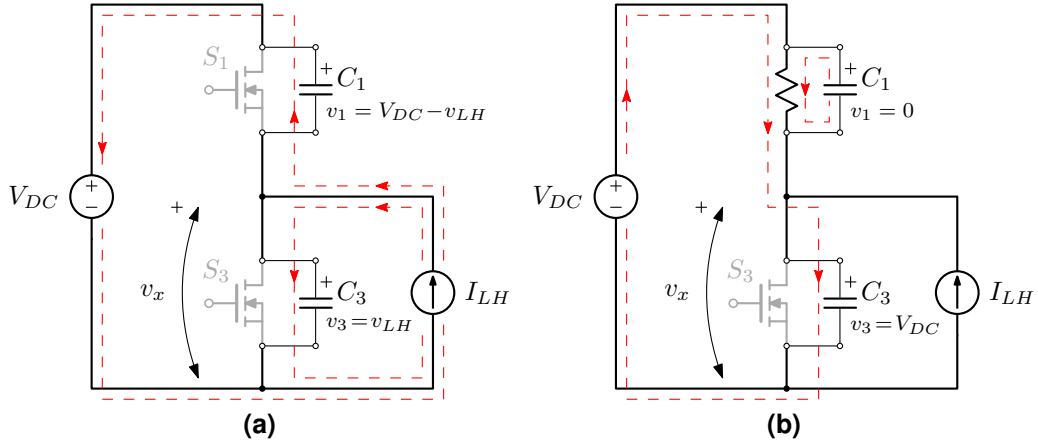


Figure 3.3: Equivalent LH Transition Model at S_1 turns on: (a) at the end of the dead time (t_d^-); (b) at S_1 turns on (t_d^+).

by the voltage source V_{DC} used to charge C_3 and the stored energy increment in the capacitor C_3 , i.e. $E'_{LH} = E_{DC} - \Delta E_{oss}$. The energy provided by the voltage source is $E_{DC} = \Delta Q_3 V_{DC}$ where $\Delta Q_3 = Q_{oss}(V_{DC}) - Q_{oss}(v_{LH})$ and the function Q_{oss} is the integral of the fitted function $C_{oss}(v_{DS})$ over v_{DS} . The C_3 energy increment is easily found as $\Delta E_{oss} = E_{oss}(V_{DC}) - E_{oss}(v_{LH})$, so the lost energy is equal to

$$E'_{LH} = [Q_{oss}(V_{DC}) - Q_{oss}(V_{DC} - v_{LH})] V_{DC} - [E_{oss}(V_{DC}) - E_{oss}(v_{LH})].$$

The total switching losses are equal to $E_{LH} = E'_{LH} + E''_{LH}$, that gives:

$$\begin{aligned} E_{LH} = & E_{oss}(V_{DC} - v_{LH}) + [Q_{oss}(V_{DC}) - Q_{oss}(v_{LH})] V_{DC} \\ & - [E_{oss}(V_{DC}) - E_{oss}(v_{LH})] \end{aligned} \quad (3.14)$$

3.2.2 HL Transition

Same considerations made in the previous section, can be done in the High to Low (HL) transition case, that, referring to Fig. 3.2, occurs when S_1 is turns off and S_3 is turns on after a t_d interval.

Hard Switching Hard Switching transition are achieved when $i_x = i_{HL} > 0$. In this case the dissipated energy is calculated as done for (3.10):

$$E_{HL} = E_{tot}(i_{HL}@V_{DS}) \frac{V_{DC}}{V_{DS}} \quad (3.15)$$

Soft Switching To achieve ZVS or pZVS, necessary condition is $i_{HL} < 0$. Using the same procedure done to obtain (3.13), the voltage v_x at the end of the dead time is equal to:

$$v_{HL} = \{v|v \in [0, V_{DC}] : -Q_{oss}(V_{DC}) - Q_{oss}(V_{DC} - v) + Q_{oss}(v) - i_{HL}t_d = 0\}. \quad (3.16)$$

At time t_d , S_3 turns on and the energy stored in the output capacitance of the devices changes as following:

C₁ the capacitance is charged to V_{DC} via the S_3 on-resistance R_{on} . The energy dissipated in the device S_3 during the C_1 charging process is equal to

$$E'_{HL} = [Q_{oss}(V_{DC}) - Q_{oss}(v_{HL})] V_{DC} - [E_{oss}(V_{DC}) - E_{oss}(V_{DC} - v_{HL})].$$

C₃ the stored energy is completely dissipated in R_{on} and its value is $E''_{HL} = E_{oss}(v_{HL})$.

The total switching losses are equal to $E_{HL} = E'_{HL} + E''_{HL}$, that is

$$\begin{aligned} E_{HL} = & E_{oss}(v_{HL}) + [Q_{oss}(V_{DC}) - Q_{oss}(v_{HL})] V_{DC} \\ & - [E_{oss}(V_{DC}) - E_{oss}(V_{DC} - v_{HL})] \end{aligned} \quad (3.17)$$

The equation (3.14) and (3.17) represent the energy dissipated at each commutation. The overall switching losses are of course given by the sum (3.14) and (3.17) and multiplied by the switching frequency.

3.3 Summary

In this chapter, the theoretical and technical background for the application of the MOO technique is provided. The modelling of losses and the volume for the main components

are described, with a particular focus on the magnetic and the switching devices. With this tool-set of components models, the final testcase presented in Ch. 5 can be discussed.

Chapter 4

Steady-State Converter Analysis

A broad class of DC-DC converters is based on an energy transfer mechanism that involves the use of a current shaping impedance inserted between two equivalent voltage sources, as represented in Fig. 4.1. In many cases, the current shaping impedance is a simple inductor, like in the unidirectional Single Active Bridge (SAB) topology [35] or in the more popular bidirectional Dual Active Bridge converter [36]–[43]. The same energy transfer mechanism is found also in current-fed topologies like [44]–[48], and in their bidirectional counterpart [49]–[51]. In fact, in these topologies, despite the use of input-port inductors, internal clamp capacitors act as voltage sources that generate the voltage $v_A(t)$ in Fig. 4.1.

In unidirectional topologies, voltage $v_A(t)$ is imposed by the modulation algorithm, while voltage $v_B(t)$ is related to the inductor current sign through the action of the rectification circuits in the switching network Sw_2 , while in bidirectional topologies both voltages $v_A(t)$ and $v_B(t)$ are determined by the control algorithm. In any case, a stair-case voltage $v_Z(t) = v_A(t) - v_B(t)$ is produced, with a consequent piece-wise linear inductor current waveform.

All aforementioned converters can be modified to obtain a resonant behavior by using a series resonant (SR) LC tank as current shaping impedance in Fig. 4.1. In some cases, the series capacitor is used just as DC blocking element to prevent core saturation in isolated topologies, thus not modifying the piecewise linear inductor current waveform. In many other situations, the resonant behavior is exploited to improve the soft-switching conditions of both switches and/or diodes, or to allow higher operation frequency with reduced elec-

tromagnetic interferences, thus allowing to develop high-efficiency and high power-density DC-DC converters. This is the case of the resonant DAB topologies [52]–[62], and their corresponding current-fed counterpart [63]–[67].

In most of the literature, the steady-state analysis of series resonant converter is worked out using two well known methods: the Fundamental Harmonic Approximation (FHA) as done in [52]–[56] and [61], where the voltages $v_A(t)$ and $v_B(t)$ are approximated with their components at the switching frequency [68], or the State Plane (Normalized) Analysis (SPA) as done in [57]–[64], where the ordinary differential equations (ODEs) of the resonant tank are solved. This last is more accurate than the first but requires a greater calculation effort.

The aim of this work is to provide a general and easy-to-use mathematical tool to figure out the SPA of SR converter class. The matrix formulation makes easy its implementation in popular mathematical tools like MATLAB[®] and simulation and calculation time-consumption to obtain the interested quantities in SR converter design is drastically reduced. This framework highly simplifies the analytic way to study the state evolution during the commutation instants, useful for ZVS and ZCS conditions check, and to define the closed-form expressions of main characteristic functions, e.g. transferred power and voltage conversion ratio. The chapter is structured as follows: in Sec. 4.1 the Generalized State-Space Model is described providing the main characteristic functions in typical applications, in Sec. 4.2 a voltage-fed converter is taken into account and the proposed method is compared with FHA, and finally, in Sec. 4.3, a current-fed topology is considered as case study to apply the aforesaid framework supported by simulation and experimental measurements taken on a prototype to validate the theoretical analysis.

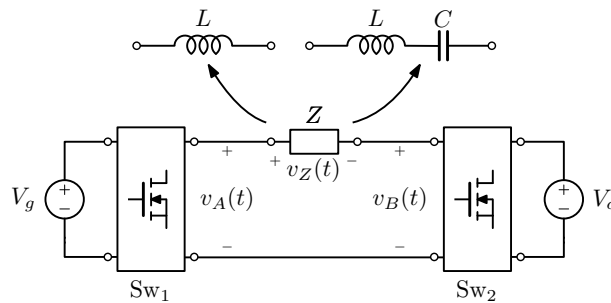
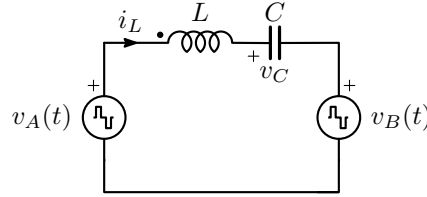


Figure 4.1: Generalized DC-DC conversion involving a current shaping impedance.

Table 4.1: Base and Normalized Variable Definitions.

Variable	Base	Normalized
Impedance/Load	$Z_r = \sqrt{\frac{L}{C}}$	$\rho = \frac{R}{Z_r}$
Frequency	$f_r = \frac{1}{2\pi\sqrt{LC}}$	$F = \frac{f_{sw}}{f_r}$
Voltage	$V_{base} = V_o$	$u_x = \frac{v_x}{V_{base}}$
Current	$I_{base} = \frac{V_{base}}{Z_r}$	$j_x = \frac{i_x}{I_{base}}$
Power	$P_{base} = \frac{V_{base}^2}{Z_r}$	$\Gamma_x = \frac{P_x}{P_{base}}$


Figure 4.2: Generalized DC-DC Series Resonant Converter.

4.1 Generalized State-Space Model

The analysis will be presented in normalized form using the base variables indicated in Table 4.1. This approach allows to spread its application across different topologies where the energy exchange process take essentially place as illustrated in Fig. 4.2. The only assumption is to have stair-case voltages $v_A(t)$ and $v_B(t)$, i.e. voltage $v_Z(t) = v_A(t) - v_B(t)$ is constant in every switching sub-interval.

4.1.1 Sampled Steady-State Trajectories

Let us suppose the converter assumes a fixed number of topological states in the switching period T_{sw} , each associated with a given impressed voltage $V_{Z,i} = v_{A,i} - v_{B,i}$, $i \in \mathbb{N}$, and with the corresponding sub-interval duration $\Delta t_i = t_i - t_{i-1}$. In the i -th state, the trajectory of state-space variables (i_L, v_C) is obtained resolving the ODE system imposing the initial

4.1. Generalized State-Space Model

conditions $(I_{L,i-1} V_{C,i-1})$ and the related voltage $V_{Z,i}$. The solution is expressed by

$$\begin{aligned} i_L(t) &= I_{L,i-1} \cos(\omega_r t) - \frac{V_{C,i-1}}{Z_r} \sin(\omega_r t) + \frac{V_{Z,i}}{Z_r} \sin(\omega_r t), \\ v_C(t) &= Z_r I_{L,i-1} \sin(\omega_r t) + V_{C,i-1} \cos(\omega_r t) + V_{Z,i}(1 - \cos(\omega_r t)), \end{aligned} \quad (4.1)$$

where $\omega_r = 2\pi f_r$ and Z_r are the resonance frequency and characteristic impedance of the series LC tank, respectively.

Moving from time to angle dependency, i.e. $\theta = 2\pi f_{sw} t$ where f_{sw} is the switching frequency, and normalizing according to Table 4.1, the normalized final values of state variables $\mathbf{x}_i = (J_i U_i)$ at θ_i instants, can be related to the previous one \mathbf{x}_{i-1} and the applied voltage $U_{Z,i}$ as:

$$\begin{bmatrix} J_i \\ U_i \end{bmatrix} = \begin{bmatrix} \cos \frac{\delta_i}{F} & -\sin \frac{\delta_i}{F} \\ \sin \frac{\delta_i}{F} & \cos \frac{\delta_i}{F} \end{bmatrix} \begin{bmatrix} J_{i-1} \\ U_{i-1} \end{bmatrix} + \begin{bmatrix} \sin \frac{\delta_i}{F} \\ 1 - \cos \frac{\delta_i}{F} \end{bmatrix} U_{Z,i} \quad (4.2)$$

or in matrix form

$$\mathbf{x}_i = \mathbf{M}_i \mathbf{x}_{i-1} + \mathbf{N}_i U_{Z,i}, \quad (4.3)$$

in which $\delta_i = \theta_i - \theta_{i-1}$ represents the normalized sub-interval duration.

Starting from the initial state \mathbf{x}_0 and iterating (4.3) for N sub-intervals, the sampled state trajectory at the N-th commutation is obtained as:

$$\mathbf{x}_N = \mathbf{M}_{N,1} \mathbf{x}_0 + \mathbf{H}[U_g \mathbf{q}_A - \mathbf{q}_B], \quad (4.4)$$

where the following vectors and matrices are introduced:

- the clockwise rotation matrix $\mathbf{M}_{k,j} = \prod_j^k \mathbf{M}_i \in \mathbb{R}^{2 \times 2}$, which definition is

$$\mathbf{M}_{k,j} = \begin{bmatrix} \cos \frac{\delta_{k,j}}{F} & -\sin \frac{\delta_{k,j}}{F} \\ \sin \frac{\delta_{k,j}}{F} & \cos \frac{\delta_{k,j}}{F} \end{bmatrix} \quad (4.5)$$

where the compact angle notation $\delta_{m,n} = \sum_n^m \delta_i$ for $m > n$ or $\delta_{m,n} = \delta_{N,1} + \delta_m + \delta_n -$

$\delta_{n,m}$ for $m < n$ is introduced;

- the matrix $\mathbf{H} = [\mathbf{M}_{N,2}\mathbf{N}_1 \dots \mathbf{M}_{N,k+1}\mathbf{N}_k \dots \mathbf{N}_N] \in \mathbb{R}^{2 \times N}$, where the matrix product $\mathbf{M}_{N,k+1}\mathbf{N}_k$, $k \in [1, N]$ in \mathbf{H} assumes the form

$$\mathbf{M}_{N,k+1}\mathbf{N}_k = \begin{bmatrix} \sin \frac{\delta_{N,k}}{F} - \sin \frac{\delta_{N,k+1}}{F} \\ \cos \frac{\delta_{N,k+1}}{F} - \cos \frac{\delta_{N,k}}{F} \end{bmatrix} \quad (4.6)$$

with $\delta_{N,N+1} = 0$.

- the vectors $\mathbf{q}_{A,B} \in \mathbb{R}^{N \times 1}$ such that $q_{A,i}V_g = v_{A,i}$ and $q_{B,i}V_o = v_{B,i}$.

The vectors $\mathbf{q}_{A,B}$ have the purpose to abstract the voltage gain of switching networks from their implementation, in this way more topologies can be analysed using the same mathematical frame.

If the steady-state condition is verified at the N -th interval, i.e. $\mathbf{x}_N = \mathbf{x}_0$, the initial state value can be derived from (4.4) as

$$\mathbf{x}_0 = \mathbf{W}[U_g\mathbf{q}_A - \mathbf{q}_B], \quad (4.7)$$

with $\mathbf{W} = (\mathbf{I} - \mathbf{M}_{N,1})^{-1}\mathbf{H}$. The initial state can be evaluated if and only if $(\mathbf{I} - \mathbf{M}_{N,1})$ is invertible, i.e. $\delta_{N,1} \neq 2\pi F$. This constraint corresponds to avoid the condition $f_{sw} = f_r$, for which the resonant tank impedance is zero. The expression of the k -th column vector of \mathbf{W} is

$$\mathbf{w}_k = \frac{\sin \frac{\delta_k}{2F}}{\sin \frac{\delta_{N,1}}{2F}} \begin{bmatrix} -\sin \frac{\delta_{N,k} - \delta_{k,1}}{2F} \\ \cos \frac{\delta_{N,k} - \delta_{k,1}}{2F} \end{bmatrix}, \quad (4.8)$$

Only active topological states take part in (4.4)–(4.7), namely the intervals where the resonant tank variables don't change are neglected. The dead time T_d , and associated dead angle α , in DCM mode is an example of neglected interval, since inductor current i_L stays zero and the capacitor voltage v_C is clamped during all its duration. A graphical interpretation of the just introduced angle convention is reported in Fig. 4.3a. Let us focus on Fig. 4.3a and its usage: each commutation instant t_i , $i \in [0, N]$, is projected to the corre-

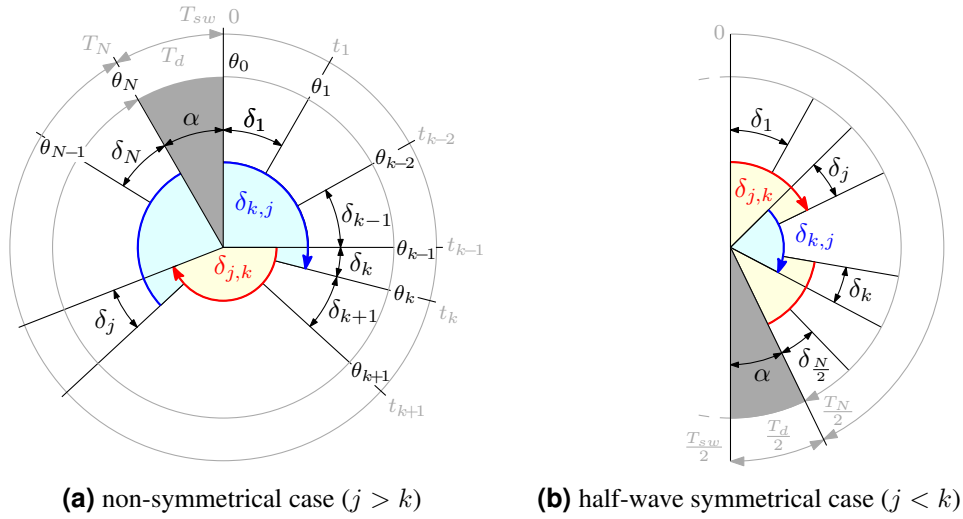


Figure 4.3: Angle convention: the time T_N is equal to the switching period T_{sw} for CCM modes, otherwise to $T_{sw} - T_d$ for DCM modes, with T_d is the overall dead-time where the inductor current stays zero.

sponding angle θ_i using the aforementioned relation, i.e. $\theta_i = 2\pi f_{sw} t_i$. The single interval duration δ_i , $i \in [1, N]$ is the difference of the angle endpoint values, i.e. $\delta_i = \theta_i - \theta_{i-1}$, while the composed duration $\delta_{y,x}$ is the sum of the intervals δ_i starting from δ_x and ending to δ_y in a clockwise direction, and neglecting the dead angle α if the considered path goes over it. For example, the reported interval $\delta_{k,j}$ in Fig. 4.3a corresponds to the sum of the angles highlighted in blue, with the grey dead angle α is disregarded. The same aspects can be identified for the convection of Fig. 4.3b, where only half a switching period is taken into account.

The mathematical framework which has so far been developed permits to figured out the sampled state trajectories in all operating modes, either CCM and DCM, computing (4.7) and proceeding along the sampled trajectory with (4.3).

In case the impressed voltage $u_Z(t)$ is a half-wave symmetric waveform, i.e. $\delta_k = \delta_{N/2+k}$ and $q_{A(B),k} = -q_{A(B),N/2+k}$ with $k \in [1, N/2]$, (4.7) can be computed using only the first $N/2$ inputs and the renamed column vector \mathbf{w}'_k of matrix $\mathbf{W}' \in \mathbb{R}^{2 \times N/2}$ assumes

the following expression

$$\mathbf{w}'_k = -\frac{\sin \frac{\delta_k}{2F}}{\cos \frac{\delta_{N/2,1}}{2F}} \begin{bmatrix} \cos \frac{\delta_{N/2,k} - \delta_{k,1}}{2F} \\ \sin \frac{\delta_{N/2,k} - \delta_{k,1}}{2F} \end{bmatrix}, \quad (4.9)$$

such that

$$\mathbf{x}_0 = \mathbf{W}' [U_g \mathbf{q}'_A - \mathbf{q}'_B] \quad (4.10)$$

with $\mathbf{q}'_{A,B} \in \mathbb{R}^{N/2 \times 1}$ are the related sub-vectors of $\mathbf{q}_{A,B}$ considering only the first $N/2$ elements.

4.1.2 Normalized Output Power

The normalized output power is given by

$$\Gamma = \frac{P_o}{P_{base}} = \frac{1}{2\pi} \sum_1^N q_{B,i} \int_{\delta_i} j_L(\theta) d\theta. \quad (4.11)$$

The inductor current i_L is related to the resonant capacitor voltage v_C by the normalized differential $j_L d\theta = F du_C$. Substituting this relationship in (4.11) gives

$$\Gamma = \frac{F}{2\pi} \sum_1^N q_{B,i} [U_i - U_{i-1}] = \frac{F}{2\pi} \mathbf{q}_B^T \Delta \mathbf{U}, \quad (4.12)$$

where the vector $\Delta \mathbf{U} = [\Delta U_1 \dots \Delta U_N]^T \in \mathbb{R}^{N \times 1}$ is defined as stack of the difference between two consecutive capacitor voltage state values, i.e. $\Delta U_k = U_k - U_{k-1}$. Defining the vector $\Delta \mathbf{x} = [\Delta \mathbf{x}_1 \dots \Delta \mathbf{x}_N]^T \in \mathbb{R}^{2N \times 1}$ as a stack of two consecutive state differences, i.e. $\Delta \mathbf{x}_k = \mathbf{x}_k - \mathbf{x}_{k-1}$, $k \in [1, N]$, the interested vector $\Delta \mathbf{U}$ is equal to the even-row elements of $\Delta \mathbf{x}$. To compute $\Delta \mathbf{x}$, the (4.3) and (4.7) are used to achieve the following matrix representation

$$\Delta \mathbf{x} = (\mathbf{S}^X + \mathbf{S}^H) [\mathbf{q}_A U_g - \mathbf{q}_B] \quad (4.13)$$

4.1. Generalized State-Space Model

where the (j, k) -th sub-vectors ($j, k \in [1, N]$) of the $\mathbf{S}^X \in \mathbb{R}^{2N \times N}$ and $\mathbf{S}^H \in \mathbb{R}^{2N \times N}$ are so defined

$$S_{j,k}^X = (\mathbf{M}_{j,1} - \mathbf{M}_{j-1,1})(\mathbf{I} - \mathbf{M}_{N,1})^{-1} \mathbf{M}_{N,k+1} \mathbf{N}_k$$

$$S_{j,k}^H = \begin{cases} \mathbf{0} & j < k \\ \mathbf{N}_k & j = k \\ (\mathbf{M}_{j,k+1} - \mathbf{M}_{j-1,k+1}) \mathbf{N}_k & j > k \end{cases} \quad (4.14)$$

The matrix \mathbf{N}_k can be traced back to \mathbf{M}_k such that $\mathbf{N}_k = (\mathbf{I} - \mathbf{M}_k) \mathbf{C}_2$, where $\mathbf{C}_2 = [0 \ 1]^T$. Since the interested value is $\Delta U_k = \mathbf{C}_2^T \Delta \mathbf{x}_k$, the expression for $\Delta \mathbf{U} = \mathbf{S}[\mathbf{q}_A U_g - \mathbf{q}_B]$ is extracted by (4.13) with

$$S_{j,k} = \frac{1}{2 \left(1 - \cos \frac{\delta_{N,1}}{F}\right)} \cdot \begin{cases} \mathbf{C}_2^T \mathbf{M}_{j,1} (\mathbf{I} - \mathbf{M}_j^T) (\mathbf{M}_{N,1} - \mathbf{I}) (\mathbf{I} - \mathbf{M}_k) \mathbf{M}_{k,1}^T \mathbf{C}_2 & j < k \\ \mathbf{C}_2^T (\mathbf{M}_j^T - \mathbf{M}_{N,1}^T) (\mathbf{I} - \mathbf{M}_{N,1}) (\mathbf{I} - \mathbf{M}_k) \mathbf{C}_2 & j = k \\ \mathbf{C}_2^T \mathbf{M}_{j,1} (\mathbf{I} - \mathbf{M}_j^T) (\mathbf{I} - \mathbf{M}_{N,1}^T) (\mathbf{I} - \mathbf{M}_k) \mathbf{M}_{k,1}^T \mathbf{C}_2 & j > k \end{cases} \quad (4.15)$$

Exploiting some properties of rotation matrix $\mathbf{M}_{x,y}$, such as

- $\mathbf{M}_x^T = \mathbf{M}_{-x}$ (*transposition*),
- $\mathbf{M}_x \mathbf{M}_y = \mathbf{M}_{x+y}$ (*addition*),
- $\mathbf{M}_x \mathbf{M}_y^T = \mathbf{M}_{x-y}$, $\mathbf{M}_x^T \mathbf{M}_y = \mathbf{M}_{x-y}^T$ (*subtraction*),

and important identities like

- $\mathbf{M}_{N,1} + \mathbf{M}_{N,1}^T = 2 \cos \delta_{N,1} \cdot \mathbf{I}$
- $2(1 - \cos \delta_{N,1})(\mathbf{I} - \mathbf{M}_{N,1})^{-1} = \mathbf{I} - \mathbf{M}_{N,1}^T$

the final expression of $S_{j,k}$ is obtained as stated below

$$S_{j,k} = \frac{2 \sin \frac{\delta_j}{2F} \sin \frac{\delta_k}{2F}}{\sin \frac{\delta_{N,1}}{2F}} \sin \frac{\delta_{k,j} - \delta_{j,k}}{2F}. \quad (4.16)$$

The matrix \mathbf{S} is $N \times N$ skew-symmetric, i.e. $\mathbf{S} \in \text{Skew}_N$, because it is simple to check that $S_{j,k} = -S_{k,j}$ and $S_{j,j} = 0$. By the Skew_N properties, the term $\mathbf{q}_B^T \mathbf{S} \mathbf{q}_B = 0$ in (4.12), so that the final expression of Γ is

$$\Gamma = \frac{FU_g}{2\pi} \mathbf{q}_B^T \mathbf{S} \mathbf{q}_A. \quad (4.17)$$

In case of half-wave symmetry, as done in the section 4.1.1, the value of output power becomes dependent only on the first $N/2$ intervals and the matrix \mathbf{S} can be reduced to $\mathbf{S}' \in \mathbb{R}^{N/2 \times N/2}$ because the following simplification in (4.17) takes place

$$\begin{aligned} \mathbf{q}_B^T \mathbf{S} \mathbf{q}_A &= \sum_{j,k=1}^N q_{B,j} S_{j,k} q_{A,k} \\ &= \sum_{j,k=1}^{N/2} q_{B,j} [S_{j,k} + S_{N/2+j,k+N/2} - S_{N/2+j,k} - S_{j,k+N/2}] q_{A,k} \\ &= \mathbf{q}'_B{}^T \mathbf{S}' \mathbf{q}'_A. \end{aligned} \quad (4.18)$$

From (4.18) the final form of $S'_{j,k}$ is found as

$$S'_{j,k} = \frac{4 \sin \frac{\delta_j}{2F} \sin \frac{\delta_k}{2F}}{\cos \frac{\delta_{N/2,1}}{2F}} \begin{cases} -\cos \frac{\delta_{j,k} - \delta_{k,j}}{2F} & j < k \\ 0 & j = k \\ \cos \frac{\delta_{k,j} - \delta_{j,k}}{2F} & j > k \end{cases} \quad (4.19)$$

where the angle convention reported in Fig. 4.3b is used. Again, \mathbf{S}' is a skew-symmetric matrix, i.e. $\mathbf{S}' \in \text{Skew}_{N/2}$, and the normalized power definition from (4.17) becomes

$$\Gamma = \frac{FU_g}{2\pi} \mathbf{q}'_B{}^T \mathbf{S}' \mathbf{q}'_A. \quad (4.20)$$

4.1.3 Voltage Conversion Ratio

In case of resistive load, the output power can be linked to the resistance value R_o in the following normalized form

$$\Gamma = \frac{P_o}{P_{base}} = \frac{V_o^2}{R_o} \frac{Z_r}{V_{base}^2} = \frac{1}{\rho_o}. \quad (4.21)$$

Since (4.17) must be equal to (4.21) and U_g is the reciprocal of the voltage conversion ratio M , the latter is equal to

$$M = \frac{F \rho_o}{2\pi} \mathbf{q}_B^T \mathbf{S} \mathbf{q}_A. \quad (4.22)$$

4.1.4 General Considerations

This general approach permits to study also complex topologies where the duration of the intervals or the impressed voltage is dependent on the current, for example due to the presence of a rectifier at the output side employing unidirectional current devices like diodes. In this case, a known condition, e.g. zero-current state, is required to solve the topological state succession in terms of duration and initial conditions. Consequence of this dependency also appears in (4.22) turning it into an implicit formula, since \mathbf{S} becomes function of M .

In the following sections are considered the bidirectional Phase Shift Modulated (PSM) SR Dual Half Bridge (DHB) and the unidirectional Interleaved Boost with Coupled Inductors (IBCI) converters as examples. The first is obtained substituting the switching networks $\mathbf{S}_{w_{1,2}}$ in Fig. 4.1 with two HB legs as shown in Fig. 4.4a, while the second topology is depicted in Fig. 4.7. Both converter analyses are presented using the above-mentioned method to find the closed-form input-output characteristic functions with two different focuses: the PSM DHB topology described in Sec. 4.2 provides a simple application example easily comparable with FHA model. The IBCI topology, on the other hand, provides a complex example in which CCM and DCM modes are present and the boundary conditions have to be found in Sec. 4.3.

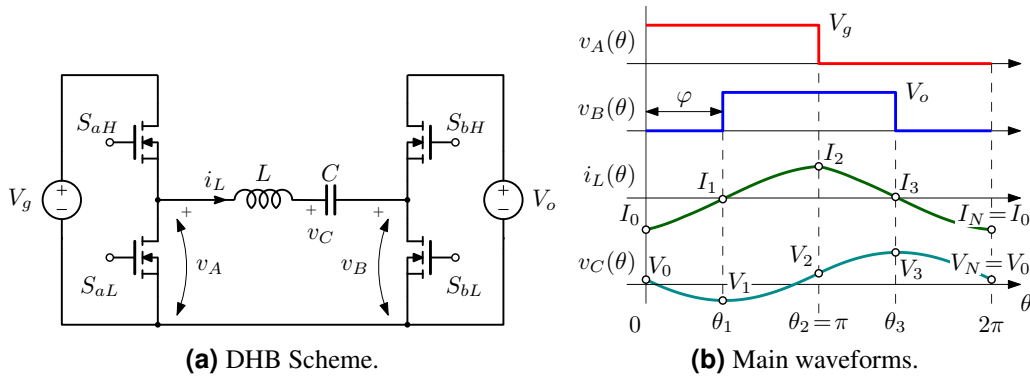


Figure 4.4: Scheme and main waveforms of SR PSM DHB.

4.2 Case Study 1: PSM SR DHB Converter

The Phase Shift Modulated Dual Half Bridge (PSM DHB) is a simple SR voltage-fed converter that is widely studied in the literature. In this section, the proposed method is first applied to briefly show its usability, and then compared with the corresponding FHA model.

4.2.1 Functional Description

Both impressed voltages $v_{A,B}(\theta)$ are two-level voltage square wave owing to the switching network implementation and the modulation scheme. The power transferring is achieved thanks to the phase shift φ between v_A and v_B voltages, which is also the control variable. The main converter waveforms are depicted in Fig. 4.4b highlighting the commutation instants θ_i and the corresponding state variable values (I_i V_i). The following analysis is limited to $\varphi \in [0, \frac{\pi}{2}]$ and $F > 0.5$. For $\varphi \in [-\frac{\pi}{2}, 0]$, the power flow reversal is obtained but the converter operation remains the same.

4.2.2 State-Space Analysis

The PSM DHB presents only one operating mode, i.e. CCM, so no boundary conditions have to be found. The converter is characterized by four topological states, as shown in Fig. 4.4b, and the corresponding definition of $\mathbf{q}_{A,B}$ vectors and interval durations δ_i , $i \in [1, 4]$, is reported in Table 4.2. It is worth noting that δ_i definition, as well as matrices \mathbf{W} and \mathbf{S} , are function of the control variable φ . Using (4.3) and (4.7), the normalized

Table 4.2: Definition of $\mathbf{q}_A, \mathbf{q}_B$ and δ_i for SR PSM DHB.

i	$q_{A,i}$	$q_{B,i}$	δ_i
1	1	0	φ
2	1	1	$\pi - \varphi$
3	0	1	φ
4	0	0	$\pi - \varphi$

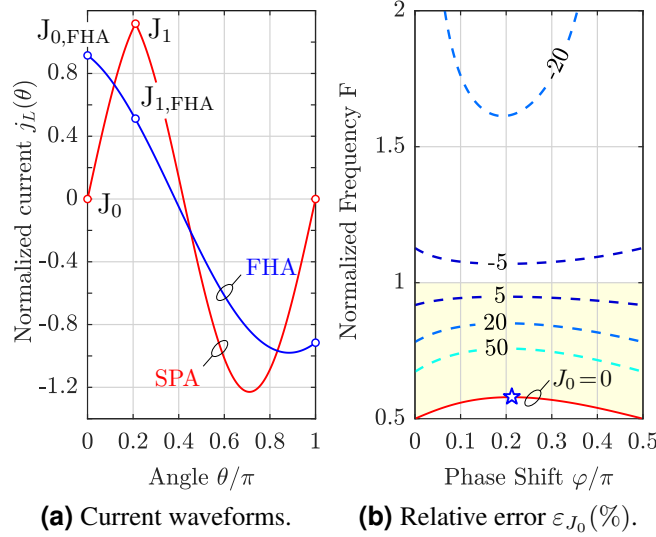


Figure 4.5: Comparison between FHA and SPA models. (a) Normalized current waveforms in a semi-period at $U_g = 12/5$, $\varphi^* = 0.21\pi$ and $F^* = 0.58$. For $\theta \in [\pi, 2\pi]$ the currents are equal to $-j_L(\theta - \pi)$. (b) Percentage relative error ε_{J_0} (isolines) between the (4.23a) and (4.25a) as a function of F and φ at $U_g = 12/5$. The red line represents the points satisfying $J_0 = 0$, where is highlighted the point (φ^*, F^*) . The yellow area indicates the region of positive values for J_0 .

expressions of $I_{0,1}$ are:

$$J_0 = \frac{1}{2 \cos \frac{\pi}{2F}} \left[-U_g \sin \frac{\pi}{2F} + \sin \frac{\pi - 2\varphi}{2F} \right], \quad (4.23a)$$

$$J_1 = \frac{1}{2 \cos \frac{\pi}{2F}} \left[-U_g \sin \frac{\pi - 2\varphi}{2F} + \sin \frac{\pi}{2F} \right]. \quad (4.23b)$$

These expressions contain information about ZVS and ZCS conditions: the locus of points (φ, F) where (4.23) is zero identifies a ZCS condition, while ZVS can be evaluated studying the sign of (4.23) in the (φ, F) -plane. An example is depicted in Fig. 4.5b at $U_g = 12/5$: the red line satisfy $J_0 = 0$, while the highlighted yellow region solve $J_0 > 0$. To compare the previous results with the outcomes of the FHA method, the sampled values of the cur-

rent phasor at $\theta_{0,1}$ are calculated from the general normalized current expression

$$j_{FHA}(\theta) = \frac{2}{\pi} \frac{F}{F^2 - 1} \Re \{ (e^{-j\varphi} - U_g) e^{j\theta} \} \quad (4.24)$$

as follows:

$$J_{0,FHA} = \frac{2}{\pi} \frac{F}{F^2 - 1} [\cos \varphi - U_g], \quad (4.25a)$$

$$J_{1,FHA} = \frac{2}{\pi} \frac{F}{F^2 - 1} [1 - U_g \cos \varphi]. \quad (4.25b)$$

Differently from the exact analysis, (4.25a) never zeros for $U_g > 1$ as well as (4.25b) for $U_g < 1$. This information loss affects both the soft and hard switching estimation, especially in below resonance operation as shown in Fig. 4.5a for $U_g = 12/5$, $\varphi^* = 0.21\pi$ and $F^* = 0.58$. The FHA model in the considered scenario, i.e. $0.5 < F < 1$, provides a wrong estimation of commutated currents. The relative error $\varepsilon_{J_0} = \frac{J_{0,FHA}}{J_0} - 1$ plotted in Fig. 4.5b in the (φ, F) -plane, reveals the importance of an accurate prediction of the current at the commutation instants for a correct switching loss estimation. Once again, such error rapidly increases entering the below resonance region.

Now focusing on the power, the necessary elements of \mathbf{S} in (4.17) are the set of $S_{j,k}$ such that $j \neq k$, $q_{A,k} \neq 0$ and $q_{B,j} \neq 0$ since $q_{B,j} S_{j,k} q_{A,k} = 0$ for the others. Then the useful matrix elements are

$$S_{2,1} = S_{3,2} = \frac{\sin \frac{\varphi}{2F} \sin \frac{\pi - \varphi}{2F}}{\cos \frac{\pi}{2F}}, \quad S_{3,1} = 0, \quad (4.26)$$

that provide the normalized output power Γ equation through (4.17) as

$$\Gamma = \frac{F}{\pi} U_g \frac{\sin \frac{\varphi}{2F} \sin \frac{\pi - \varphi}{2F}}{\cos \frac{\pi}{2F}}. \quad (4.27)$$

Performing the FHA analysis, the normalized output power Γ_{FHA} is given by

$$\Gamma_{FHA} = \frac{2}{\pi^2} U_g \frac{F}{F^2 - 1} \sin \varphi. \quad (4.28)$$

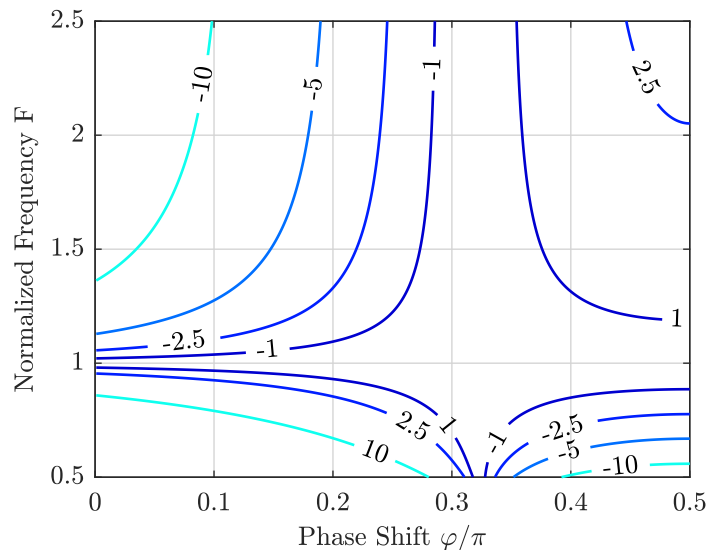


Figure 4.6: Percentage relative error between (4.28) and (4.27), i.e. $\epsilon_{r\%} = 100 \left(\frac{\Gamma_{FHA}}{\Gamma} - 1 \right)$, as a function of the normalized frequency F and the phase shift angle φ .

The discrepancy between (4.27) and (4.28) is plotted in Fig. 4.6 in term of percentage relative error as a function of the normalized frequency F and the normalized phase shift angle $\frac{\varphi}{\pi}$. As shown in Fig. 4.6, the closer operating point (φ, F) gets to the axes, the more discrepancy is between the two approaches surpassing even the 10% in magnitude.

4.3 Case Study 2: IBCI Converter

The IBCI topology reported in Fig. 4.7 belongs to the current-fed converter family cited in the introduction, and has been previously studied in [45], as non-resonant topology, while the analysis of the resonant case is reported in [61], [69], for the above-resonance case only. The coexistence of both CCM and DCM modes in the said unidirectional topology requires to find the related boundary conditions needing a further step in the analysis. In this section the survey has been extended in the below-resonance mode validating the previous solving method, providing a guideline to help the reader in the analysis steps.

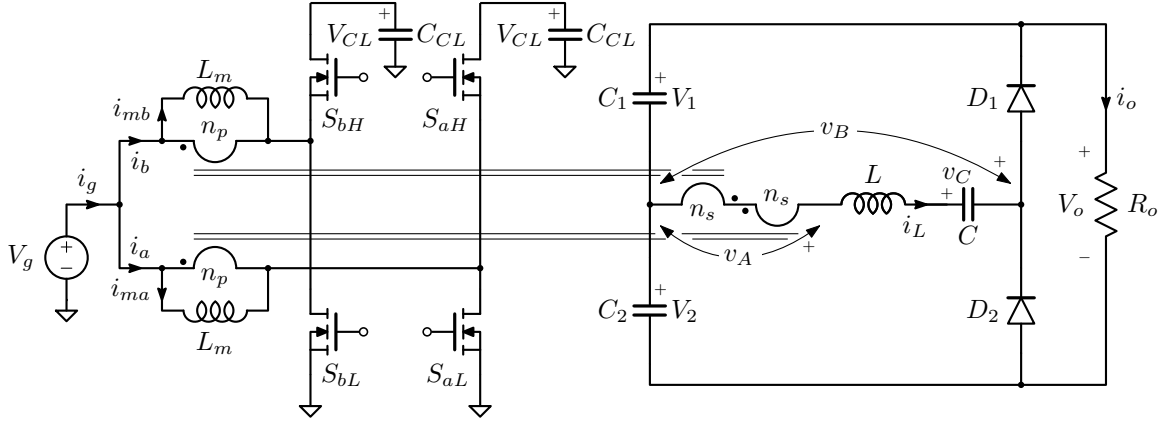


Figure 4.7: Interleaved Boost with Couple Inductors (IBCI): the impressed voltages $v_{A,B}$ are highlighted as well as the state-space variables (i_L v_C) respectively the current through the total leakage inductor L and the resonant capacitor voltage C .

4.3.1 Functional Description

The IBCI converter transfers the energy between the input and output ports through the LC-series impedance composed by the total leakage inductance L of the mutual inductors and the resonant capacitance C , both indicated in Fig. 4.7. Considering negligible the voltage ripple across the clamp and output capacitors, C_{CL} and $C_{1,2}$, the converter works like the equivalent circuit of Fig. 4.1. The impressed voltage $v_A(\theta)$ is a three-level voltage waveform given by the two series-connected secondary windings (see Fig. 4.8). Due to the interleaved operation, the positive (and negative) pulse duration β is a symmetrical function of the duty-cycle D , which is the control variable, around $D = 0.5$:

$$\beta = \begin{cases} 2\pi D & \text{when } D \leq 0.5 \\ 2\pi(1 - D) & \text{when } D > 0.5 \end{cases}. \quad (4.29)$$

The *volt-second* balance across each magnetizing inductance L_m yields the clamp capacitor voltage V_{CL} which is reflected to the transformer secondary side returning the peak amplitude V_A as

$$V_A = \frac{V_g}{n(1 - D)}, \quad (4.30)$$

where $n = n_p/n_s$ is the turns ratio of each coupled inductor.

Instead, the voltage $v_B(\theta)$ is a two-level waveform (CCM operation) whose peak am-

plitude V_B is equal to either half output voltage, using a voltage doubler rectifier like in Fig. 4.7, or the whole output voltage, when a standard full-wave rectifier is used. In order to account for both cases, the voltage gain parameter $G \in \{0.5, 1\}$ is introduced, therefore $V_B = GV_o$ in the general case. Clearly, if a different rectifier stage is used like in [48], G will assume a different value (in this case 0.25). The condition $V_A \geq V_B$ is necessary to obtain a positive energy transfer from source to load.

4.3.2 State-Space Analysis

Since the IBCI converter presents a half-wave symmetry in the impressed voltage waveforms, only a semi-period needs to be taken into account in the analysis using the angle convention illustrated in Fig. 4.3b. Limiting the study for $F > 0.5$ and for the operating modes in which the inductor current i_L changes sign only one time in a switching period, the IBCI converter shows three Continuous and three Discontinuous Conduction Modes reported as CCM_i and DCM_i ($i = 0, 1, 2$) in Fig. 4.8 for $D > 0.5$. For CCM modes the considered number of intervals is $N/2 = 3$, while for DCM modes $N/2 = 2$ for $DCM_{0,1}$ and $N/2 = 1$ for DCM_2 , since only active states are considered, i.e. the sub-intervals where the inductor current remains zero are ignored (see Fig. 4.8).

For any operating mode, the initial state \mathbf{x}_0 is set at the instant the inductor current i_L starts rising above zero. As a consequence, the current is always positive in the considered half switching period, and the impressed voltage is constant and equals to GV_o , so that $\mathbf{q}'_B = G\mathbf{1}$ with $\mathbf{1} = [1 \dots 1]^T$. This choice permits a further simplification in (4.20). In fact

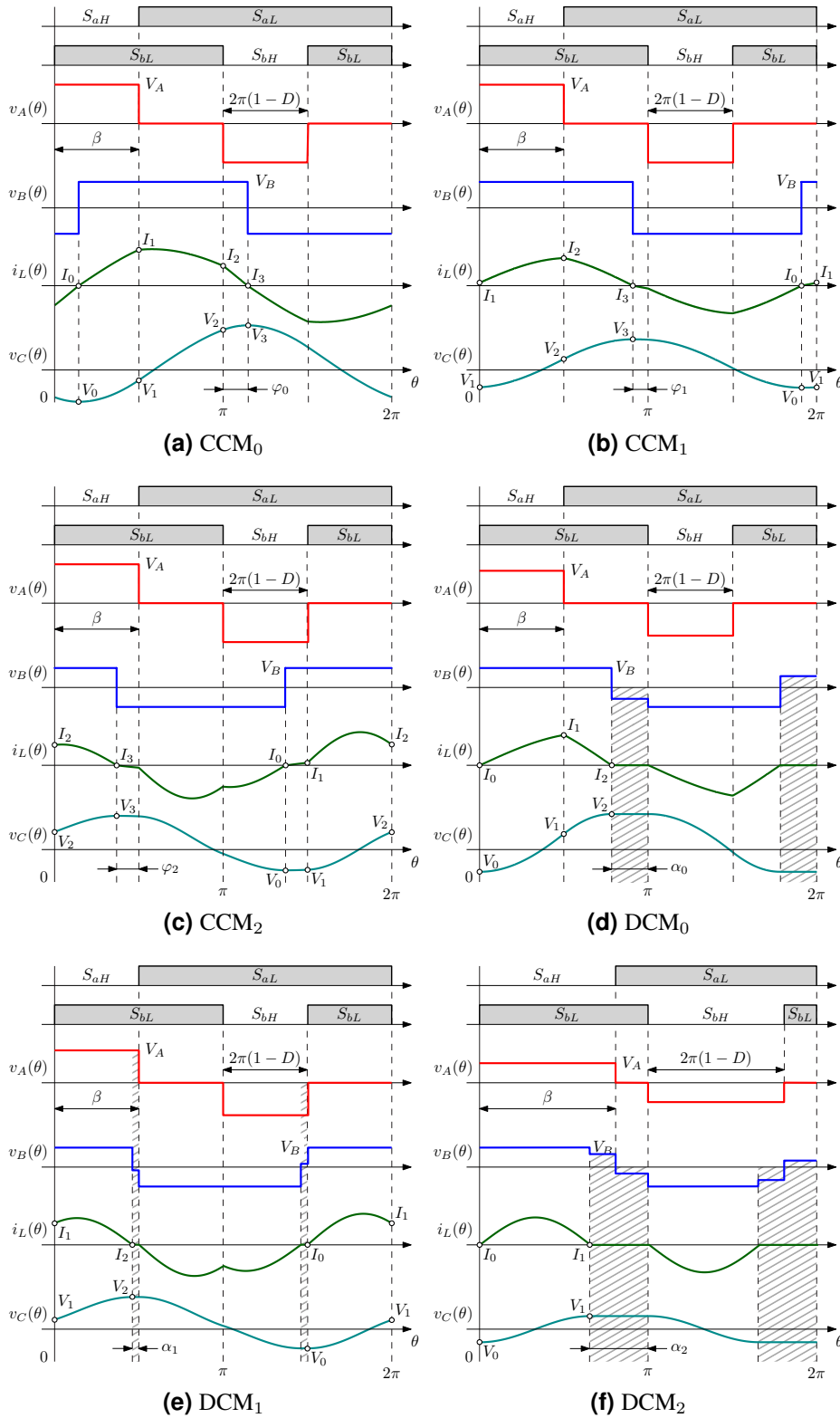


Figure 4.8: Main converter waveforms in different CCM and DCM operation modes for $D > 0.5$. The waveforms related to $D < 0.5$ case are just scaled replicas of those obtained for $D > 0.5$. The grey-filled intervals won't be considered in the DCM analysis.

the k -th element of $\mathbf{q}_B^T \mathbf{S}'$ is equal to

$$\begin{aligned}
 (\mathbf{q}_B^T \mathbf{S}')_k &= G(\mathbf{1}^T \mathbf{S}')_k \\
 &= G \frac{4 \sin \frac{\delta_k}{2F}}{\cos \frac{\delta_{N/2,1}}{2F}} \left\{ \sum_{j=k+1}^{N/2} \sin \frac{\delta_j}{2F} \cos \frac{\delta_{k,j} - \delta_{j,k}}{2F} - \sum_{j=1}^{k-1} \sin \frac{\delta_j}{2F} \cos \frac{\delta_{j,k} - \delta_{k,j}}{2F} \right\} \\
 &= G \frac{2 \sin \frac{\delta_k}{2F}}{\cos \frac{\delta_{N/2,1}}{2F}} \left\{ \left(\sin \frac{\delta_{N/2,1} - \delta_k}{2F} + \sin \frac{\delta_{N/2,k} - \delta_{k,1}}{2F} \right) + \dots \right. \\
 &\quad \left. \dots + \left(\sin \frac{\delta_{N/2,k} - \delta_{k,1}}{2F} - \sin \frac{\delta_{N/2,1} - \delta_k}{2F} \right) \right\} \\
 &= G \frac{4 \sin \frac{\delta_k}{2F}}{\cos \frac{\delta_{N/2,1}}{2F}} \sin \frac{\delta_{N/2,k} - \delta_{k,1}}{2F}
 \end{aligned} \tag{4.31}$$

that is equal to $-4G\mathbf{C}_2^T \mathbf{w}'_k$, as obtainable from (4.9). Using (4.31) in (4.17), the power definition modifies as follows:

$$\Gamma = -\frac{2FG}{\pi} U_g \mathbf{C}_2^T \mathbf{W}' \mathbf{q}'_A. \tag{4.32}$$

The above expression can be further simplified by correlating the term $\mathbf{W}' \mathbf{q}'_A$ with the initial state vector \mathbf{x}_0 given in (4.10). In fact, the term $\mathbf{W}' \mathbf{1}$, which expression is given by

$$\begin{aligned}
 \mathbf{W}' \mathbf{1} &= \frac{1}{2 \cos \frac{\delta_{N/2,1}}{2F}} \begin{bmatrix} \sum_{k=1}^{N/2} \sin \frac{\delta_{N/2,k+1} - \delta_{k,1}}{2F} - \sum_{k=1}^{N/2} \sin \frac{\delta_{N/2,k} - \delta_{k-1,1}}{2F} \\ - \sum_{k=1}^{N/2} \cos \frac{\delta_{N/2,k+1} - \delta_{k,1}}{2F} + \sum_{k=1}^{N/2} \cos \frac{\delta_{N/2,k} - \delta_{k-1,1}}{2F} \end{bmatrix} \\
 &= \frac{-1}{\cos \frac{\delta_{N/2,1}}{2F}} \begin{bmatrix} \sin \frac{\delta_{N/2,1}}{2F} \\ 0 \end{bmatrix},
 \end{aligned} \tag{4.33}$$

when multiplied by \mathbf{C}_2^T gives zero. Thus we can write:

$$\Gamma = -\frac{2FG}{\pi} U_g \mathbf{C}_2^T \mathbf{W}' \mathbf{q}'_A = -\frac{2FG}{\pi} \mathbf{C}_2^T \mathbf{W}' [\mathbf{q}'_A U_g - G\mathbf{1}] = -\frac{2FG}{\pi} \mathbf{C}_2^T \mathbf{x}_0 = -\frac{2FG}{\pi} U_0. \tag{4.34}$$

This result can be traced easily back to (4.12) where the summation is simplified as $\sum_i (U_i -$

Table 4.3: Definition of $\mathbf{q}'_A, \mathbf{q}'_B$ and δ_i for CCM₁ mode.

i	$q'_{A,i}$	$q'_{B,i}$	δ_i
1	0	G	φ_1
2	$G\lambda$	G	β
3	0	G	$\pi - \beta - \varphi_1$

$U_{i-1}) = U_{N/2} - U_0 = -2U_0$. With the same tricks, the voltage gain M reported in (4.22) becomes

$$M = -\frac{2FG\rho_o}{\pi} \mathbf{C}_2^T \mathbf{W}' \mathbf{q}'_A. \quad (4.35)$$

The hereunder analysis guideline explains how to reach the closed-form expressions of normalized output power Γ , voltage conversion ratio M and the operating boundaries for CCM₁ mode, depicted in Fig. 4.8b. The same procedure has been applied to the other operating modes, paying particular attention to DCM modes as described afterwards.

1. *Identify the topological state sequence* in the form of the applied voltage u_Z , thus defining the $\mathbf{q}'_{A,B}$ vectors and relative angles δ_i , as reported in Table 4.3. The characteristic angle φ_1 is introduced as the phase-shift between the positive-pulse rising-edges of voltages v_A and v_B , as depicted in Fig. 4.8b. It is worth to highlight that δ_i are function of the control variable β and the current-sign dependent variable φ_1 . For the sake of readability, the dimensionless factor λ is introduced as

$$\lambda = \frac{1}{nG(1-D)}, \quad (4.36)$$

and (4.7) provides the initial state \mathbf{x}_0 :

$$J_0 = \frac{G}{\cos \frac{\pi}{2F}} \left[\sin \frac{\pi}{2F} - \lambda U_g \sin \frac{\beta}{2F} \cos \frac{\pi - \beta - 2\varphi_1}{2F} \right], \quad (4.37a)$$

$$U_0 = -\frac{G\lambda U_g}{\cos \frac{\pi}{2F}} \sin \frac{\beta}{2F} \sin \frac{\pi - \beta - 2\varphi_1}{2F}. \quad (4.37b)$$

In general, each topological state sequence is decided a priori, following the common sense or just guessing. The non-existence of the selected sequence is translated in no intersection between the constraints provided in the following steps.

2. *Find the CCM (or DCM) condition.* For CCM modes, at the instant $\theta_{N/2}$ the inductor current i_L changes sign and starts to flow through diode D_2 changing the u_B voltage polarity. For CCM operation, is necessary that the inductor voltage v_L is negative in the right neighbourhood of $\theta_{N/2}$, i.e. $u_L(\theta_{N/2}^+) = U_{Z,N/2+1} - U_{N/2} < 0$, otherwise the current will be null in the next topological state (DCM case). Due to the half-wave symmetry, the same condition can be reflected to the initial state \mathbf{x}_0 , just reversing the voltage polarities, giving

$$U_{Z,1} - U_0 > 0 \quad \rightarrow \quad U_g q'_{A,1} - U_0 > q'_{B,1} \quad (4.38)$$

and in the particular CCM₁ case for which $q'_{A,1} = 0$:

$$-U_0 > G. \quad (4.39)$$

3. *Extract the characteristic angle φ_1 .* In CCM₁ case, imposing (4.37a) equals to zero and rearranging (4.37b) the cosine (4.40a) and sine (4.40b) of the same angle, function of φ_1 , are obtained as

$$\cos \frac{\pi - \beta - 2\varphi_1}{2F} = \frac{1}{\lambda U_g} \frac{\sin \frac{\pi}{2F}}{\sin \frac{\beta}{2F}}, \quad (4.40a)$$

$$\sin \frac{\pi - \beta - 2\varphi_1}{2F} = -\frac{U_0}{G\lambda U_g} \frac{\cos \frac{\pi}{2F}}{\sin \frac{\beta}{2F}}. \quad (4.40b)$$

The (4.40a) is always positive, on the other hand (4.40b) is positive for $F > 1$ and negative for $F \in [\frac{1}{2}, 1]$ due to the right-side cosine term and the negative value of U_0 derived from (4.39). Consequently, (4.40) represents an angle that lies on the I or IV quadrant, which is

translated in the \mp sign in the following φ_1 expression:

$$\varphi_1 = \frac{\pi - \beta}{2} \mp F \arccos \left(\frac{1 \sin \frac{\pi}{2F}}{\lambda U_g \sin \frac{\beta}{2F}} \right). \quad (4.41)$$

4. Find the feasible operating region constraining each interval to be positive and lower than half resonant period, i.e.:

$$0 < \delta_i < \pi F, \quad i \in [1, N/2]. \quad (4.42)$$

The lower limit is obvious while the upper limit is necessary to eliminate the solutions where output impressed voltage \mathbf{q}'_B is incoherent with the inductor current sign because a further zero-crossing takes place. Limit case is DCM₂ mode where the unique active interval lasts a resonant semi-period, i.e. πF , and the inductor current performs a complete semi-cycle as depicted in Fig. 4.8f and described in detail afterwards. In the considered case (see Table 4.3), the most restrictive inequalities got from (4.42) are

$$\beta < \pi F, \quad (4.43a)$$

$$\varphi_1 < \pi F, \quad (4.43b)$$

$$0 < \varphi_1 < \pi - \beta. \quad (4.43c)$$

The (4.43a) just identifies a semi-plane in the (F, β) -plane, while (4.43b) and (4.43c) must be separately discussed for $0.5 < F < 1$ and $F > 1$ because of the different definition of φ_1 in (4.41).

Case $0.5 < F < 1$. The lower limit in (4.43c) doesn't provide any restriction, on the other hand, the upper limit returns the following inequality

$$\frac{1 \sin \frac{\pi}{2F}}{\lambda U_g \sin \frac{\beta}{2F}} > \cos \frac{\pi - \beta}{2F}. \quad (4.44)$$

The left-side term is always positive in the considered range ($F > 0.5$), then (4.44) is

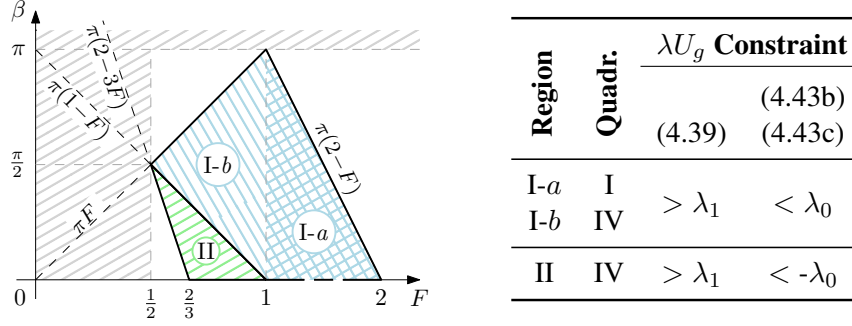


Figure 4.9: CCM₁ operating region: in the table are highlighted the constraints given by the reported inequalities expressed in function of λU_g and the quadrant of the angle in (4.40).

always true for $\beta < \pi(1 - F)$ where cosine term is negative, otherwise it is verified on condition that

$$\lambda U_g < \lambda_0 = \frac{\sin \frac{\pi}{2F}}{\sin \frac{\beta}{2F} \cos \frac{\pi - \beta}{2F}}. \quad (4.45)$$

Similarly, (4.43b) forces the normalized voltage U_g to be

$$\lambda U_g < -\lambda_0. \quad (4.46)$$

in the semi-plane $\beta < \pi(1 - F)$ only.

Case $F > 1$. The inequalities (4.43a) and (4.43b) are always verified, while the upper limit of (4.43c) returns (4.45) again.

Another constraint comes from (4.39) substituting (4.40a) in (4.37b) giving the following inequality in the whole interested range:

$$\lambda U_g > \lambda_1 = \frac{1}{\sin \frac{\beta}{2F}}. \quad (4.47)$$

Now, all these constraints must coexist in the (F, β) -plane as depicted in Fig. 4.9: (4.45) and (4.47) admit common solution if and only if $\lambda_0 > \lambda_1$, that is true for $F > 1$ with $\beta < \pi(2 - F)$ (Region I-a), and for $0.5 < F < 1$ with $\beta < \pi F$ (Region I-b); (4.46) and (4.47) are simultaneously true if only if $-\lambda_0 > \lambda_1$ that implies $\beta > \pi(2 - 3F)$ (Region II).

The λ_i functions correspond to the normalized voltage λU_g at the frontiers between different operating modes. In the considered range, the IBCI converter presents three voltage

Table 4.4: Voltage and power mode boundaries definitions of λU_g and Γ .

i	λ_i	Γ_i
0	$\frac{\sin \frac{\pi}{2F}}{\sin \frac{\beta}{2F} \cos \frac{\pi-\beta}{2F}}$	$\frac{2FG^2}{\pi} \left \tan \frac{\pi}{2F} \right \tan \frac{\pi-\beta}{2F}$
1	$\frac{1}{\sin \frac{\beta}{2F}}$	$\frac{2FG^2}{\pi}$
2	$\frac{1}{\cos \frac{\pi-\beta}{2F}}$	$\frac{2FG^2}{\pi} \left[1 + \frac{1}{\cos \frac{\pi-\beta}{2F}} \right]$

boundaries $\lambda_{0,1,2}$, reported in Table 4.4, in addition to $\lambda U_g = 1$ that corresponds to the limit of positive power flow condition, i.e. $V_A \geq V_B$.

5. Find the normalized output power and the voltage conversion ratio applying (4.32) and (4.35). For CCM₁ mode, substituting in (4.32) the value of φ_1 given in (4.41), the normalized power in function of U_g is obtained:

$$\Gamma = \frac{2FG^2}{\pi} \lambda U_g \frac{\sin \frac{\beta}{2F}}{\left| \cos \frac{\pi}{2F} \right|} \sqrt{1 - \left(\frac{1}{\lambda U_g} \frac{\sin \frac{\pi}{2F}}{\sin \frac{\beta}{2F}} \right)^2}. \quad (4.48)$$

Substituting the voltage boundary values $\lambda_{0,1}$ in (4.48) the corresponding power boundaries values $\Gamma_{0,1}$ are found. At every λ_i is associated its Γ_i value as reported in Table 4.4. Using (4.35) and remembering that $U_g = M^{-1}$, the explicit value of the conversion ratio is found as:

$$M = \frac{2FG^2 \rho_o}{\pi} \lambda \frac{\sin \frac{\beta}{2F}}{\left| \cos \frac{\pi}{2F} \right|} \frac{1}{\sqrt{1 + \left(\frac{2FG^2 \rho_o}{\pi} \tan \frac{\pi}{2F} \right)^2}}. \quad (4.49)$$

Iterating this presented procedure for all the modes depicted in Fig. 4.8, the different regions in the (F, β) -plane and normalized frontiers of λU_g and Γ are figured out. The Table 4.5 contains the initial state x_0 for all the considered modes. The unknown angles, function of the phase shift φ_i for CCM modes or the dead angle α_i for DCM modes, is highlighted in the table. As previously done in the point 3, the sign of the unknown angle allows to obtain the right expression of the related characteristic angle. The Tables 4.6-4.7 report the (F, β) -plane existence regions, the normalized frontiers of λU_g and Γ for CCM

and DCM modes respectively. As the last, in Tables 4.8-4.9 the expressions of normalized power and characteristic angles (φ for CCM and α for DCM modes) as well are summarized.

The DCM₂ mode, which is the resonant mode mostly exploited in literature (see [63]–[66]), deserves a particular discussion because $\delta_{N/2,1} = \pi F$, turning \mathbf{W}' and \mathbf{S}' meaningless. In this mode, the converter behaves like a voltage source, since its voltage gain $M = \lambda$ is independent of the load, as easily obtained from (4.3). Applying (4.38) both at the end of the resonant semi-period and at the falling edge of v_A , the condition $-G < U_0 < 0$ is obtained and substituting it in (4.34) the power boundary $\Gamma < \Gamma_1$ is achieved (see Tables 4.7–4.8).

It is worth mentioning that the presented analysis, can be immediately extended to the voltage-fed counterpart topologies just making the input parameter λ independent of control variable, and setting $\lambda \in \{0.5, 1\}$ in case of half or full bridge usage respectively. It is also useful to highlight that the non-resonant behaviour can be simply obtained assuming $F \gg 1$.

Switching Node Current Analysis

As aforementioned in the introduction, the proposed framework is able to provide a reasonable estimation of the switching node current at the commutation instants. The knowledge of their values permits to have a first evaluation of the switching losses and recognize the limits of the studied topology accordingly. Let us take into account the switching node current of the leg a , namely the current i_a depicted in Fig. 4.7. The current i_a is equal to the difference between the magnetizing current i_{ma} and the resonant current i_L reflected on the primary side, in formula $i_a = i_{ma} - \frac{i_L}{n}$. The two interested values are I_{LH} and I_{HL} , that are the sampled values of i_a when the switch S_{aL} turns off and S_{aH} is going to turn on, and vice-versa, respectively. They depend on both the duty-cycle and the operating mode, as shown in Fig. 4.10 for CCM₁ mode. In Table 4.10, all the values of $I_{LH,HL}$ for each combinations of duty cycle and operating mode are given: the peak and valley values of i_m

Table 4.5: Closed form expressions of the initial state \mathbf{x}_0 for $\text{CCM}_i, \text{DCM}_i$ modes.

Mode	Initial state \mathbf{x}_0
CCM_0	$J_0 = \frac{G}{\cos \frac{\pi}{2F}} \left[\sin \frac{\pi}{2F} - \lambda U_g \cos \frac{\pi-\beta}{2F} \sin \frac{\beta-2\varphi_0}{2F} \right]$
	$U_0 = \frac{G\lambda U_g}{\cos \frac{\pi}{2F}} \left[\cos \frac{\pi}{2F} - \cos \frac{\pi-\beta}{2F} \cos \frac{\beta-2\varphi_0}{2F} \right]$
CCM_1	$J_0 = \frac{G}{\cos \frac{\pi}{2F}} \left[\sin \frac{\pi}{2F} - \lambda U_g \sin \frac{\beta}{2F} \cos \frac{\pi-\beta-2\varphi_1}{2F} \right]$
	$U_0 = -\frac{G\lambda U_g}{\cos \frac{\pi}{2F}} \sin \frac{\beta}{2F} \sin \frac{\pi-\beta-2\varphi_1}{2F}$
CCM_2	$J_1 = \frac{G}{\cos \frac{\pi}{2F}} \left[\sin \frac{\pi}{2F} - \lambda U_g \cos \frac{\pi-\beta}{2F} \sin \frac{\beta-2\varphi_2}{2F} \right]$
	$U_0 = \frac{G\lambda U_g}{\cos \frac{\pi}{2F}} \left[\cos \frac{\pi}{2F} - \cos \frac{\pi-\beta}{2F} \cos \frac{\beta-2\varphi_2}{2F} \right]$
DCM_0	$J_0 = G \left[\tan \frac{\pi-\alpha_0}{2F} - \lambda U_g \left(\tan \frac{\pi-\alpha_0}{2F} \sin^2 \frac{\beta}{2F} + \sin \frac{\beta}{2F} \cos \frac{\beta}{2F} \right) \right]$
	$U_0 = G\lambda U_g \sin \frac{\beta}{2F} \left[\tan \frac{\pi-\alpha_0}{2F} \cos \frac{\beta}{2F} - \sin \frac{\beta}{2F} \right]$
DCM_1	$J_0 = G \left[\tan \frac{\pi-\alpha_1}{2F} - \lambda U_g \cos \frac{\pi-\beta}{2F} \left(\tan \frac{\pi-\alpha_1}{2F} \cos \frac{\pi-\beta}{2F} - \sin \frac{\pi-\beta}{2F} \right) \right]$
	$U_0 = G\lambda U_g \sin \frac{\pi-\beta}{2F} \left[\tan \frac{\pi-\alpha_1}{2F} \cos \frac{\pi-\beta}{2F} - \sin \frac{\pi-\beta}{2F} \right]$
DCM_0	$J_0 = 0$
	$U_0 = -\frac{\pi\Gamma}{2F}$

Table 4.6: CCM mode regions and $\lambda U_g/\Gamma$ -boundaries.

CCM Region	Normalized Boundaries		
	(F, β) -plane	Voltage λU_g	Power Γ
0	$F > 1$	$\lambda U_g > \lambda_0$	$\Gamma > \Gamma_0$
1	I	$\lambda_1 < \lambda U_g < \lambda_0$	$\Gamma_1 < \Gamma < \Gamma_0$
	II		
2	I	$\lambda U_g > \lambda_2$	$\Gamma > \Gamma_2$
	II	$\lambda U_g > \lambda_0$	$\Gamma > \Gamma_0$

Table 4.7: DCM mode regions and $\lambda U_g/\Gamma$ -boundaries.

DCM Region	Normalized Boundaries		
	(F, β) -plane	Voltage λU_g	Power Γ
0	I	$1 < \lambda U_g < \lambda_1$	$\Gamma < \Gamma_1$
	II		
1	I	$1 < \lambda U_g < \lambda_2$	$\Gamma_1 < \Gamma < \Gamma_2$
	II		
	II		
2	$\beta > \pi F$	$\lambda U_g = 1$	$\Gamma < \Gamma_1$

Table 4.8: Closed form expressions of normalized power Γ for CCM_{*i*},DCM_{*i*} modes.

Mode	Normalized Output Power Γ
CCM ₀	$\frac{2FG^2}{\pi} \lambda U_g \left[-1 + \frac{\cos \frac{\pi-\beta}{2F}}{\cos \frac{\pi}{2F}} \sqrt{1 - \sin^2 \frac{\beta-2\varphi_0}{2F}} \right]$
CCM ₁	$\frac{2FG^2}{\pi} \lambda U_g \frac{\sin \frac{\beta}{2F}}{\left \cos \frac{\pi}{2F} \right } \sqrt{1 - \cos^2 \frac{\pi-\beta-2\varphi_1}{2F}}$
CCM ₂	$\frac{2FG^2}{\pi} \lambda U_g \left[1 - \frac{\cos \frac{\pi-\beta}{2F}}{\cos \frac{\pi}{2F}} \sqrt{1 - \sin^2 \frac{\beta-2\varphi_2}{2F}} \right]$
DCM ₀	$\frac{2FG^2}{\pi} \lambda U_g \frac{(\lambda U_g - 1) \sin^2 \frac{\beta}{2F}}{1 - \lambda U_g \sin^2 \frac{\beta}{2F}}$
DCM ₁	$\frac{2FG^2}{\pi} \lambda U_g \frac{\sin^2 \frac{\pi-\beta}{2F}}{1 - \lambda U_g \cos^2 \frac{\pi-\beta}{2F}}$
DCM ₂	$\forall \Gamma : \lambda U_g = 1$

Table 4.9: Closed form expressions of characteristic angles φ_i, α_i for CCM_{*i*},DCM_{*i*} modes.

Mode	Typical Angle φ_i/α_i
CCM ₀	$\varphi_0 = \frac{\beta}{2} - F \arcsin \left(\frac{1}{\lambda U_g} \frac{\sin \frac{\pi}{2F}}{\cos \frac{\pi-\beta}{2F}} \right)$
CCM ₁	$\varphi_1 = \frac{\pi - \beta}{2} \mp F \arccos \left(\frac{1}{\lambda U_g} \frac{\sin \frac{\pi}{2F}}{\sin \frac{\beta}{2F}} \right)$
CCM ₂	$\varphi_2 = \frac{\beta}{2} - F \arcsin \left(\frac{1}{\lambda U_g} \frac{\sin \frac{\pi}{2F}}{\cos \frac{\pi-\beta}{2F}} \right)$
DCM ₀	$\alpha_0 = \pi - 2F \arctan \left(\frac{\lambda U_g \sin \frac{\beta}{2F} \cos \frac{\beta}{2F}}{1 - \lambda U_g \sin^2 \frac{\beta}{2F}} \right)$
DCM ₁	$\alpha_1 = \pi(1 - 2F) + 2F \arctan \left(\frac{\lambda U_g \sin \frac{\beta}{2F} \cos \frac{\beta}{2F}}{1 - \lambda U_g \cos^2 \frac{\beta}{2F}} \right)$
DCM ₂	$\alpha_2 = \pi(1 - F)$

4.3. Case Study 2: IBCI Converter

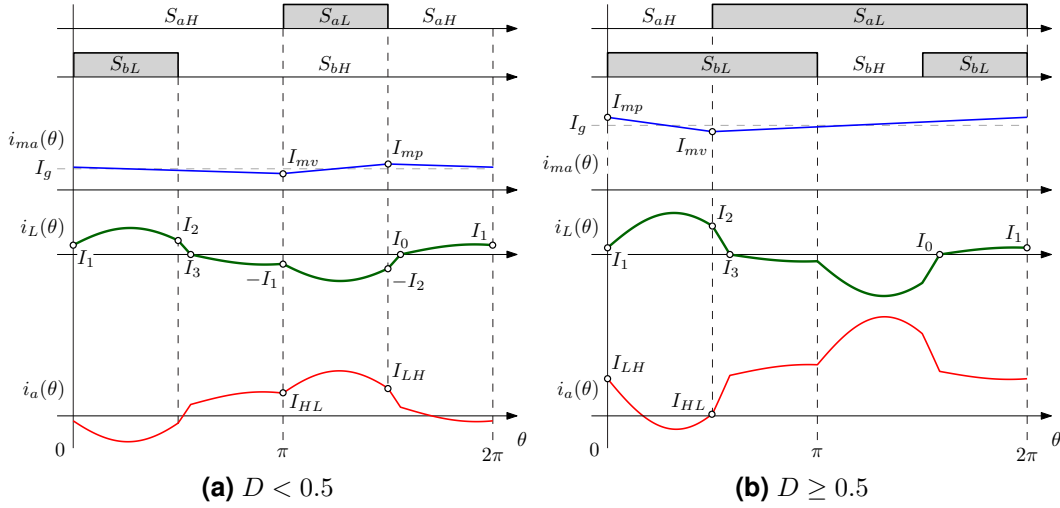


Figure 4.10: Current waveforms at node a in CCM_1 mode for (a) $D < 0.5$ and (b) $D \geq 0.5$.

are indicated with I_{mp} and I_{mv} (see Fig. 4.10), and they are given by

$$I_{mp,mv} = \frac{I_g}{2} \pm \frac{DV_g}{2f_{sw}L_m}, \quad (4.50)$$

where I_g is the average input current. Instead, the resonant current values I_i , also reported in Fig. 4.8, can be derived from Table 4.5 using (4.3) to move through the sampled trajectories. In this case study, these values can be immediately found exploiting the smart choice of the intervals: the initial state \mathbf{x}_0 is already defined, in fact $J_0 = 0$ by hypothesis and $U_0 = -\frac{\pi\Gamma}{2FG}$ according to (4.34), then the normalized value of I_1 is

$$J_1 = (U_{Z,1} - U_0) \sin \frac{\delta_1}{F}. \quad (4.51)$$

Instead to use (4.3) to move from J_1 to J_2 , the half-wave symmetry can be exploited, i.e. $\mathbf{x}_0 = -\mathbf{x}_{N/2}$, so J_2 is found moving backward from the state \mathbf{x}_3 using (4.3) as well:

$$J_2 = -(U_{Z,3} + U_0) \sin \frac{\delta_3}{F}. \quad (4.52)$$

However, some information about the sign of switching current can be immediately derived because the inductor current is always positive in the considered semi-period. Talking into account Table 4.10, the reported values that are highlighted with the symbols (1) always

Table 4.10: Switching node current at LH and HL transitions. Under the hypothesis of positive magnetizing current, the symbols (·) indicates the possibility of ZVS and/or ZCS transitions as follow: (1) always ZVS (2) ZVS or ZCS tuning properly the resonant current; (3) ZVS or ZCS if and only if I_{mv} enough negative.

Mode	$D < 0.5$		$D \geq 0.5$	
	I_{LH}	I_{HL}	I_{LH}	I_{HL}
CCM ₀	⁽¹⁾ $I_{mp} + \frac{I_1}{n}$	⁽²⁾ $I_{mv} - \frac{I_2}{n}$	⁽¹⁾ $I_{mp} + \frac{I_2}{n}$	⁽²⁾ $I_{mv} - \frac{I_1}{n}$
CCM ₁	⁽¹⁾ $I_{mp} + \frac{I_2}{n}$	⁽³⁾ $I_{mv} + \frac{I_1}{n}$	⁽²⁾ $I_{mp} - \frac{I_1}{n}$	⁽²⁾ $I_{mv} - \frac{I_2}{n}$
CCM ₂	⁽²⁾ $I_{mp} - \frac{I_1}{n}$	⁽³⁾ $I_{mv} + \frac{I_2}{n}$	⁽²⁾ $I_{mp} - \frac{I_2}{n}$	⁽³⁾ $I_{mv} + \frac{I_1}{n}$
DCM ₀	⁽¹⁾ $I_{mp} + \frac{I_1}{n}$	⁽³⁾ I_{mv}	⁽¹⁾ I_{mp}	⁽²⁾ $I_{mv} - \frac{I_1}{n}$
DCM ₁	⁽¹⁾ I_{mp}	⁽³⁾ $I_{mv} + \frac{I_1}{n}$	⁽²⁾ $I_{mp} - \frac{I_1}{n}$	⁽³⁾ I_{mv}
DCM ₂	⁽¹⁾ I_{mp}	⁽³⁾ I_{mv}	⁽¹⁾ I_{mp}	⁽³⁾ I_{mv}

satisfy the ZVS condition because I_{mp} must be positive by the converter unidirectionality, while those with (2) and (3) can satisfy ZVS or ZVC opportunely tuning the inductor current or permitting I_{mv} be negative, respectively. At a first glance of Table 4.10, CCM₀ mode is a good candidate to have ZVS (or ZCS) in the whole operating range. The ZVS condition is always satisfied in LH transition, while $I_{1,2} < nI_{mv}$ must be fulfilled. Another interesting mode is DCM₂ since the soft switching conditions are only determined by the magnetizing current without affecting the resonant tank current.

4.3.3 Simulations and Experimental Verification

In order to test and validate the theoretical analysis presented in the previous sections, simulations and measurements of a 300W prototype have been done. The power stage was assembled with the International Rectifier *IRLS4030* and *AUIRLR3110Z* indicated with $S_{a,bL}$ and $S_{a,bH}$ in Fig. 4.7 respectively. The coupled inductors were made with two RM10

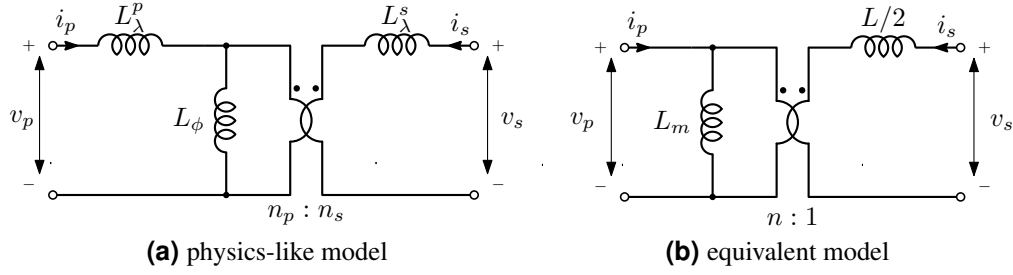


Figure 4.11: Mutual inductor models: (a) describes the magnetic coupling between two windings associating the leakage and concatenated fluxes with the corresponding inductances; (b) summaries the network behaviour highlighting a unique leakage inductance in the secondary side.

cores employing 3F3 ferrite material on which were wound 6 turns of $270 \times 71\mu\text{m}$ Litz wire (primary windings) and 24 turns of $35 \times 100\mu\text{m}$ Litz wire (secondary windings). Since each real mutual inductor presents both primary and secondary side leakage inductances, called $L_\lambda^{p/s}$, and magnetizing inductance, L_ϕ , to make it compatible with the used model of Fig. 4.7, the following transformations were used

$$L_m = L_\lambda^p + L_\phi, \quad (4.53a)$$

$$L = 2 \left[L_\lambda^s + \frac{L_\lambda^p L_\phi}{n^2(L_\lambda^p + L_\phi)} \right], \quad (4.53b)$$

$$n = \left(1 + \frac{L_\lambda^p}{L_\phi} \right) \frac{n_p}{n_s}, \quad (4.53c)$$

where L represents the total energy transfer inductance of the resonant tank. It is possible to directly measure the aforementioned quantities that permit to move from the physics-like model (Fig. 4.11a) to the used one (Fig. 4.11b), as follow:

$$L_m = \left. \frac{v_p}{i_p} \right|_{i_s=0}, \quad (4.54a)$$

$$L/2 = \left. \frac{v_s}{i_s} \right|_{v_p=0}, \quad (4.54b)$$

$$n = \frac{4L_m}{|L'_T - L''_T|} \Leftrightarrow \begin{cases} L'_T = \left. \frac{v_p + v_s}{i_p} \right|_{i_p=i_s} \\ L''_T = \left. \frac{v_p - v_s}{i_p} \right|_{i_p=-i_s} \end{cases}. \quad (4.54c)$$

Table 4.11: Prototype parameters.

Parameter	Symbol	Value	
Input Voltage	V_g	15	V
Switching frequency	f_{sw}	185	kHz
Energy transfer capacitance	C	6.8(+33)	nF
Energy transfer inductance	L	55.6	μ H
Magnetizing inductance	L_m	20	μ H
Turns ratio	n_p/n_s	6/24	
Effective turns ratio	n	0.2644	
Clamp capacitors	C_{CL}	470 + 22	nF
Output capacitors	$C_{1,2}$	470	nF

All prototype parameters are summarized in Table 4.11. A PLECS[®]/Simulink[®] model was employed to check the correspondence between the operating mode domains and their boundaries. In Fig. 4.12 is reported the outcome of this study for $F = 0.71$. The frontiers are well detected with the boundaries provided in Table 4.6-4.7 giving proof of the analysis. The prototype was used to measure the voltage gain nFM and compare it with the theoretical function (4.35) solution. In Fig. 4.13 are captured different operating points, varying duty cycle and load, for two resonance frequencies: the dots represent the prototype measurements while the dashed lines the theoretical voltage gain. At first sight, the experimental values sketch a scaled version of the respective analytic solutions. To confirm this hypothesis, the sample Pearson correlation coefficient r has been calculated for each load configuration and it appears always greater than 0.997. Since $r \simeq 1$, the real voltage gain M could be expressed by a linear function of the theoretical one M_t . It's worth noting the coefficient r value increases when it is calculated between M and ηM_t , where η is the measured efficiency, probably meaning that the linear dependence is a function of the efficiency.

4.4 Summary

In this chapter, a general approach to solve the steady-state operation of the Series-Resonant Converter class has been proposed. The analytic solution for the sampled trajectory of cur-

4.4. Summary

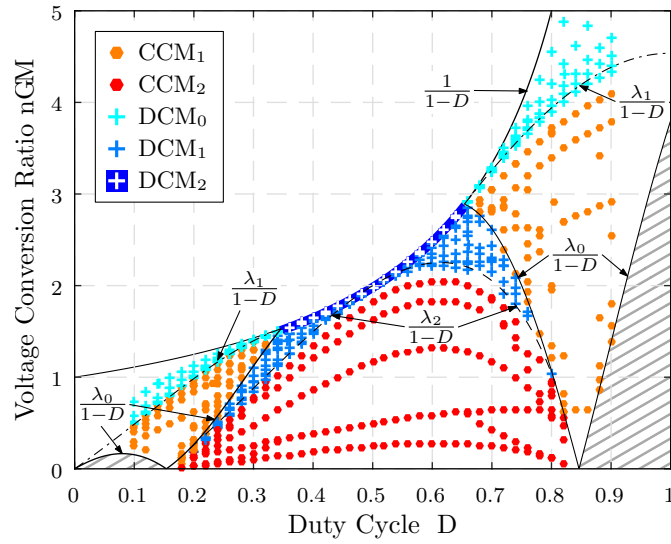


Figure 4.12: Operating points obtained via simulation for different values of duty cycle D and load R_o at $F = 0.71$. The dot colour indicates the operating mode to compare to the regions picked out with the analysis.

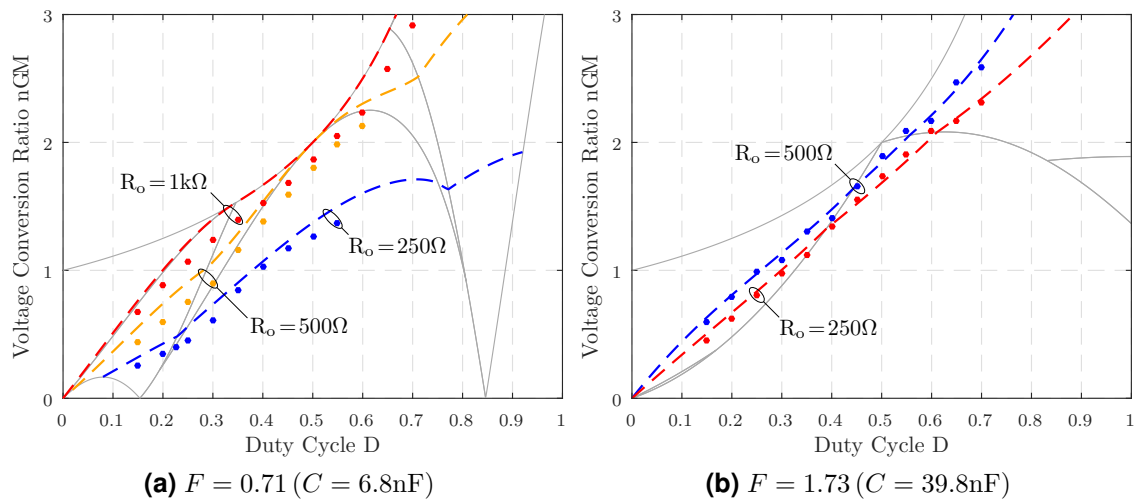


Figure 4.13: Comparison between theoretical and experimental voltage conversion ratio nFM for different values of resonant frequency: experimental measurements are indicated with dots while theoretical and voltage ratio with dashed lines.

rent and voltage in the resonant tank at the commutation instants are provided as well as the closed-form expression of the transferred power and the voltage conversion ratio. The normalized matrix representation allows a fast and flexible computation tool too. The PSM DHB converter is studied with both the proposed method and the FHA approach, to compare the error estimation of the inductor current at the switching instants and the transferred power. The theoretical framework is proved by means of simulations and experimental measurements on a 300W IBCI converter prototype. In addition to that, a comprehensive analysis of the IBCI converter is reported with a step-by-step guideline for CCM and DCM modes.

Chapter 5

Test Case

This chapter reports the Multi-Objective Optimization (MOO), described in Sec. 2.1, concerning the design of the Power Factor Correction (PFC) Boost stage in a Solid State Transformer (SST). Firstly the chosen topology is described and analysed to define the critical key points of the design procedure, e.g. modulation scheme, magnetic and switching devices, and overall system efficiency and volume. Consecutively, each single criticality is translated into a component model thus a complete converter description is obtained to implement the MOO analysis.

5.1 Multi-Cell SST

In the Distributed Energy Scenario described in Sec. 1.1, emerging Low Voltage (LV) DC applications in the medium power range ($\approx 20\text{kW}$), such as data centres and future smart buildings, among others, could benefit of a direct power electronics coupling to the Medium-Voltage (MV) AC distribution grid (2 – 35kV). The absence of intermediate energy conversion steps possibly improves the overall system efficiency and power density. Solid-State Transformer (SST) technology enables such a direct coupling of MV-AC to e.g. 400V DC grids [70]–[72].

In the recent years, several possible SST topologies have been mentioned in literature, whereby multi-stage topologies are considered most promising for the reason of flexibility and reliability. Up to now, mostly Isolated Back End (IBE) topologies have been addressed

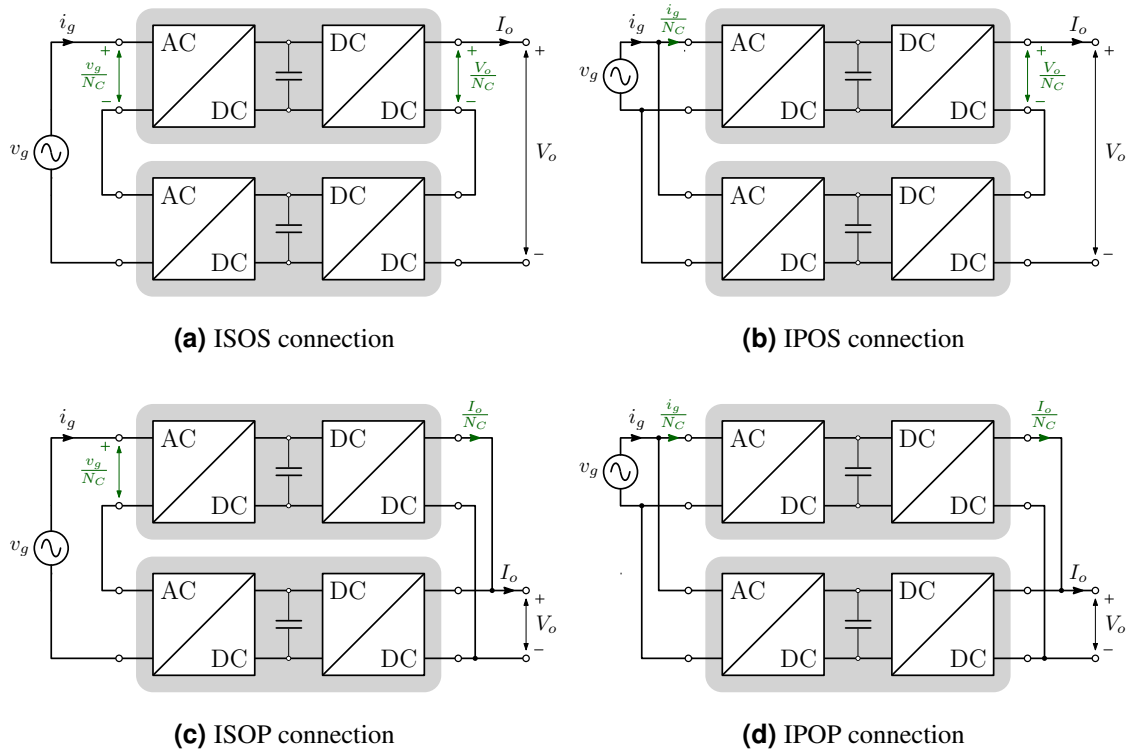


Figure 5.1: Possible Multi-cell SST configurations: (a) Input-Series Output-Series (ISOS) SST; (b) Input-Parallel Output (IPOS) SST; (c) Input-Series Output-Parallel (ISOP) SST; (d) Input-Parallel Output-Parallel (IPOP) SST

by research and industry. They are essentially composed by two cascade-connected converters: the first is an Active Rectifier Unit (ARU) which folds the AC grid voltage into $|AC|$ voltage and shapes the input current, while the second is an isolated Voltage Regulator (iVR) which provides the galvanic isolation and the output voltage regulation. In addition, several IBE converters can be arranged together to increase the quality of the electrical energy and the reliability of the overall conversion system. These topologies take the name of Multi-Cell converters and their classification regards the input and output port connection as depicted in Fig. 5.1: series connection permits to split the input/output voltage across the converter stack limiting the voltage stress of devices, while parallel connection allows to share the input/output current among the converters.

In view of the considered power and voltage rate, the Input-Series Output-Parallel (ISOP) Multi-Cell SST based on IBE cell seems the proper choice for the SST implementation. The chosen topology is shown in Fig. 5.2 where ARU stage is implemented

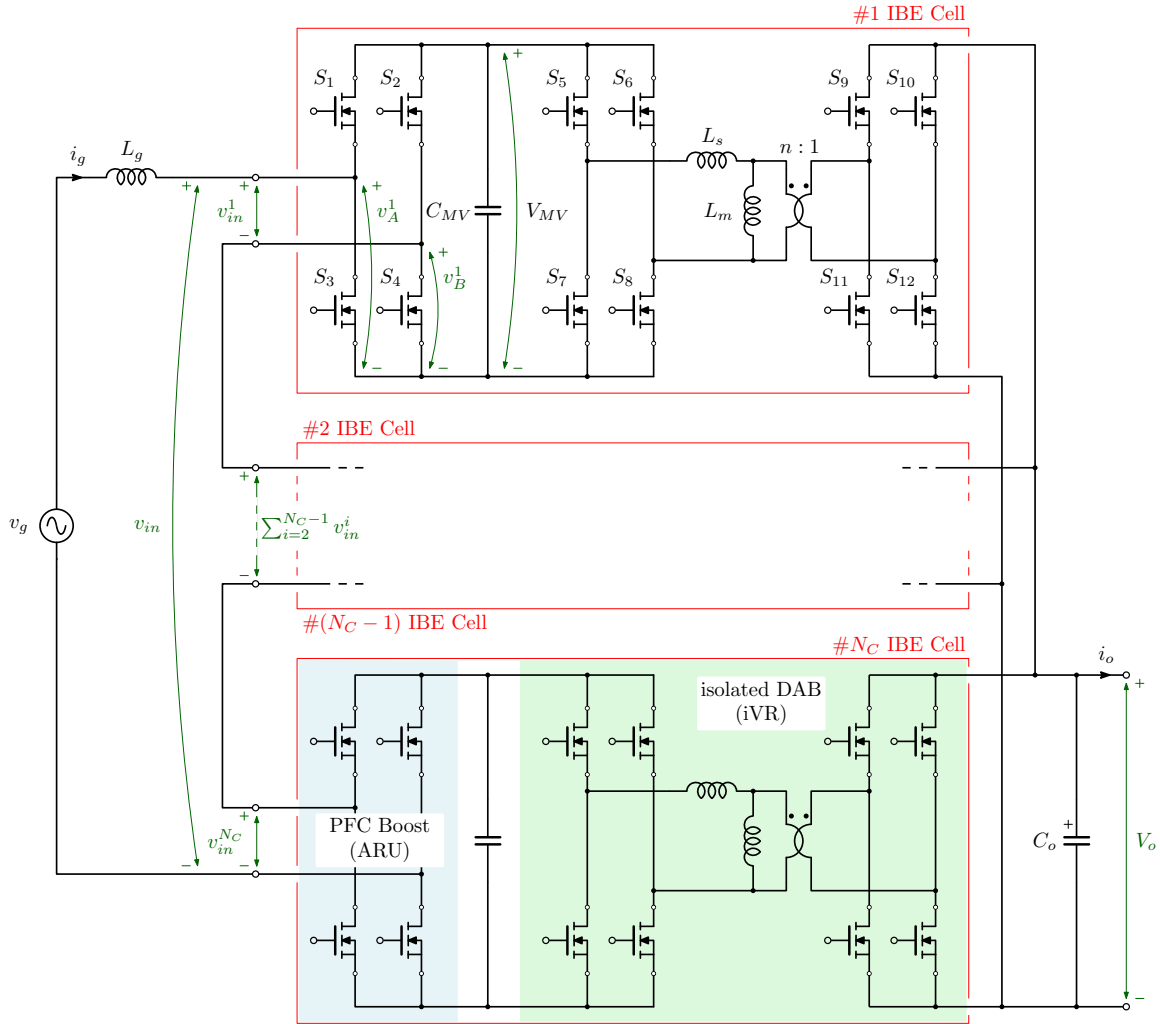


Figure 5.2: Structure of the IBE-based Multi-Cell SST: each of N_C cells is a two-stage converter composed by a PFC Boost and an isolated DAB.

with a PFC Boost, while the iVR stage is implemented using an isolated DAB converter.

The following section deals with the design of a PFC Boost through the Multi-Objective Optimization Approach. It is important to bear in mind that the aim of the proposed approach is the comparison between different solutions thus proving a direction in the final design. The specifications of the IBE-based Multi-Cell SST are reported in Table 5.1.

Table 5.1: IBE-based Multi-Cell SST specifications.

IBE-based SST	Symbol	Value	
Grid Frequency	f_g	50	Hz
AC Peak Voltage	V_g	5.4	kV
DC Output Voltage	V_o	400	V
Nominal Power	P_o	25	kW
PFC Boost stage			
Maximum Switch Voltage Stress	$V_{SW,max}$	1.3	kV
MV-DC Link Voltage Ripple	r_{MV}	± 5	%
Modulation Index	D_M	0.8	

5.2 PFC Boost Optimization

In this section the main design features of the PFC Boost are taken into account one at a time, which can essentially be summarized in the following list:

- MV-DC Link;
- Boost Inductor;
- Switching Device Losses;
- Magnetic Device Losses;
- Thermal Management.

5.2.1 MV-DC Link

The number of the SST cells, namely N_C , is defined by the maximum voltage stress $V_{SW,max}$ in the switching devices. The DC-Link voltage should be lower than the maximum drain-source voltage $V_{DS,max}$ of the considered switches to improve the system reliability. The CREE Silicon Carbide Power MOSFETs *CPM2-1700-0045B* have been chosen which $V_{DS,max} = 1.7\text{kV}$ and, considering an utilization rate around 70%, the $V_{SW,max}$ value is set to 1.3kV as reported in Table 5.1. The choice to limit the utilization rate is suggested to reduce the failures in SiC devices as reported in [73].

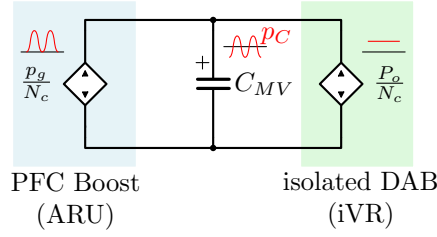


Figure 5.3: Power flow in a IBE-based SST cell.

The N_C value is also affected by the Modulation Index D_M , since it represents the ratio between the peak of the grid voltage V_g and the total SST input voltage that is equal to N_C times the DC-Link voltage. From these consideration the number of necessary cells is:

$$N_C = \left\lceil \frac{V_g}{D_M V_{SW,max}} \right\rceil = 6 \quad (5.1)$$

where $\lceil \cdot \rceil$ is the ceiling function which returns the least integer that is greater than or equal to the argument. From (5.1), the DC-Link voltage value is immediately found as:

$$V_{MV} = \frac{V_g}{D_M N_C} = 1.1\text{kV}. \quad (5.2)$$

Another main component of the DC-Link is the connected capacitor C_{MV} that has to achieve the voltage ripple constraint compensating the input power fluctuation as depicted in Fig. 5.3. The PFC Boost stage controls the input current $i_g(t)$ such that the current is in phase with the grid voltage $v_g(t)$, then the instantaneous input power $p_g(t)$ of SST is given by:

$$p_g(t) = V_g I_g \sin^2(2\pi f_g t) = \frac{V_g I_g}{2} (1 - \cos(4\pi f_g t)), \quad (5.3)$$

that is split among the N_C cells. On the other hand, each isolated voltage regulator absorbs a constant power from the DC-Link equals to P_o/N_C , therefore the instantaneous power processed by the DC-Link capacitor is:

$$p_C(t) = \frac{p_g - P_o}{N_C} = -\frac{P_o}{N_C} \cos(4\pi f_g t). \quad (5.4)$$

The energy variation in the capacitor $\Delta E_{C_{MV}}$ can be calculated from (5.4) integrating one

Individual harmonic order (odd harmonics)				
$n < 11$	$11 \leq n < 17$	$17 \leq n < 23$	$23 \leq n < 35$	$n > 35$
4.0	2.0	1.5	0.6	0.3

Table 5.2: Maximum harmonic current amplitude limit in percent of I_{load} for $I_{sc}/I_{load} < 20$ case. The even harmonics are limited of 25% of the odd harmonic limits above.

of positive (or negative) defined segments of $p_C(t)$:

$$\Delta E_{C_{MV}} = \left| \int_{-\frac{T_g}{8}}^{\frac{T_g}{8}} p_C dt \right| = \frac{P_o}{2N_C \pi f_g}. \quad (5.5)$$

The same energy variation is associated to the capacitor voltage according to the following relation:

$$\Delta E_{C_{MV}} = \frac{1}{2} C_{MV} (V_{MV,min}^2 - V_{MV,max}^2) = 2C_{MV} r_{MV} V_{MV}^2, \quad (5.6)$$

where identities $V_{MV,max} - V_{MV,min} = 2r_{MV}V_{MV}$ and $(V_{MV,max} + V_{MV,min})/2 = V_{MV}$ have been used. From (5.5) and (5.6), the value of DC-Link capacitor results:

$$C_{MV} = \frac{P_o}{4N_C \pi f_g r_{MV} V_{MV}^2}. \quad (5.7)$$

5.2.2 Boost Inductor

The Boost Inductor design is determined by the current distortion limits of grid-tie converters described in the IEEE 519-2014 standard, *IEEE Recommended Practice and Requirements for Harmonic Control in Electric Power Systems current distortion*. The Table 5.2 reports the current distortion limits for the case $I_{sc}/I_{load} < 20$, where I_{sc} is the maximum short-circuit current at PCC and I_{load} is the maximum demand load current (fundamental frequency component).

Since the constraints are on the spectral components, a closed-form expression for the input current ripple has to be found so as to easily predict its harmonic content, thus avoiding time consuming circuit simulations. To this purpose, first the modulation scheme of the overall SST is analysed to obtain the voltage across the boost inductor, then a model

regarding the associated current ripple is found.

Modulation Scheme

The modulation law of the PFC Boost stage of Fig. 5.2 is depicted in Fig.5.4 [74]. The PWM carrier signals of the leg A or B in the n -th IBE-cell, c_A^n and c_B^n , $n \in [1, N_C]$ respectively, are symmetric triangular waveforms defined in $[0, 1]$ range at f_{sw} frequency. The carriers are phase shifted among them, such that

$$\angle c_A^1 = 0, \quad \angle c_A^{n+1} = \angle c_A^n + \frac{\pi}{N_C}, \quad \angle c_B^n = \pi + \angle c_A^n.$$

The modulating signal $m_d \in [0, 1]$ is provided to all the cells. The ARU switch gate signals of each device, g_i with $i = 1, 2, 3, 4$, associated to the S_i switch in Fig. 5.2, are logically defined from these conditions:

$$g_1^n : m_d \geq c_A^n, \quad g_4^n : m_d \geq \overline{c_B^n}, \quad g_3^n = \overline{g_1^n}, \quad g_2^n = \overline{g_4^n}.$$

where the notation $\overline{y_X^n} = \text{not}(y_X^n)$.

The input voltage of each cell, i.e. $v_{in}^n = v_A^n - v_B^n$, is a three-level waveform which average value is

$$\langle v_{in}^n \rangle_{\frac{T_{sw}}{2}} = (2m_d - 1)V_{MV}, \quad (5.8)$$

where the symbol $\langle \cdot \rangle_T$ denotes the average operator, i.e. $\langle \cdot \rangle_T = \frac{1}{T} \int_0^T \cdot dt$. As highlighted in (5.8), the period of v_{in}^n is $T_{sw}/2$ because of the modulation scheme of the two legs. The effective duty cycle, i.e. the ratio between the positive or negative pulse duration and the waveform period, is given by

$$d_{in}^n = |2m_d - 1|. \quad (5.9)$$

Due to the interleaved operation, the voltage $v_{in} = \sum_{n=1}^{N_C} v_{in}^n$ is a $(2N_C + 1)$ -level waveform at frequency $f_{in} = 2N_C f_{sw}$. The average value of the ARU input voltage v_{in} in the waveform period T_{in} is

$$\langle v_{in} \rangle_{T_{in}} = (2m_d - 1)N_C V_{MV}. \quad (5.10)$$

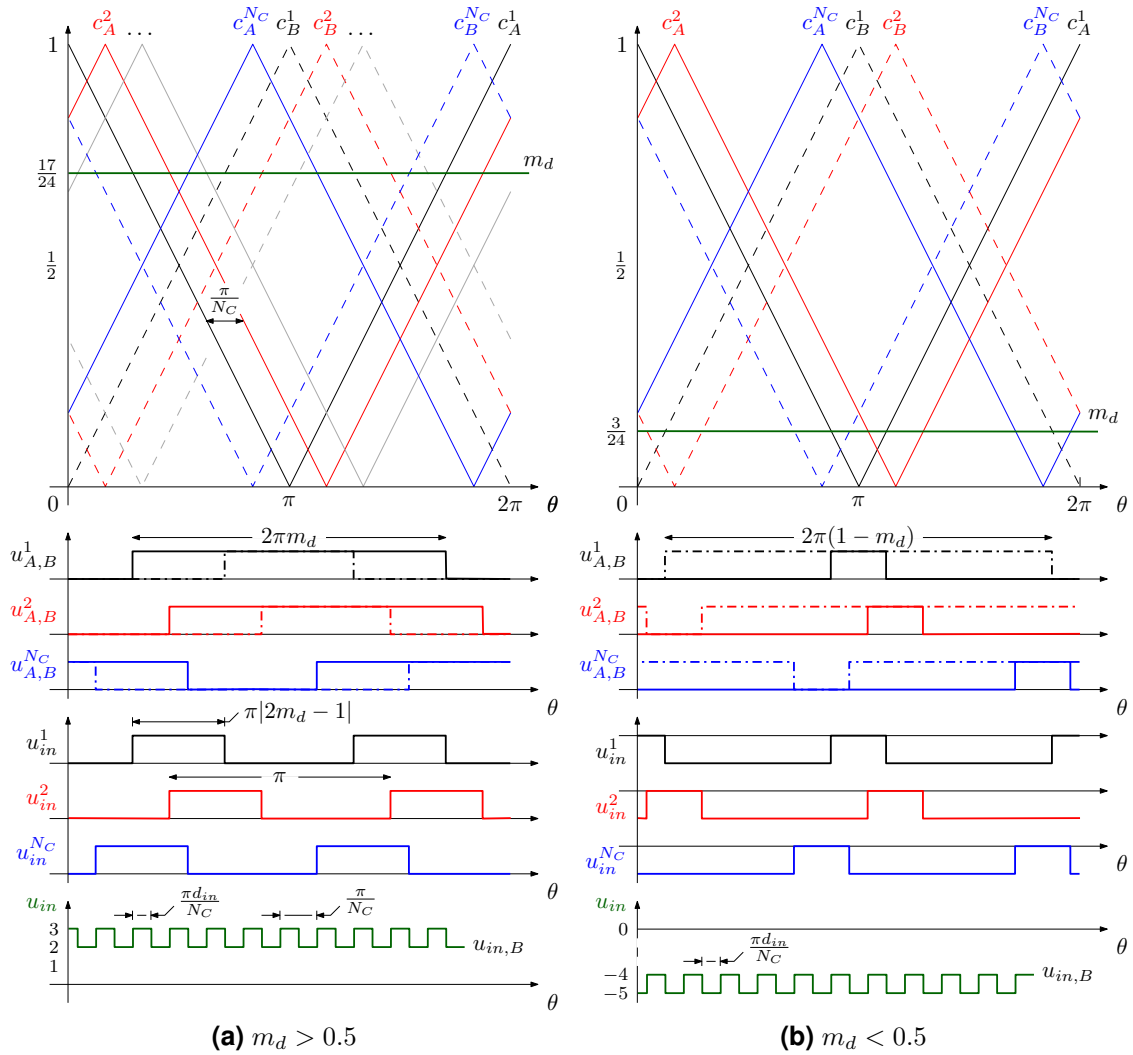


Figure 5.4: Modulation scheme of IBE-based multi-cell SST with constant switching frequency. The time axis is defined respect to the switching frequency f_{sw} , i.e. $\theta = 2\pi f_{sw}t$, while the voltage axis is normalized respect to the DC Link Voltage V_{MV} , i.e. $u = v/V_{MV}$.

It follows that, the generation of a bipolar voltage v_{ref} defined in the SST voltage range, i.e. $[-N_C V_{MV}, N_C V_{MV}]$, can be carried out providing a reference signal equal to

$$m_d = \frac{v_{ref}}{2N_C V_{MV}} + \frac{1}{2}. \quad (5.11)$$

Due to the modulation law, the generated input voltage v_{in} swings between two consecutive positive (negative) voltage levels, e.g. among kV_{MV} and $(k+1)V_{MV}$, $i \in [0, N_C - 1]$, if $v_{in} > 0$ (among $-kV_{MV}$ and $-(k+1)V_{MV}$ if $v_{in} < 0$). Then, the generated voltage v_{in} can be seen as the sum of two signals: a baseline composed by a $(2N_C - 1)$ -level staircase waveform and a three-level PWM signal that lies on the baseline. An explicative example is depicted in Fig. 5.4: in Fig. 5.4a the baseline is setted at $2V_{MV}$ and the PWM signal presents only positive pulses of amplitude V_{MV} , while in Fig. 5.4b the baseline is imposed at $-4V_{MV}$ from where the negative pulses of amplitude $-V_{MV}$ lie. To extract these signals in normalized form, the operators $(\cdot)_i$ and $(\cdot)_f$ of a real number are defined as follow

$$(x)_i = \begin{cases} \lfloor x \rfloor & x \geq 0 \\ \lceil x \rceil & x < 0 \end{cases}, \quad (5.12a)$$

$$(x)_f = x - (x)_i, \quad (5.12b)$$

where the operator $\lfloor \cdot \rfloor$ and $\lceil \cdot \rceil$ map the argument into the largest previous or the smallest following integer, respectively. Subscripts i and f have been chosen to indicate the *integer* and *fractional* part of the argument.

The duty cycle d_{in} is defined on the normalized three-level waveform $(u_{in})_f = (v_{in}/V_{MV})_f$, i.e. the fractional part of the normalized SST input voltage, and its value is given by:

$$d_{in} = |N_C(2m_d - 1)|_f. \quad (5.13)$$

The normalized voltage level $u_{in,B}$ of the baseline waveform is defined by:

$$u_{in,B} = [N_C(2m_d - 1)]_i. \quad (5.14)$$

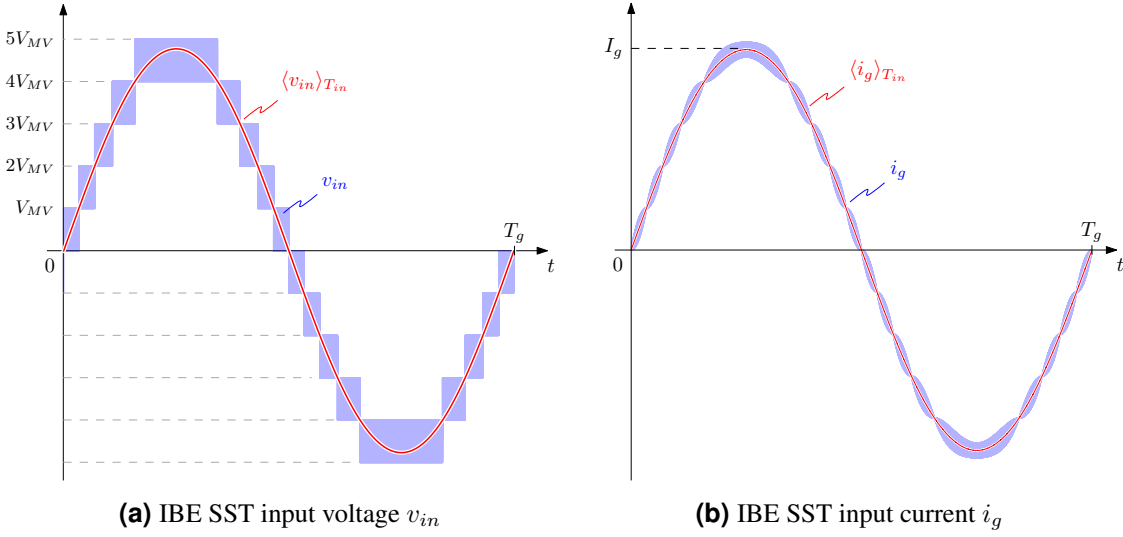


Figure 5.5: Main waveforms of IBE SST: (a) input voltage produced by the interleaved operation of 6 IBE cells; (b) input current.

The aforementioned definitions, namely (5.13) and (5.14), permit to figure out the input current spectrum and find a closed form for the boost inductance value.

High Frequency Current Spectrum

The proposed approach is aimed to separate the fundamental grid current component from its ripple and model the latter like an Amplitude Modulation, where the modulating signal is its envelope and the carrier is a symmetric triangular waveform. In Fig. 5.5 are shown the input voltage and current waveforms in the considered SST where the average value of each waveform in the T_{in} period is plotted.

Moving in the phasor domain, the grid voltage $v_g(t)$ and the input SST voltage $v_{in}(t)$, the latter as the average voltage in the effective switching period T_{in} , can be mapped in their phasor representations, \vec{v}_g and \vec{v}_{in} respectively, which definition is $v(t) = \Re \{ \vec{v} e^{j2\pi f_g t} \}$. To obtain the desired input current phasor \vec{i}_g in phase with the input grid voltage \vec{v}_g , the SST has to provide the correct input voltage \vec{v}_{in} , such that

$$\vec{v}_{in} = \vec{v}_g - j2\pi f_g L_g \vec{i}_g. \quad (5.15)$$

A phasor representation of the input SST quantities is reported in Fig. 5.6. Let us suppose

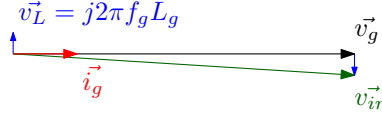


Figure 5.6: Phasor description of input SST quantities.

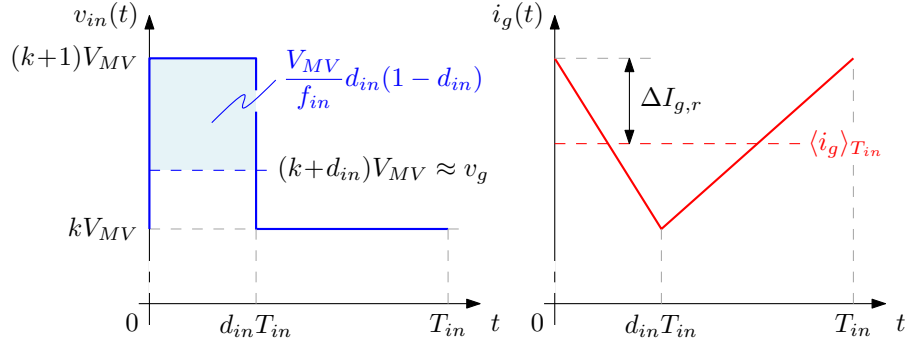


Figure 5.7: SST input voltage and current waveforms in a switching period under the hypothesis of quasi-stationary condition.

that the magnitude of the voltage phasor across the boost inductance is negligible, so \vec{v}_{in} can be approximated with \vec{v}_g allowing a further simplification, i.e. to neglect the phase shift between the two phasors.

The grid current ripple $i_{g,r}$ is defined as the difference between the grid current i_g and the fundamental harmonic component $I_{g,FH}$, i.e. $i_{g,r} = i_g - \langle i_g \rangle_{T_{in}}$. Assuming to be in a quasi-stationary condition, i.e. the converter dynamics can be neglected since the operating point changes very slowly respect the switching period, the current ripple is a function of the instantaneous duty cycle d_{in} and its amplitude is given by

$$\Delta I_{g,r} \simeq \frac{V_{MV}}{2f_{in}L_g} d_{in}(1 - d_{in}), \quad (5.16)$$

exploiting the volt-second balance on the boost inductance in the steady-state condition thanks to the aforementioned hypothesis as depicted in Fig. 5.7.

Neglecting the phase shift between \vec{v}_g and \vec{v}_{in} , the effective duty cycle d_{in} can be derived from the grid voltage as follows:

$$d_{in} = \left| \frac{v_{in}}{V_{MV}} \right|_f = \left| \frac{V_{in}}{V_{MV}} \sin(2\pi f_g t) \right|_f = |N_C D_M \sin(2\pi f_g t)|_f, \quad (5.17)$$

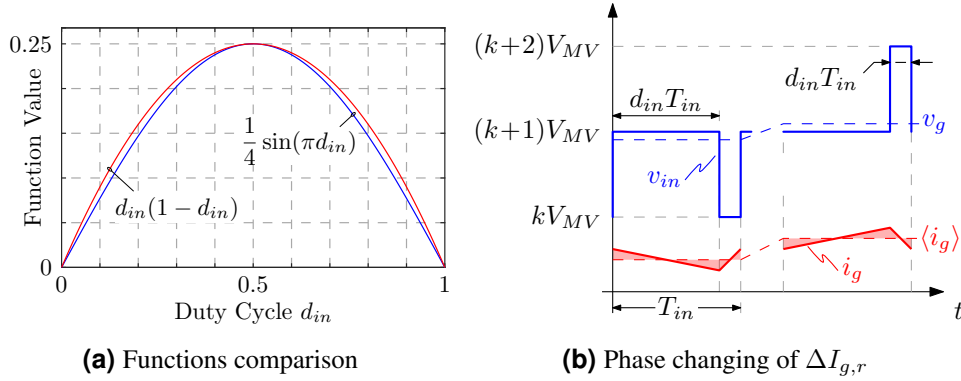


Figure 5.8: Comparison between $\Delta I_{g,r}$ and $\Delta I_{g,e}$: (a) functions $d_{in}(1-d_{in})$ and $\frac{1}{4} \sin(\pi d_{in})$; (b) phase changing of $\Delta I_{g,r}$ between two consecutive voltage levels of $v_{in,B}$.

remembering that $V_g \approx V_{in} = D_M N_C V_{MV}$ from (5.2). Combining (5.16) and (5.17), the spectrum of the ripple current $\Delta I_{g,r}$ is given by

$$\mathcal{F} \left\{ \frac{V_{MV}}{2f_{in}L_g} |N_C D_M \sin(2\pi f_g t)|_f \left(1 - |N_C D_M \sin(2\pi f_g t)|_f \right) \right\}, \quad (5.18)$$

where $\mathcal{F}(\cdot)$ indicates the Fourier Transform operator. The presence of $(\cdot)_f$ doesn't permit an easy mathematical approach to estimate the boost inductor value because it is a non linear function and cannot be computed in a closed form.

However, the term $d_{in}(1-d_{in})$ in (5.16) describes a parabola which maximum is 0.25 at $d_{in} = 0.5$ and it could be approximated by a sinusoidal function as shown in Fig. 5.8a. This approximation lets to define an estimation of the current ripple amplitude $\Delta I_{g,e}$ of $\Delta I_{g,r}$ as

$$\Delta I_{g,e} = \frac{V_{MV}}{2f_{in}L_g} \frac{\sin(\pi d_{in})}{4}. \quad (5.19)$$

Since the sine function is periodic and the objective of this analysis consists to model the envelope of $i_{g,r}$, the (5.19) is rewritten as

$$\Delta I_{g,e} = \frac{V_{MV}}{8f_{in}L_g} \sin[\pi N_C D_M \sin(2\pi f_g t)] \quad (5.20)$$

where the non linear function $(\cdot)_f$ is now deleted thanks to the periodicity of sine. Another advantage of (5.20) is that it takes also into account the phase changing of $\Delta I_{g,r}$ between

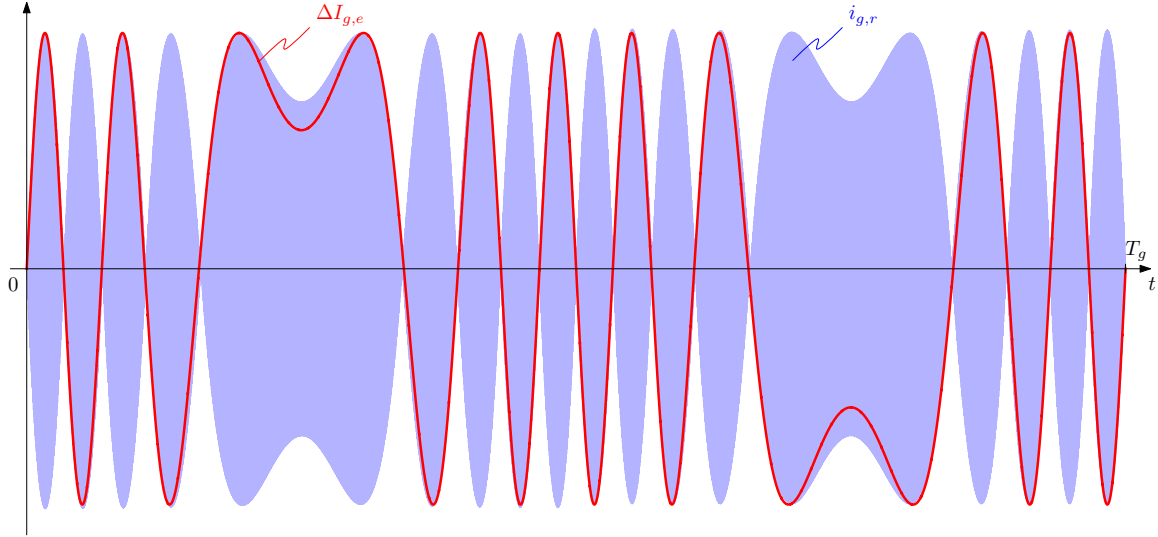


Figure 5.9: Comparison between the grid current ripple $i_{g,r}$ obtained by simulation (blue trace) and the approximated envelope (red trace).

two consecutive voltage levels as depicted in Fig. 5.8b. Lastly, the envelope of $i_{g,r}$ is depicted in Fig. 5.9 showing how it is well good modelled by (5.20). It's worth to note that (5.20) describes a frequency modulated (FM) signal, then the modulation theory allows to find the spectrum in terms of Fourier series of the given signal. The sinusoidal term can be expanded as

$$\sin(z \sin \omega_0 t) = 2 \sum_{n=0}^{+\infty} J_{2n+1}(z) \sin((2n+1)\omega_0 t), \quad (5.21)$$

and in the angular frequency domain appears like

$$\mathcal{F}_\omega \{ \sin(z \sin \omega_0 t) \} = -j \sum_{n=0}^{+\infty} J_{2n+1}(z) \left[\delta[\omega - (2n+1)\omega_0] - \delta[\omega + (2n+1)\omega_0] \right], \quad (5.22)$$

where $J_\nu(z)$ is the Bessel function of the first kind.

Substituting (5.22) in (5.20), the resulting FM signal presents only the odd components around the fundamental harmonic, i.e. the grid component f_g , and the magnitude of the $(2n+1)$ -th spectral component is

$$\left| \mathcal{F} \{ \Delta I_{g,e} \} \right|_{f=\pm(2n+1)f_g} = \frac{V_{MV}}{8f_{in}L_g} \left| J_{2n+1}(\pi N_C D_M) \right| \quad (5.23)$$

The (5.20) describes the envelope of the HF current ripple like the modulating signal in

an amplitude modulation. Approximating the current ripple waveform with a symmetric triangular wave and supposing the energy is almost entirely associated to the first harmonic of the carrier signal, the obtained spectrum is the modulating signal one shifted around carrier frequency and scaled for $\frac{8}{\pi^2}$, such that the estimated spectrum is

$$\left| \mathcal{F} \{i_{g,e}\} \right|_{f=f_{in} \pm (2n+1)f_g} = \frac{V_{MV}}{2\pi^2 N_C f_{sw} L_g} \left| J_{2n+1}(\pi N_C D_M) \right| \quad (5.24)$$

An example of this analysis is reported in Fig. 5.10 where both simulated and calculated spectrum are compared in case of $f_{sw} = 25\text{kHz}$ and $L_g = 1\text{mH}$ in the considered SST configuration, i.e. $D_M = 0.8$, $N_C = 6$. It is worthy noting that the greatest harmonic is well

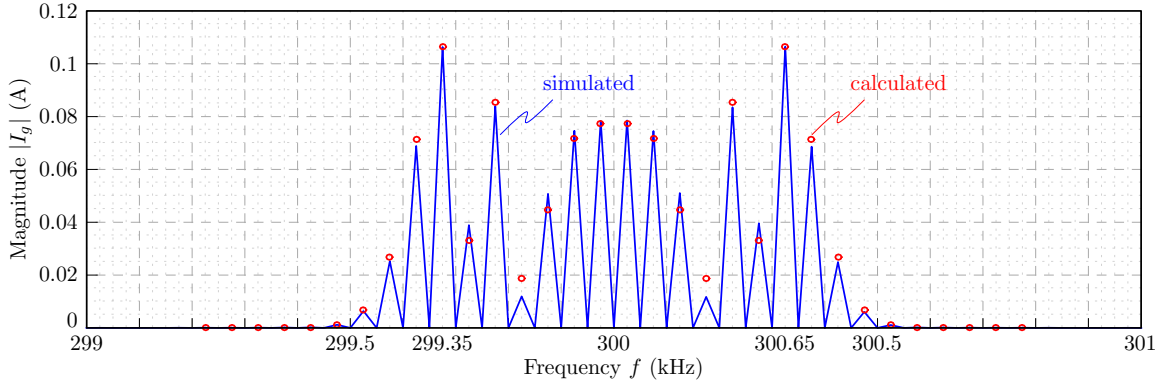


Figure 5.10: Boost Inductor Current Spectrum around frequency f_{in} obtained by simulation (blue trace) and approximated analysis using (5.24) (red circles).

estimated both in amplitude and frequency, in fact the maximum of function $J_\nu(\pi N_C D_M)$ is reached for $\nu = 13$.

If $f_{in} \gg 35f_g$, the current limit given in the standard can be considered constant and equal to αI_g , where $\alpha = 0.003$ from Tab.5.2, and a lower bound for the boost inductor can be found easily as:

$$L_g > \frac{V_{MV}}{2\pi^2 N_C f_{sw} \alpha I_g} \max_{n \geq 0} \left| J_{2n+1}(\pi N_C D_M) \right| \quad (5.25)$$

The Figure 5.11 shows the value obtained via (5.25) and the first value of inductance that satisfies the constraint via simulation making visible the correctness of the estimation.

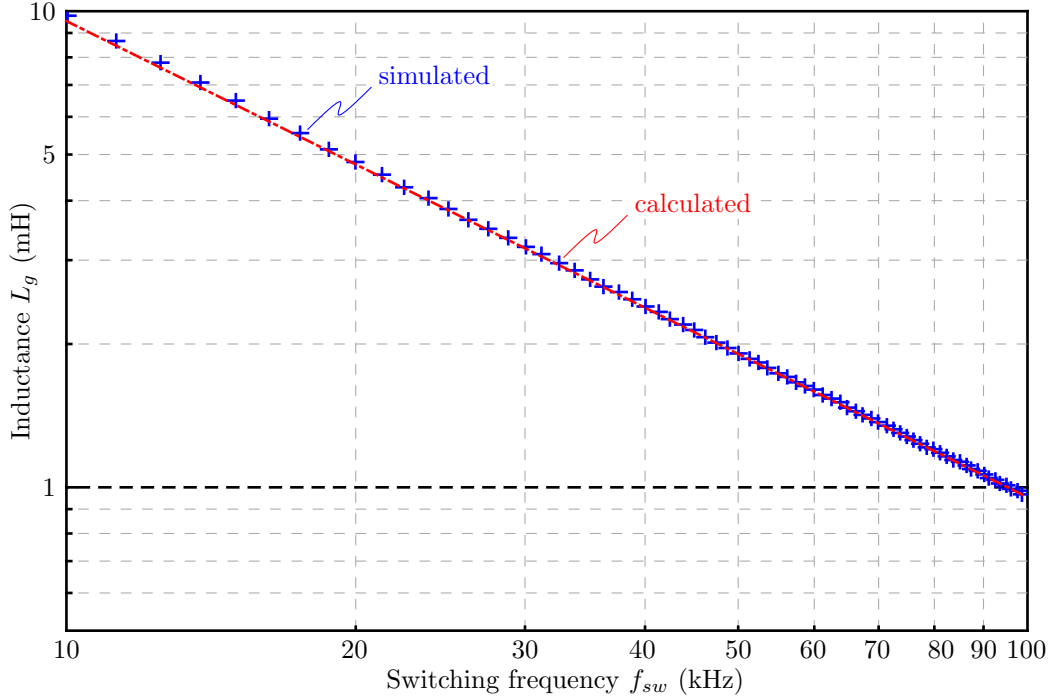


Figure 5.11: Comparison between the Boost Inductor Value obtained by simulation (blue crosses) and approximated analysis using (5.25) (red trace) to achieve the IEEE standard.

5.2.3 Switching Device Losses

The PFC Boost stage intrinsically suffers of Hard Switching (HS) commutations: the commutated current is the fundamental grid current i_g basically, because the superimposed ripple is negligible. For example, the LH transition of the switching node A occurs in ZVS condition when the input current is positive, as well as the HL transition of node B. On the other hand, vice versa occurs when the i_g is negative. These intrinsic losses reduce the possible switching frequency range due to the thermal limits of the switches.

To reduce the switching losses, the proposed solution is adding between the nodes A and B a series resonant tank, the inductance L and capacitance C as showed in Fig. 5.12, afterwards indicated with internal Triangular Current Modulation (iTCM). The aim of the resonant tank is to add a circulating current in the switches, achieving the condition of complete or partial Zero Voltage Switching (ZVS or pZVS) almost everywhere in the grid period. The kind of transition, hard or soft, depends on the difference between the grid current i_g and the resonant current i_L .

The amplitude of i_L is dependent on the duty cycle d_{in}^n of the IBE-cell input voltage

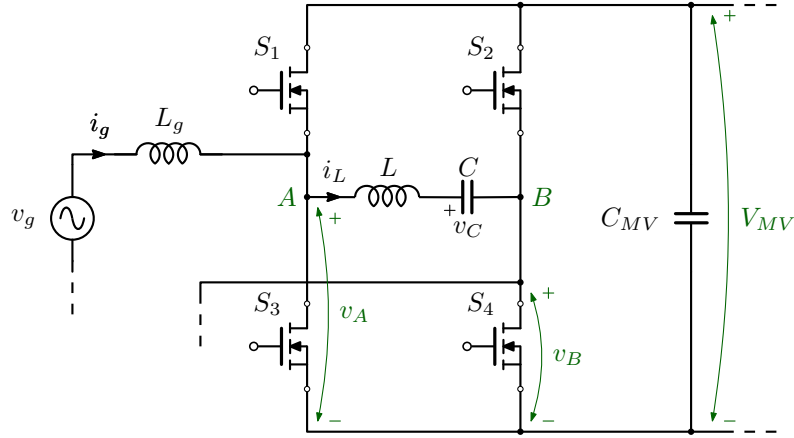


Figure 5.12: Proposed scheme for the reduction of the switching losses (iTCM).

v_{in}^n , so it is independent on the grid current amplitude. However, v_{in} and i_g are related to the apparent power on SST input port which establishes the phase shift between them. The additional current modifies the values of the switching node current at the commutation instant, even changing its sign. The main voltage and current waveforms that are involved are shown in Fig. 5.13 where the ZVS or HS conditions are highlighted in case the resonant current permits them.

This reactive current decreases the switching losses on the one hand, and increases the conduction losses in the switch on the other since the RMS current is increased. The resonant inductor and capacitor are also a source of losses that have to be included. It's easy to imagine that a trade-off between switching and conduction losses exists, both in the switches and in the resonant tank, opening for the possibility to find the minimum of the overall losses. However, soft switching is always equivalent to low EMI emissions that is an important feature [75]–[76].

ZVS Impedance

The proposed framework for the steady-state analysis of the Series Resonant converter can be exploited to study the inductor current and capacitor voltage evolution in the resonant tank. From this information the overall losses in the switches are obtained, while for the tank a magnetic model for the inductor is necessary.

Since the frequency of $v_{in}^n = v_A^n - v_B^n$ is double respect to f_{sw} due to the interleaved

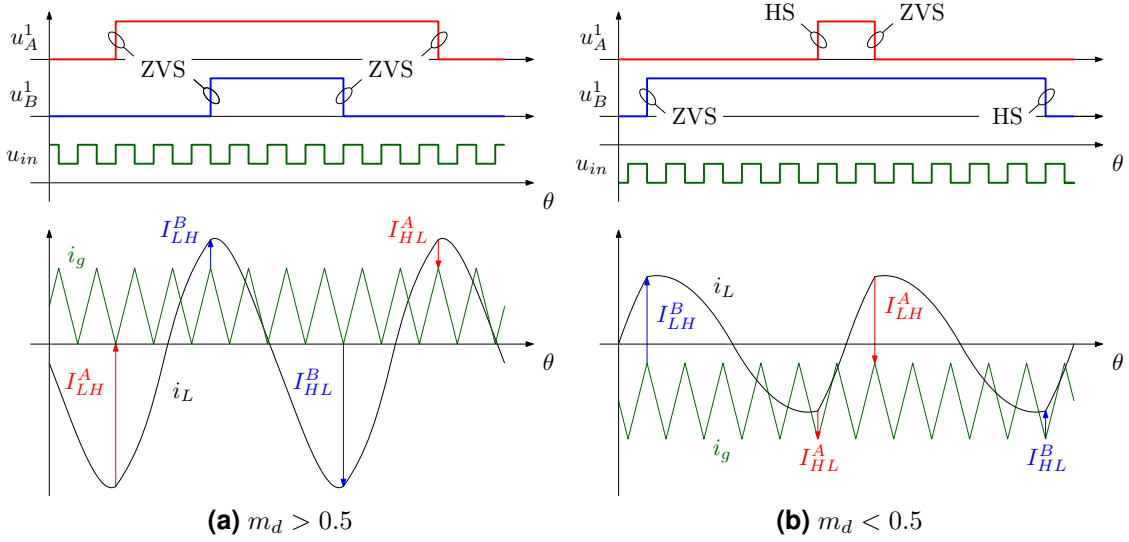


Figure 5.13: Main waveforms of iTCM: the vectors between the currents i_g and i_L indicates the magnitude and the sign of the transition current.

Table 5.3: Definition of $U_{Z,i}$ and δ_i and δ_i for ZVS impedance.

i	$U_{Z,i}$	δ_i
1	1	$2\pi d$
2	0	$2\pi(1-d)$

operation, the normalized frequency F is defined in this case as $F = 2f_{sw}/f_r$. The i -th value of the impressed voltage is expressed by the single variable $U_{Z,i} = q_{A,i} - q_{B,i}$ since in this case the two voltages V_g and V_o are equal to V_{MV} entailing $U_g = 1$. The intervals duration and their related inputs in this configurations are only two as reported in the Table 5.3. The normalized waveform of the state variables ($j_L u_C$) are reported in In Fig. 5.14. To simplify the notation, in the following analysis the value of the duty cycle d_{in}^n is just indicated with d .

Applying (4.3) and (4.7), the values of normalized inductor current and capacitor volt-

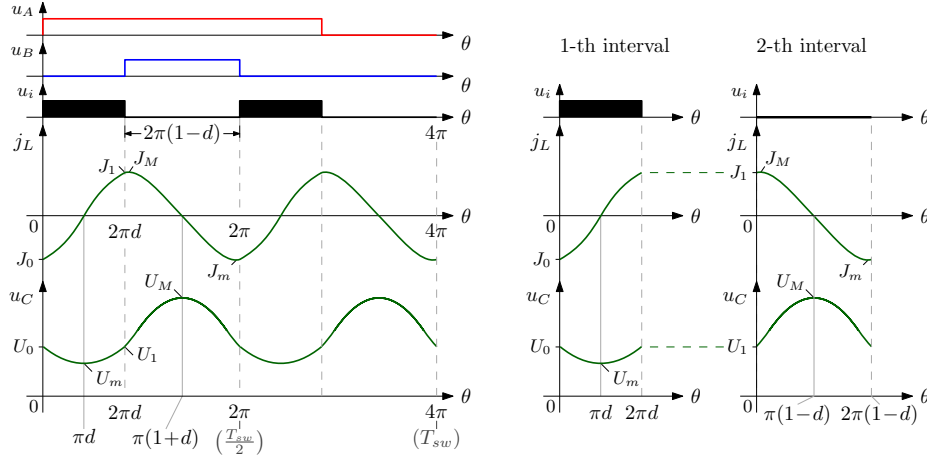


Figure 5.14: Normalized current and voltage waveforms in the resonant tank in the switching period and in each subinterval used in the analysis. The time axis is normalized to double switching frequency, i.e. $\theta = 4\pi f_{sw}t$.

age are derived:

$$J_0 = -\frac{\sin \frac{\pi d}{F} \sin \frac{\pi(1-d)}{F}}{\sin \frac{\pi}{F}} \quad J_1 = -J_0 \quad (5.26a)$$

$$U_0 = \frac{\sin \frac{\pi d}{F} \cos \frac{\pi(1-d)}{F}}{\sin \frac{\pi}{F}} \quad U_1 = U_0 \quad (5.26b)$$

To achieve complete or partial Zero Voltage Switching, indicated with ZVS or pZVS, a necessary condition is $J_0 < 0$ and $J_1 > 0$ otherwise the additional current provided by the resonant tank can only increase the hard switching losses. Since $J_0 = -J_1$, it's sufficient to study only one condition. Studying the sign of J_0 in the (d, F) -plane, the normalized frequency F could be chosen greater than 1 such that in the whole grid period the condition will be satisfied as shown in the Fig. 5.15. The magnitude of $I_0 = J_0 I_N$ defines which kind of commutation occurs.

In the first angle interval, i.e. $[0, 2\pi d]$, the normalized current evolution j_L is expressed by

$$j_L = J_0 \cos \frac{\delta}{F} - (U_0 - 1) \sin \frac{\delta}{F}, \quad (5.27)$$

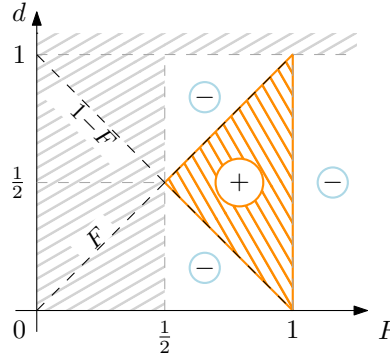


Figure 5.15: Sign of the normalized current J_0 . Gray regions are not considered in the analysis.

and maximum or minimum points satisfy

$$\frac{\partial j_L}{\partial \delta} = -\frac{1}{F} \left[J_0 \sin \frac{\delta}{F} + (U_0 - 1) \cos \frac{\delta}{F} \right] = 0. \quad (5.28)$$

Substituting (5.26) in (5.28), the solutions are

$$\delta_{M,m} = \pi \left(d \pm \frac{F}{2} \right) \wedge d > \frac{F}{2} \quad (5.29)$$

thus the stationary points exist only in a region of the (d, F) -plane otherwise the function is monotonic and the local maximum and minimum correspond to the function values at the interval extremes. The local maximum and minimum are given by

$$J'_{M,m} = \pm \frac{\sin \frac{\pi(1-d)}{F}}{\sin \frac{\pi}{F}} \quad (5.30)$$

In the second angle interval, i.e. $[0, 2\pi(1-d)]$, the normalized current evolution j_L is expressed by:

$$j_L = J_1 \cos \frac{\delta}{F} - U_1 \sin \frac{\delta}{F} \quad (5.31)$$

It's worth to note that in this case the origin is moved at the beginning of the second interval, as showed in Figure 5.14. The local maximum or minimum points in the second

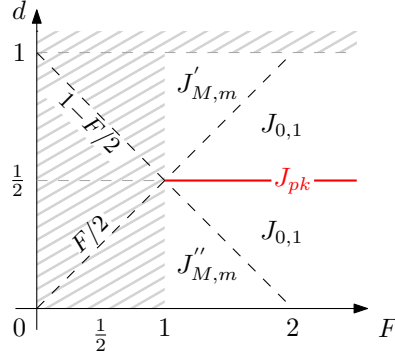


Figure 5.16: Local stationary points in the (d, F) -plane. Gray regions are not considered in the analysis.

subinterval, i.e. $[0, 2\pi(1 - d)]$, are allocated in:

$$\delta_{M,m} = \frac{\pi}{F} \left(1 - d \pm \frac{F}{2} \right) \wedge d < 1 - \frac{F}{2} \quad (5.32)$$

that means in the half switching period they are located in $\delta_{M,m} = \frac{\pi}{F} \left(1 + d \pm \frac{F}{2} \right)$ due to the $2\pi d$ angle adding. The local maximum and minimum values are given by

$$J''_{M,m} = \pm \frac{\sin \frac{\pi d}{F}}{\sin \frac{F}{\pi}} \quad (5.33)$$

Since the two (d, F) -plane regions don't overlap in the remaining part of the plane and the current function is monotonic, $J_{0,1}$ are the local stationary points. In Fig. 5.16 the maximum and minimum values of the normalized current in a switching period are depicted. They identify three different regions in the (F, d) -plane where equations (5.26), (5.30) and (5.33) allow to calculate the local stationary points of the current for different values of the duty cycle d and normalized frequency F . To find the peak current in the whole grid

period, the derivative respect to the duty-cycle has to be taken into account:

$$\frac{\partial J'_M}{\partial d} = -\frac{\pi \cos \frac{\pi(1-d)}{F}}{\sin \frac{\pi}{F}} < 0 \quad \forall d : d > \frac{F}{2} \quad (5.34a)$$

$$\frac{\partial J''_M}{\partial d} = \frac{\pi \cos \frac{\pi d}{F}}{\sin \frac{\pi}{F}} > 0 \quad \forall d : d < 1 - \frac{F}{2} \quad (5.34b)$$

$$\frac{\partial J_1}{\partial d} = \frac{\pi \sin \frac{\pi(1-2d)}{F}}{\sin \frac{\pi}{F}} = 0 \quad \text{if } d = \frac{1}{2} \quad (5.34c)$$

The maximum value of J'_M and J''_M is reached at the region border, i.e. $d = \frac{F}{2}$ and $d = 1 - \frac{F}{2}$ respectively, and their value is:

$$\widehat{J}'_M = \widehat{J}''_M = -\cot \frac{\pi}{F} \quad (5.35)$$

while the maximum value of J_1 is

$$\widehat{J}_M = \frac{1}{2} \tan \frac{\pi}{2F} \quad (5.36)$$

Comparing (5.35) and (5.36), \widehat{J}_M is always greater than \widehat{J}'_M and \widehat{J}''_M , then the peak value J_{pk} of j_L during the whole grid period is given by

$$J_{pk} = \frac{1}{2} \tan \frac{\pi}{2F}. \quad (5.37)$$

Regarding the resonant capacitor, the maximum or minimum voltage is reached when the current j_L is zero. Imposing (5.27) equals to zero in the first angular interval, i.e. $[0, 2\pi d]$, the normalized current j_L is zero at the middle of the interval, $\delta = \pi d$. Also in the second one, i.e. $[0, 2\pi(1-d)]$, j_L reaches zero value in the middle, $\delta = \pi(1-d)$.

In the first interval, the normalized voltage evolution is given by

$$u_C = J_0 \sin \frac{\delta}{F} + (U_0 - 1) \cos \frac{\delta}{F} + 1, \quad (5.38)$$

and the local stationary point is in the centre of the interval. Since u_C is a continuous function and the derivative respect to δ is proportional to the current j_L , to understand if it's a minimum or a maximum point is sufficient studying the sign of the current. The current starts from a negative value (J_0) to a positive one (J_1), so it describes a minimum point which value is:

$$U'_m = 1 - \cos \frac{\pi d}{F} + \cot \frac{\pi}{F} \sin \frac{\pi d}{F}.$$

In the second interval, the normalized voltage trajectory is expressed by

$$u_C = J_1 \sin \frac{\delta}{F} + U_1 \cos \frac{\delta}{F} \quad (5.39)$$

and, as before, the local stationary point is in the centre of the interval. Using the before-mentioned considerations, the current starts from a positive value (J_1) to a negative one (J_0) in this interval, so it describes a maximum point which value is:

$$U'_M = \cos \frac{\pi(1-d)}{F} - \cot \frac{\pi}{F} \sin \frac{\pi(1-d)}{F}$$

To find the peak values in the whole grid period, the directional derivative along the duty-cycle direction has to be taken into account.

$$\frac{\partial U'_m}{\partial d} = \frac{\pi}{F} \left[\sin \frac{\pi d}{F} + \cot \frac{\pi}{F} \cos \frac{\pi d}{F} \right] \geq 0 \quad \forall d : d \geq 1 - \frac{F}{2} \quad (5.40a)$$

$$\frac{\partial U'_M}{\partial d} = \frac{\pi}{F} \left[\sin \frac{\pi(1-d)}{F} + \cot \frac{\pi}{F} \cos \frac{\pi(1-d)}{F} \right] \geq 0 \quad \forall d : d \leq \frac{F}{2} \quad (5.40b)$$

The minimum and maximum normalized capacitor voltages in the grid period are reached when $d = 1 - \frac{F}{2}$ and $d = \frac{F}{2}$, respectively. In case the duty-cycle is upper bounded at D_M , the maximum voltage is also clamped to $U'_M(D_M)$ value, such that:

$$U_m = 1 - \csc \frac{\pi}{F} \quad U_M = \begin{cases} \csc \frac{\pi}{F} & \text{if } F \leq 2D_M \\ U'_M(D_M) & \text{if } F > 2D_M \end{cases} \quad (5.41)$$

where $\csc(\cdot)$ is the cosecant function: $\csc \theta = (\sin \theta)^{-1}$. Since $U_M > |U_m|$, the peak value

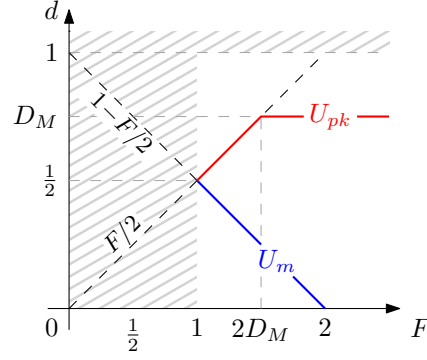


Figure 5.17: Local stationary points in the (D, F) -plane. Gray regions are not considered in the analysis.

U_{pk} of u_C during the whole grid period is given by

$$U_{pk} = \begin{cases} \csc \frac{\pi}{F} & \text{if } F \leq 2D_M \\ U'_M(D_M) & \text{if } F > 2D_M \end{cases} \quad (5.42)$$

In Fig. 5.17 are summarized the location of maximum and minimum points in (d, F) -plane.

The equations (5.37) and (5.42) provide important information about the maximum current and voltage stress in the resonant tank that are useful in the next design steps: the peak current I_{pk} establishes the geometry of inductor because it is related to the maximum stored energy, and also the interval of the grid period where ZVS occur. Instead, the peak voltage V_{pk} provides information about the volume of the capacitor since it is also related to the maximum stored energy. To complete the analysis regarding the resonant tank only the conduction losses have to be taken into account and they are related to the RMS value of both inductor current and capacitor voltage.

The inductor RMS current value is obtained as

$$\begin{aligned} I_{L,RMS} &= \sqrt{\frac{1}{T_g} \int_0^{T_g} i_L^2(t) dt} = \sqrt{f_g \sum_{n=1}^{\frac{2f_{sw}}{f_g}} \int_{(n-1)\frac{T_{sw}}{2}}^{n\frac{T_{sw}}{2}} i_{L,n}^2 dt} \\ &= I_N \sqrt{f_g \sum_{n=1}^{\frac{2f_{sw}}{f_g}} \int_{(n-1)\frac{T_{sw}}{2}}^{n\frac{T_{sw}}{2}} j_{L,n}^2(t) dt} = I_N \sqrt{\frac{f_g}{4\pi f_{sw}} \sum_{n=1}^{\frac{2f_{sw}}{f_g}} \int_0^{2\pi} j_{L,n}^2(\delta) d\delta}, \end{aligned} \quad (5.43)$$

where $i_{L,n}$ represents the inductor current $i_L(t)$ in the n -th resonant cycle, with $n \in [1, \frac{2f_{sw}}{f_g}]$. For each value of the modulation sequence d_m , $m \in [1, \frac{f_{sw}}{f_g}]$, the resonant current performs the same trajectory two times in a switching period, due to the used modulation law.

This permits to simplify the integral as

$$I_{L,RMS} = I_N \sqrt{\frac{f_g}{2\pi f_{sw}} \sum_{d_m} \int_0^{2\pi} j_L^2(\delta, d_m) d\delta}. \quad (5.44)$$

Defining the integral value $K_J(m)$ as a function of the duty cycle d_m in the m -th interval:

$$\begin{aligned} K_J(m) &= \int_0^{2\pi} j_L^2(\delta, d_m) d\delta \\ &= \frac{1}{\sin^2 \frac{\pi}{F}} \left[\pi(1-d_m) \sin^2 \frac{\pi d_m}{F} + \pi d_m \sin^2 \frac{\pi(1-d_m)}{F} \right. \\ &\quad \left. - F \sin \frac{\pi}{F} \sin \frac{\pi d_m}{F} \sin \frac{\pi(1-d_m)}{F} \right], \end{aligned} \quad (5.45)$$

the RMS value of the inductor current is given by

$$I_{L,RMS} = I_N \sqrt{\frac{f_g}{2\pi f_{sw}} \sum_{d_m} K_J(m)}. \quad (5.46)$$

In the same way done for the inductor current, the capacitance RMS voltage value is obtained as

$$V_{C,RMS} = \sqrt{\frac{1}{T_g} \int_0^{T_g} v_C^2(t) dt} = V_N \sqrt{\frac{f_g}{2\pi f_{sw}} \sum_{d_m} \int_0^{2\pi} u_C^2(\delta, d_m) d\delta} \quad (5.47)$$

where $u_C(\delta, d_m)$ represents the normalized capacitor voltage $u_C(t)$ in the m -th switching period with $d = d_m$. The integral value $K_U(m)$ is a function of the duty cycle d_m in the

m -th interval:

$$\begin{aligned}
K_U(m) &= \int_0^{2\pi} u_C^2(\delta, d_m) d\delta \\
&= \frac{1}{\sin^2 \frac{\pi}{F}} \left[\pi(1 - d_m) \sin^2 \frac{\pi d_m}{F} + \pi d_m \sin^2 \frac{\pi(1 - d_m)}{F} \right. \\
&\quad \left. + 2\pi d_m \sin^2 \frac{\pi}{F} - 3F \sin \frac{\pi}{F} \sin \frac{\pi d_m}{F} \sin \frac{\pi(1 - d_m)}{F} \right], \tag{5.48}
\end{aligned}$$

and the value of the RMS voltage is:

$$V_{C,RMS} = V_N \sqrt{\frac{f_g}{2\pi f_{sw}} \sum_{d_m} K_U(m)}. \tag{5.49}$$

Knowing the expression of the resonant peak current and its RMS value, a first investigation can be made considering the conduction and switching losses, P_j and P_{sw} respectively, at nominal power in a grid period for different values of switching frequency f_{sw} , resonant peak current I_{pk} and normalized frequency F (or corresponding resonant frequency f_r). These three parameters represent the Design Space (DS) where the Multi-Objective Optimization is applied to find which is the set of the optimum designs. In Fig. 5.18 the results of this first analysis are showed considering the performance of a single cell: increasing the switching frequency, the switching losses increase as shown in Fig. 5.18a, instead the conduction losses increase with the peak current, as depicted in Fig. 5.18b. The Fig. 5.18c describes how for each couple of f_{sw} and I_{pk} , both conduction and switching losses reduce increasing the normalized frequency F since the points move towards the origin.

5.2.4 Magnetic Device Losses

As aforementioned in Sec. 5.2.2 and 5.2.3, a model for magnetic components is needed to have an estimation of their losses and volume. It is also necessary to keep in mind that the aim of the modelling is to take into account the majority of the loss processes and to provide the model in a reasonable time. For this reasons, both resonant and boost inductor are modelled as shown in Fig. 5.19. It is an E-core inductor where the winding is split around

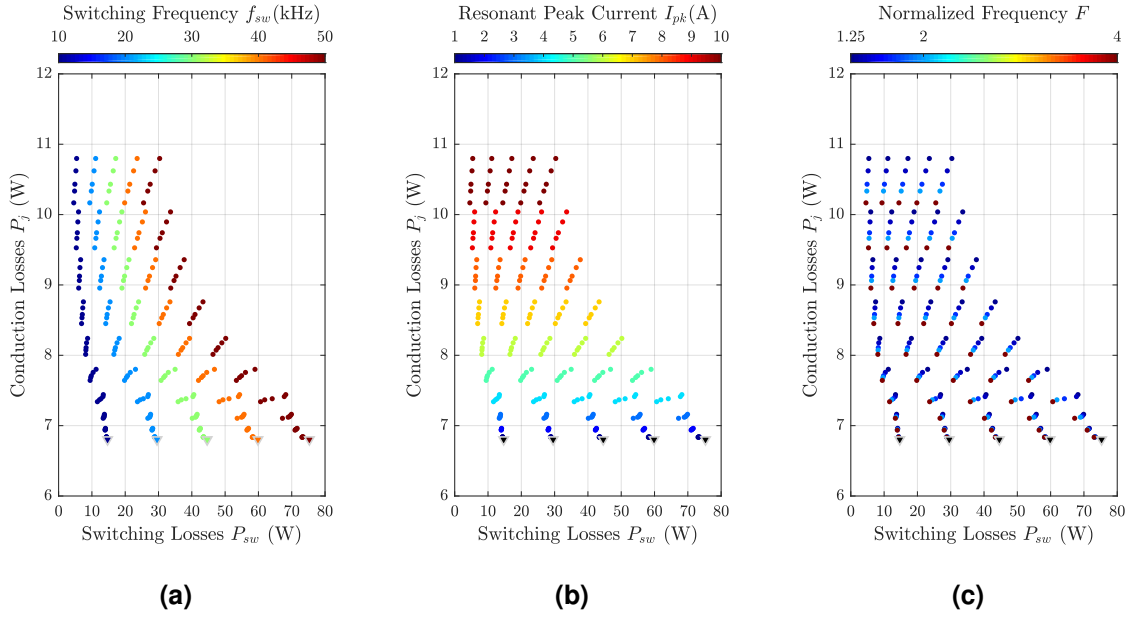


Figure 5.18: Conduction and switching losses in the considered design space (f_{sw} , I_{pk} , F) of a single IBE cell. The ∇ indicates the designs where the iTCM is not implemented.

the air-gap to reduce the fringing effects. The choice of E-core is suggested by the wide range of LF and HF core materials, core shapes and possible assembly configurations, that permit to consider their discrete DS as continuous. As the MOO approach has been used for the whole SST system, MOO is applied on the magnetic devices to return the proper set of inductor designs that have the best performances in term of losses and volume. In Figure 5.20 the geometry of the inductor model is described where are indicated the quantities determined in the optimization process. The two inductors work at different frequency range since the Boost inductor is stressed by the LF grid current while the ZVS inductor is crossed by HF resonant current, that permits to choose different core materials and wires for each inductor to make the most of his frequency separation. For the boost inductor the *Si-Steel 2605SA1 (Metglas)* core material is considered and the winding is made with simple stranded wire since the skin effect is negligible at grid frequency, instead for the ZVS inductor the core is *Si-Ferrite N87 (EPCOS)* with Litz wires are required because of HF operation.

From these previous considerations, the Design Space of the inductors sweeps the following parameters:

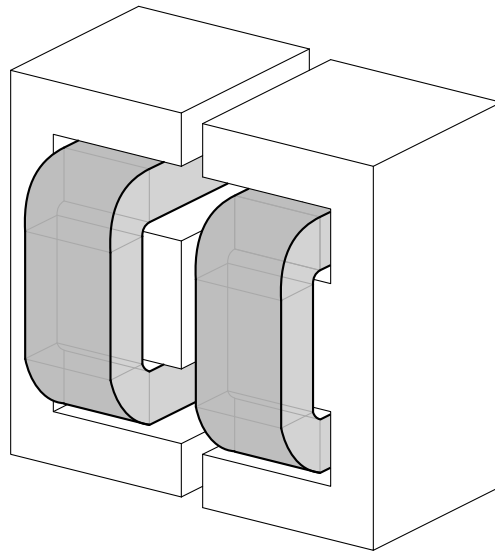


Figure 5.19: Base inductor model.

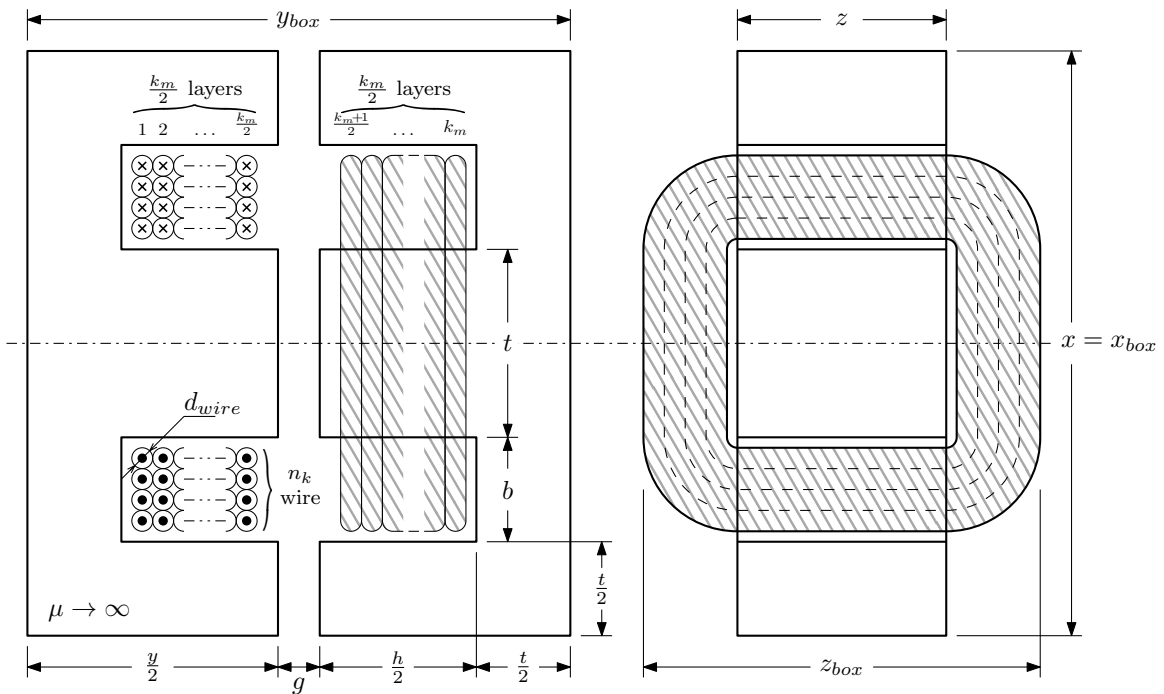


Figure 5.20: Geometry of the base inductor model: the indicated quantities are functions of the chosen point in the Design Space.

- *maximum flux density* B_{max} (T) that must be lower than the saturation flux density B_{sat} of the selected core material;
- *total winding turns* N that are split in k_m layers of n_k wires;
- *current density* J (A/m²) of each wire;
- *winding windows shape factor* k_{hb} defined as the ratio between the height h and the width b of the winding window;
- *core cross section shape factor* k_{zt} defined as the ratio between the depth z and the width t of the core cross section;
- *strand Litz wire diameter* d_{str} (m) only for the ZVS inductor.

To design the inductors the procedure reported in [77] has been the reference. In the following step the main approximations are explained to provide a guideline of the design procedure.

The dimension of the core cross section are implicitly defined in the DS knowing which is the peak current: for the boost inductor it is represented by the nominal current I_g , while for the ZVS inductor it is a parameter of the SST DS, i.e. (f_{sw}, I_{pk}, F) . The needed core cross section A_e is

$$A_e = \frac{LI_{pk}}{NB_{max}}, \quad (5.50)$$

and from the parameter k_{zt} the dimension of the E core branches are found:

$$z = \sqrt{k_{zt}A_e} \quad t = k_{zt}^{-1}z. \quad (5.51)$$

Instead, the total window area is defined by the RMS values of the current flowing in the winding: as done for the approximation of the peak current value, its RMS value is given by $I_g/\sqrt{2}$, while for the ZVS inductor it is calculated with (5.46) for each point in the SST DS. The windows section A_w is so defined

$$A_w = \frac{NI_{rms}}{k_w k_{Aw} J}, \quad (5.52)$$

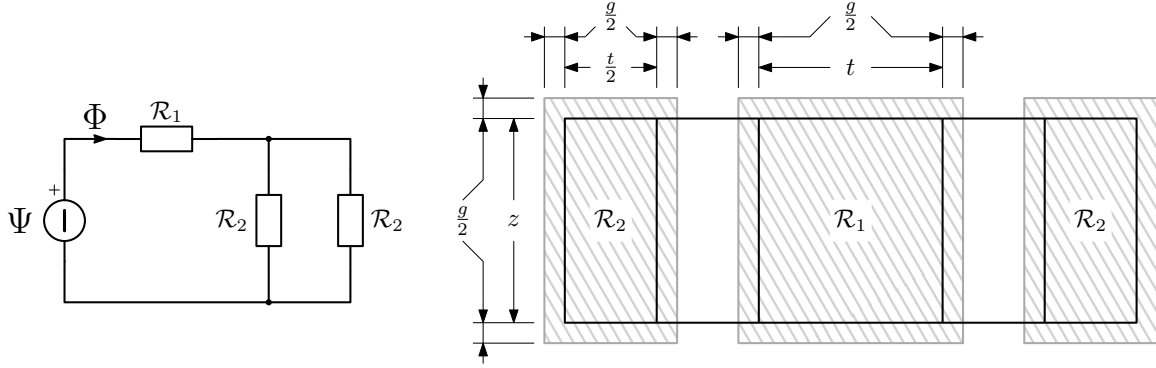


Figure 5.21: Magnetic core paths in a E core.

where k_w and k_{Aw} are the wire and window fill factor respectively. These parameters take into account the effective copper area, the first in the single wire and the second in the whole window. From the parameter k_{hb} the dimension of the window is calculated as:

$$h = \sqrt{k_{hb} A_w} \quad b = k_{hb}^{-1} z. \quad (5.53)$$

The effective copper section provides also information about the number of strands in the Litz wire or the diameter of the stranded wire, as well as the number of layer k_m and the turns for layer n_k .

To set the correct value of inductance, the air-gap g must be calculated. In fact it changes the reluctance values of the three magnetic paths of E-core. The magnetomotive force (MMF) produced by the central branch winding Ψ feeds the magnetic flux Φ along the different reluctances of the core. Considering the core magnetic permeability greater than the air one, i.e. $\mu \gg \mu_0$, the reluctance of each branch is only given by the air-gap reluctance. In Fig. 5.21 the magnetic circuit is depicted, showing also the considered cross section of the air-gap that takes into account the flux fringing, a phenomenon in which the magnetic flux Φ flowing in a magnetic core spreads out in the surrounding medium in the air gap increasing the effective section. The total reluctance is given by

$$\mathcal{R} = \mathcal{R}_1 + \frac{1}{2} \mathcal{R}_2 = \frac{g}{\mu_0 (z + g)} \frac{2t + 3}{t^2 + 3gt + 2g^2}, \quad (5.54)$$

where \mathcal{R}_1 is the reluctance of the central branch while \mathcal{R}_2 is related to the lateral branches.

Remembering the definition of inductance, i.e.

$$L = \frac{\Phi_c}{i} = \frac{N\Psi}{\mathcal{R}i} = \frac{N^2}{\mathcal{R}} \quad (5.55)$$

where Φ_c is the concatenated flux generated by the current i flowing in the winding. Substituting (5.54) in (5.55), the following expression of the inductance value can be derived:

$$L = \frac{N^2}{\mathcal{R}} = N^2\mu_0 \frac{(z + g)(t^2 + 3gt + 2g^2)}{g(2t + 3g)}. \quad (5.56)$$

To simplify the calculation of the air-gap to achieve the desired value of inductance in (5.56), the term rational function can be rewritten as follows

$$\frac{t^2 + 3gt + 2g^2}{2t + 3g} = \frac{1}{2} \left(t + \frac{3}{2}g \right) + o(g), \quad (5.57)$$

and a closed form for g is given by

$$g^2 - \frac{2}{3} \left[\frac{2L}{N^2\mu_0} - t - \frac{3}{2}z \right] g + \frac{2}{3}tz = 0; \quad (5.58)$$

The minimum value of g can be obtained solving the second order equation: the two solutions are concordant since $tz > 0$ and they are positive if and only if $\frac{2L}{N^2\mu_0} - t - \frac{3}{2}z > 0$.

With the definition of the air-gap the geometry of E core and the arrangement of the winding are defined. The next step is the estimation of the core and winding losses. However some checks has to be done during the design iteration, for example:

- control the air-gap values to keep valid the assumption made in (5.54) imposing $g < 0.1 \max \{t, z\}$;
- limit the final temperature T_f of the inductor to T_{max} estimating T_f under the condition of air convection cooling [77]– [78]. A fast way to estimate the final temperature

is provided by the following formulas

$$h = 1.42 \left[\frac{T_{max} - T_a}{V_{box}^{1/3}} \right]^{1/4} \quad (5.59a)$$

$$T_f = \frac{P}{h V_{box}^{2/3}} + T_a \quad (5.59b)$$

where T_a is the ambient temperature, V_{box} is the total volume of the core, i.e. $V_{box} = x_{box} y_{box} z_{box}$ as depicted in Fig. 5.20, and P are the total inductor losses.

This controls permit to discard several design that are not feasible and also reduce the outcomes of the design sweep.

The core losses are differently calculated for the two inductors. The boost inductor core losses can be estimated using the Steinmetz Equation (SE) since the inductor current is approximatively sinusoidal. Instead, the ZVS inductor current is not sinusoidal so the SE can not be used. To evaluate in this case the core losses, the iGSE equation reporting in (3.7) is used. In the first case the SE equation becomes

$$P_{core} = V_{core} k f_g^\alpha \left(\frac{L_g I_g}{N A_e} \right)^\beta \quad (5.60)$$

while, in the second case, the following relations can be exploited to report (3.7) with known quantities, since

$$\frac{dB}{dt} = \frac{1}{A_e} \frac{d\Phi}{dt} = \frac{1}{N A_e} \frac{d\Phi_c}{dt} = \frac{v_L}{N A_e} = \frac{v_Z - v_C}{N A_e}, \quad (5.61)$$

in according to the definition of v_z in Table 5.3 and v_c in equations (5.38) and (5.39) for the two subintervals, and

$$\Delta B = \frac{L}{N A_e} \Delta I_L \quad (5.62)$$

where ΔI_L is equal to $2J'_M$ or $2J''_M$ or $2J_1$ depending on the instantaneous value of the duty-cycle as depicted in Fig. 5.16. Since the duty cycle varies in the grid period according to the grid voltage, the core losses in the ZVS inductor is given by average of the all integrals

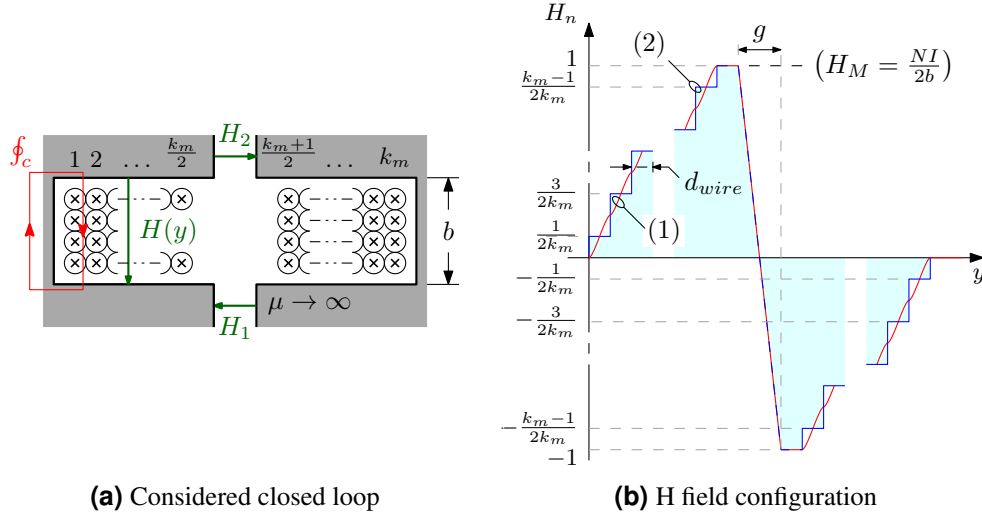


Figure 5.22: Closed line integral of the magnetic field H : (1) normalized magnetic field H_n in function of y using (5.66); (2) simplified staircase model.

in each i -th subinterval with the given duty cycle d_i as follows

$$P_{core} = V_{core} f_g \sum_{i=1}^{\frac{2f_{sw}}{f_g}} \int_0^{\frac{T_{sw}}{2}} \frac{k_i L^{\beta-\alpha}}{(NA_e)^\beta} \left[|v_Z - v_C|^\alpha \Delta I_L^{\beta-\alpha} \right]_{d_i} dt. \quad (5.63)$$

The last losses that are considered in the model are the winding losses that are dependent of the magnetic field H in the winding window due to the HF magnetic field involved. To estimate H , the closed line integral of the magnetic field has been done since it is equal to the total current crossing the surface enclosed by the line, i.e. the Ampere law. In Fig. 5.22a the considered closed loop is shown. At first, the magnetic field magnitude of H_1 and H_2 , respectively in the air gaps of the central and lateral branch of the E core, are calculated

$$H_1 = \frac{B_1}{\mu_0} = \frac{\Phi}{\mu_0 S_1} = \frac{\Psi}{\mu_0 \mathcal{R} S_1} = \frac{NI}{2g} \frac{t + 2g}{t + \frac{3}{2}g}, \quad (5.64a)$$

$$H_2 = \frac{B_2}{\mu_0} = \frac{\Phi}{2\mu_0 S_2} = \frac{\Psi}{2\mu_0 \mathcal{R} S_2} = \frac{NI}{2g} \frac{t + g}{t + \frac{3}{2}g}, \quad (5.64b)$$

that permit to define the $H(y)$ field for $y \in [0, g]$ as

$$H(y) = \frac{NI}{2b} - (H_1 + H_2)\frac{y}{b} = \frac{NI}{2b} - \frac{NI}{g} \frac{y}{b} = \frac{NI}{2b} \left[1 - \frac{2y}{g} \right]. \quad (5.65)$$

Instead, considering a uniform current distribution in the round wire, both for the stranded and Litz wires, the $H(y)$ field is defined in the k -th layer as follows:

$$H(y) = \begin{cases} \frac{n_k I}{b} \left[k + \frac{2y}{\pi d_{wire}} \sqrt{1 - \left(\frac{2y}{d_{wire}} \right)^2} - \frac{1}{\pi} \arccos \left(\frac{2y}{d_{wire}} \right) \right], & k \in \left[1, \frac{k_m}{2} \right] \\ -\frac{NI}{2b} + H(y) \Big|_{k - \frac{k_m}{2}}, & k \in \left[\frac{k_m}{2} + 1, k_m \right] \end{cases} \quad (5.66)$$

where y is defined in the interval $\left[-\frac{d_{wire}}{2}, \frac{d_{wire}}{2} \right]$ for each layer. In Fig. 5.22b the H field magnitude is depicted, normalized respect its maximum H_M . The effective resistance R_{AC} of the wire in the HF range is given by

$$R_{AC} = R_{DC}(k_s + k_{pi} + k_{pe}); \quad (5.67)$$

where R_{DC} is the resistance of the Litz wire at the final temperature of the inductor in DC condition, while k_s , k_{pi} and k_{pe} that take into account the skin effect, and the internal and external proximity effect respectively. Their values are

$$k_s = 2F_{R, str}, \quad (5.68a)$$

$$k_{pi} = \frac{1}{\pi^2 d_{wire}^2} G_{R, str} n_{str}^2, \quad (5.68b)$$

$$k_{pe} = 2G_{R, str} n_{str}^2 \sum_{k=1}^{k_m} \left(\frac{H_{rms}}{I_{rms}} \right)^2, \quad (5.68c)$$

where the function $F_{R, str}$ and $G_{R, str}$ are defined for a round Litz wire composed by n_{str}

strands of d_{str} diameter as:

$$F_R = \frac{\xi}{4\sqrt{2}} \frac{\text{ber}_0(\xi)\text{bei}_1(\xi) - \text{ber}_0(\xi)\text{ber}_1(\xi) - \text{bei}_0(\xi)\text{ber}_1(\xi) - \text{bei}_0(\xi)\text{bei}_1(\xi)}{\text{ber}_1^2(\xi) + \text{bei}_1^2(\xi)} \quad (5.69a)$$

$$G_R = \frac{\xi\pi^2 d_{str}^2}{2\sqrt{2}} \frac{\text{bei}_2(\xi)\text{ber}_1(\xi) - \text{ber}_2(\xi)\text{ber}_1(\xi) - \text{ber}_2(\xi)\text{bei}_1(\xi) - \text{bei}_2(\xi)\text{bei}_1(\xi)}{\text{ber}_0^2(\xi) + \text{bei}_0^2(\xi)} \quad (5.69b)$$

with the parameter $\xi = \frac{d_{str}}{\sqrt{2}\delta_p}$ that is dependent of the penetration depth $\delta_p = \sqrt{\frac{\rho}{\mu_0\pi f}}$ at the frequency f , and $\text{ber}_\nu(\cdot)$, $\text{bei}_\nu(\cdot)$ are the Kelvin functions. In order to compute (5.68c), the RMS values of the H field can be directly associated to the RMS value of the inductor current. To further simply the calculation, the (5.66) can be approximated with a staircase model as depicted in Fig. 5.22b, and the sum of (5.68c) is computed as

$$2 \sum_{k=1}^{\frac{k_m}{2}} \left(\frac{H_{rms}}{I_{rms}} \right)^2 = \frac{2N^2}{b^2 k_m^2} \sum_{k=1}^{\frac{k_m}{2}} \left(k - \frac{1}{2} \right)^2 = \frac{N^2}{12b^2} \frac{k_m^2 - 1}{k_m}, \quad (5.70)$$

thanks to the odd symmetry of H around the air gap.

Once the estimations of core and winding losses are defined, the design of boost and ZVS inductors can be computed, discarding the unfeasible designs. However, only the feasible inductors that present the best performance in terms of losses and volume are the interesting ones, i.e. the Pareto Front of the Inductor DS. As a demonstrative example, the Pareto Front of the ZVS Inductor for two different points of the SST DS are shown in Fig. 5.23. They represents the optimum inductors designs that could be reached with the given values of switching frequency f_{sw} , peak current I_{pk} and resonance frequency f_r of the resonant tank. Due to the multitude of parameter combinations, a detailed analysis of the MOO outcomes becomes impracticable, but a qualitative analysis of the loss allocation could be interested instead. It is worthy noting how the distribution between core losses P_{core} and the winding losses P_w differs. For the lower frequency (see Fig. 5.23a) the P_{core}/P_w ratio varies discontinuously along the Pareto Front, highlighting a wide possibility of different arrangements. The most designs of Fig. 5.23a present the winding losses greater than the core ones that could be caused by a combination of different factors, for example the increment of current density or number of turns that increase the winding re-

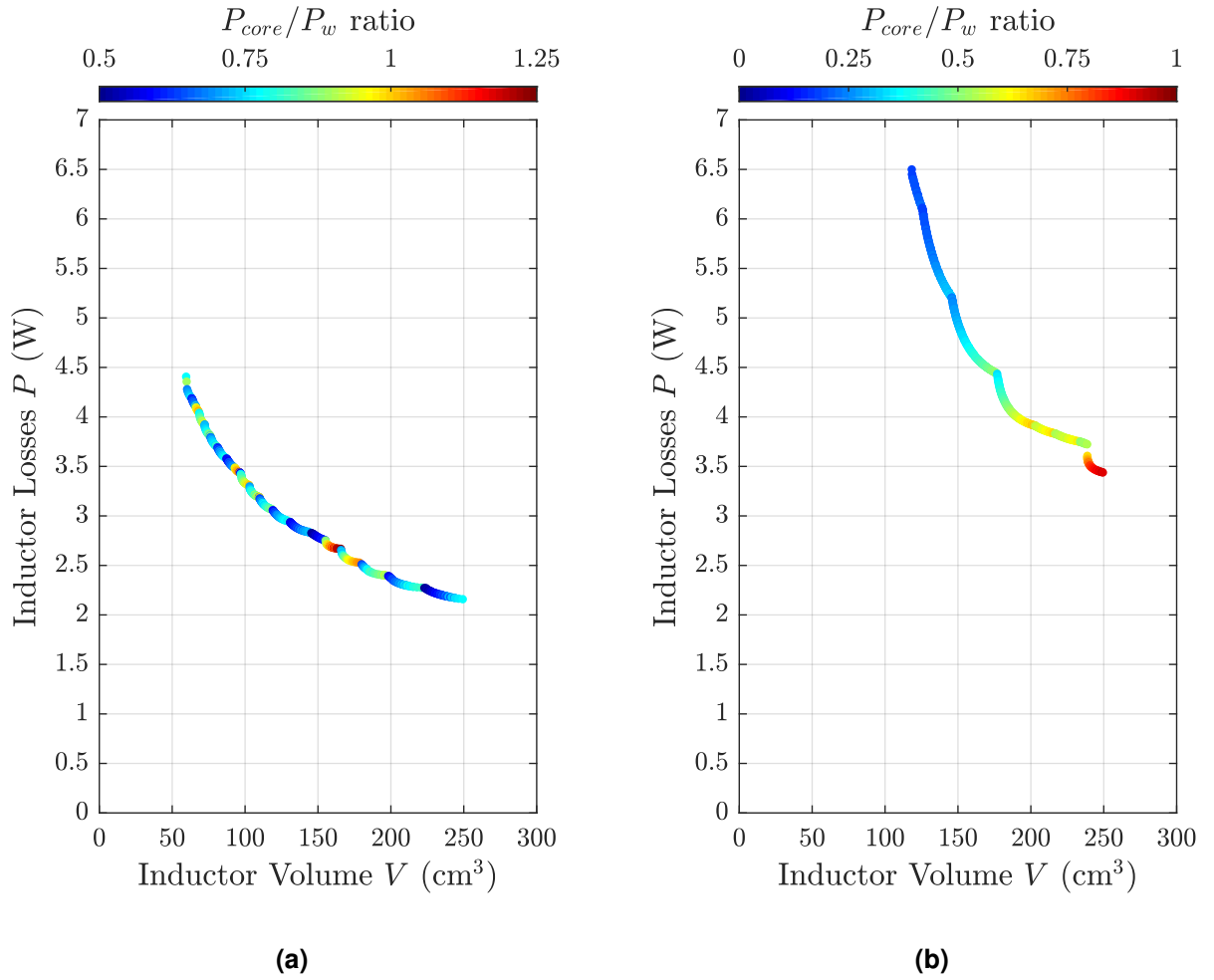


Figure 5.23: Pareto Front of ZVS Inductor design in term of losses and volume for different design space points: (a) $f_{sw} = 10\text{kHz}$, $F = 1.7$, $I_{pk} = 8\text{A}$, $L = 1.3\text{mH}$; (b) $f_{sw} = 30\text{kHz}$, $F = 1.4$, $I_{pk} = 4\text{A}$, $L = 1.1\text{mH}$.

sistance. For an intermediate frequency (see Fig. 5.23b), where the power ratio seems quite continuous indicating a defined trend between P_{core} and P_w : the smallest inductor is obtained minimizing the core losses while the most efficient inductor is given dividing the losses equally among the core and winding.

5.2.5 Thermal Management

Some considerations must be done regarding to the power dissipation of the switching devices since their thermal management could be a significant part of the total volume of the single SST cell. To take into account the quality of the thermal management system, the Cooling System Performance Index (CSPI) is defined as

$$CSPI = \frac{1}{R_{th}V_{HS}} \left(\frac{\text{kW}}{^{\circ}\text{Km}^3} \right), \quad (5.71)$$

where R_{th} is the thermal resistance showed between the heat source and the ambient, while the V_{HS} is the volume of the heatsink or the thermal management system, e.g. in case of forced air convection or liquid cooling.

From that, the volume of the heatsink is given by

$$V_{HS} = \frac{P_{sw,tot}}{(T_{HS} - T_A) CSPI}, \quad (5.72)$$

where T_{HS} and T_A are the maximum temperature of the heatsink and ambient temperature, respectively, while $P_{sw,tot}$ is the value of the overall switch losses, i.e. in the PFC case $P_{sw,tot} = 4(P_j + P_{sw})$. For SST optimization the CSPI has been set at $20\text{kW}/^{\circ}\text{Km}^3$ that is a typical value for forced air convection cooling system.

5.3 Pareto Analysis

In the previous section, the model of the PFC Boost stage in the IBE-based SST have been presented, providing all the models that are necessary to performs the Pareto Front Analysis. To remember the sweep range of the analysis, the considered variables in the

Design Space (DS) are

- Switching Frequency f_{sw} ;
- Peak Current I_{pk} in the ZVS resonant tank;
- Resonant Frequency f_r in term of the parameter $F = 2f_{sw}/f_r$;

The resulted analysis is depicted in Figs. 5.24 and 5.25. In Fig. 5.24a is shown the Pareto Front of the SST PFC Boost Stage without the proposed iTTCM solution, while in Figs. 5.24b–5.24f are shown the Pareto Fronts implementing the iTTCM solution for different switching frequencies. It is worth to note that the iTTCM solution improves the efficiency going to the detriment of the power density for switching frequency below 30kHz, instead in the upper range, the power density and the efficiency are both improved, in some case also significantly as shown in Fig. 5.24f.

Joining together all the considered designs, the final Pareto Front of the SST PFC Boost Stage with or without the iTTCM solution can be obtained as depicted in Fig. 5.25. As shown in the previous section, a detailed analysis of the MOO outcomes becomes impracticable due to the multitude of considered parameters, but a qualitative analysis of the results can be performed that was also the identified aim of this analysis. From Fig. 5.25 the main conclusion is the iTTCM solution doesn't realize the prospective benefits that were expected by the reduction of the switching losses and the increasing of the switching frequency that allows to reduce the magnetic component volume. As shown in Fig. 5.25a, the iTTCM solution provides a small efficiency improvement for low power density design. However it's interesting to note as several designs that not implement the iTTCM solution are reached by iTTCM designs at higher frequencies. Another important information that can be extracted from Fig. 5.25b is that the iTTCM works better for high values of the resonant peak current comparable with the grid current amplitude I_g . This aspect is linked to the reduction of the switching losses but, on the other hand, the increase of the RMS current value entails a volume increase in the ZVS inductor due to the thermal limits. To avoid this, a further future step could be include the analysis of the iTTCM solution with variable switching frequency in order to shape the envelope of the resonant current and reduce the RMS current value.

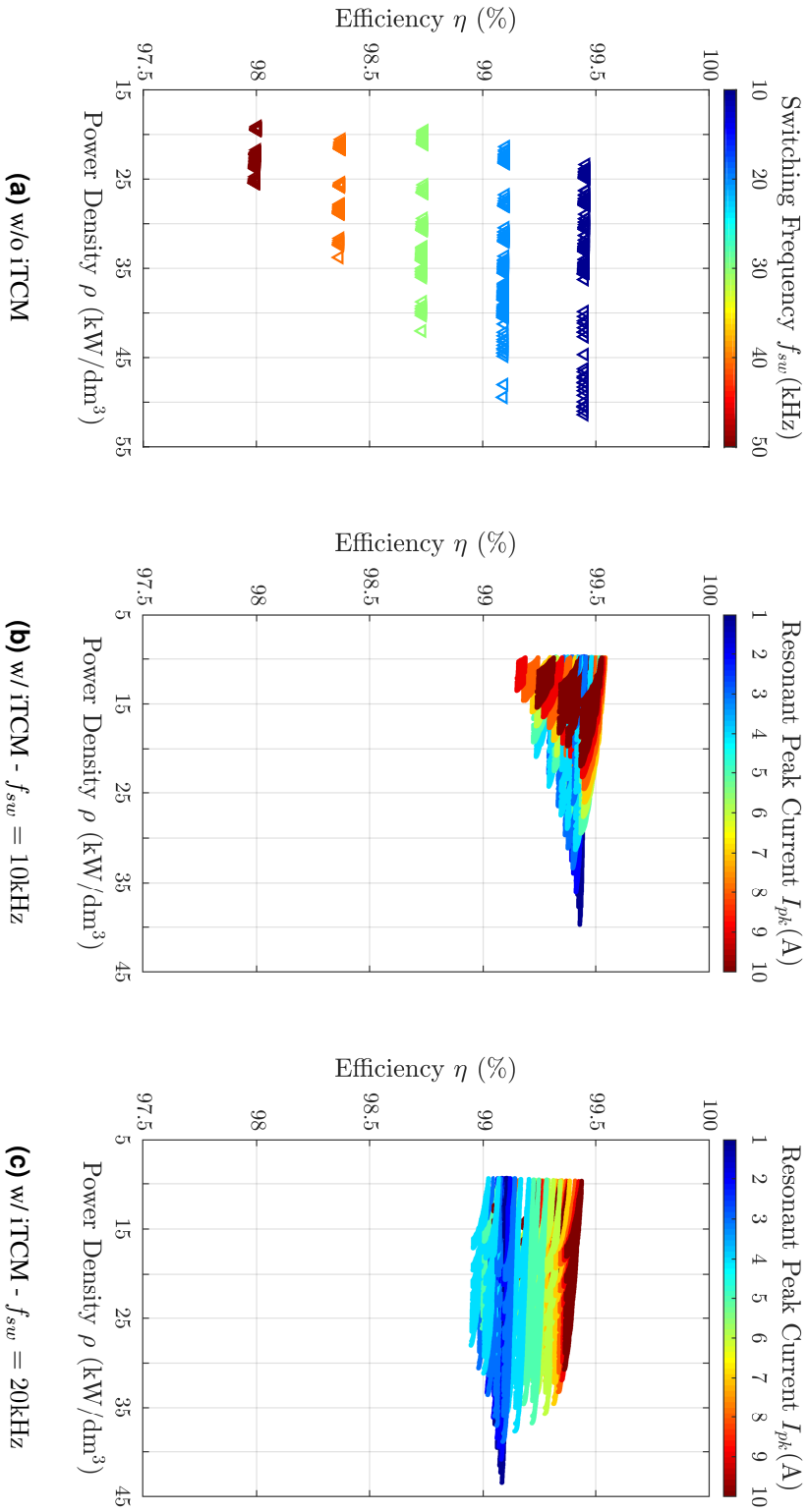


Figure 5.24: Pareto Front of overall SST PFC Boost Stage for different switching frequencies: (a) without the iTCM solution, (b)–(f) with iTCM solution at different switching frequencies.

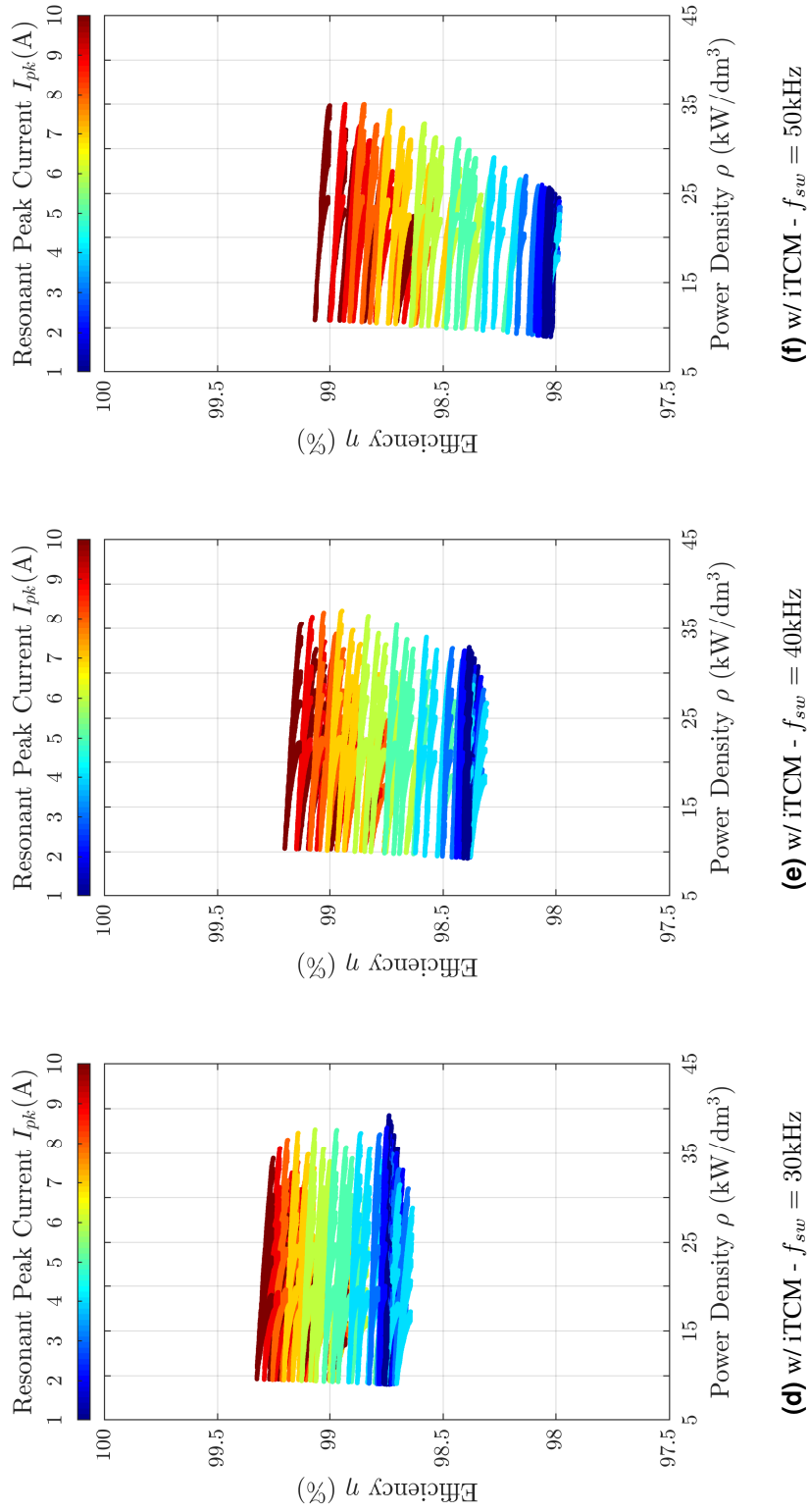
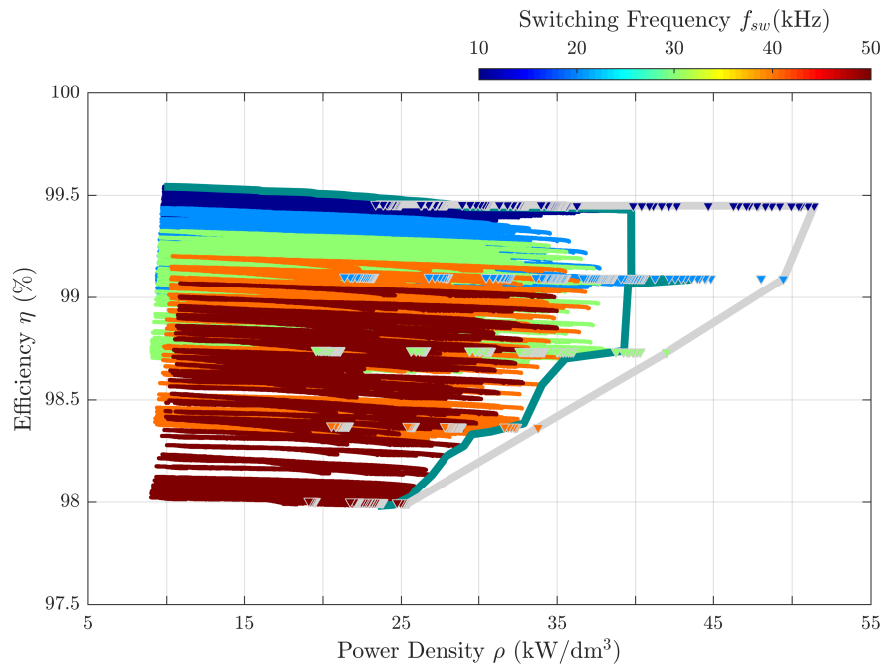
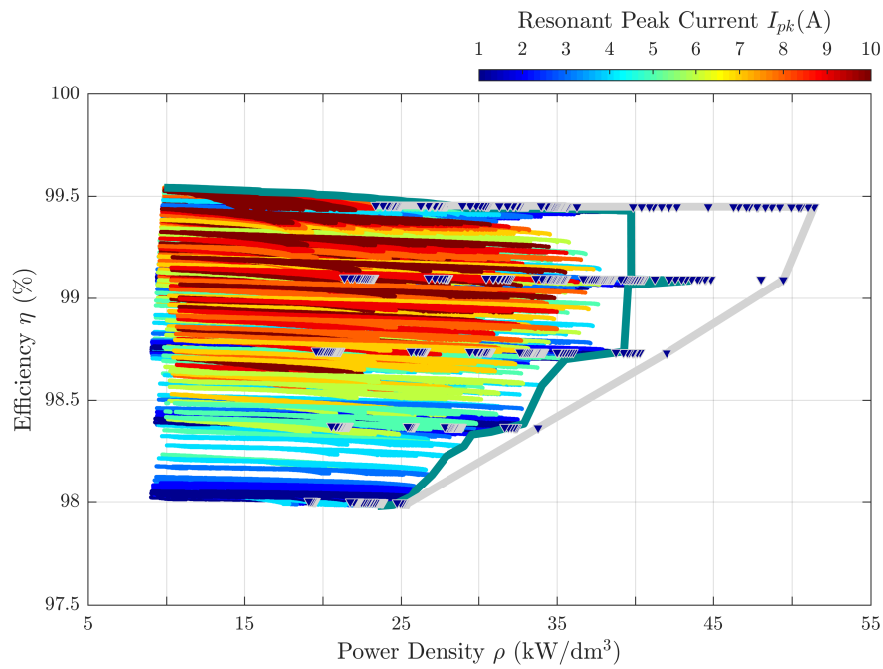


Figure 5.24: Pareto Front of overall SST PFC Boost Stage for different switching frequencies: (a) without the iTCM solution, (b)–(f) with iTCM solution at different switching frequencies.



(a)



(b)

Figure 5.25: Pareto Analysis of overall SST PFC Boost Stage: the green line is the Pareto Front of iTCM solution, while the grey one is without. The switching frequency and the resonant peak current are highlighted in (a) and (b), respectively. The ∇ indicates the designs where the iTCM is not implemented.

5.4 Summary

In this chapter, the Multi-Objective Optimization (MOO) has been applied on the PFC Boost stage in a Solid State Transformer. All the modelling stages, which are needed to deal with the MOO analysis, have been described with sufficient accuracy to provide the key points of the design process. The modulation scheme of the whole SST PFC Boost stage was described to obtain a closed form representation of the input current spectrum that permitted a fast computation of the Boost Inductance value to achieve the EMI standard constraints. Furthermore, the iTTCM solution to reduce the switching losses was taken into account and compared with the standard implementation. The Pareto Front analysis of both two solutions was implemented picking out the potential of the widespread comparison allowed by the MOO approach.

Chapter 6

Conclusions

Nowadays, the development of low-carbon energy technologies is increasingly becoming a major challenge in order to address energy security and climate change. The smart grids are being considered as possible solution as they provide several opportunities to increase the efficiency, reliability and stability of the whole system, while minimize the costs and environmental impacts. The main difference between the traditional distribution network and the smart grid is the energy generation and storage arrangement: from the large and centralized power plants present in the traditional system to a growing array of customer-sited distributed energy resources (DERs), including renewable energy sources and energy storage system in the future smart network. An important feature in the future smart grid will be the coexistence of an ICT infrastructure that is placed beside the electrical one, to control, monitor and manage the whole grid state and its agents, i.e. DERs. Therefore, a large usage of Electronic Power Converters (EPCs) is mandatory to interface and control the prospected huge amount of DERs and to connect the micro grid to the energy distribution infrastructure. Typical examples of DERs used in the described scenario include photovoltaic panels and fuel cells as energy sources, while different kinds of battery and/or supercapacitor stacks as energy storages. They are both characterized to be low voltage, high current DC devices, so they are usually connected to a common High Voltage DC bus (typically 400V) via high step-up DC/DC converters. The power transfer takes place or among the connected DERs, e.g. the available photovoltaic power is used to charge the energy storage system, or from the DC link bus to the grid through an AC/DC converter (in-

verter) or to another DC micro grid. The aim of the presented dissertation is to investigate the EPC design procedure to maximize efficiency and power density in order to achieve a deep integration of DERs in the future smart grid or, more generally, how take into account more performance indices to get more effective in the EPC design.

With that aim, the Multi-Objective Optimization (MOO) approach is proposed as useful tool to evaluate innovative solutions and comparisons with the State of Art. Without the widespread analysis provided by the MOO design, each proposed topology or solution cannot benefit of its own potentials since it is flawed by the limited information that a single design can provide.

The analysed performance indices have been the efficiency and the power density since they play a key role in many power conversion fields, e.g. automotive, power supplies, LED lighting. Because of this choice, a model for the estimation of the characteristic losses and volume for each electronic components of EPC has been found in literature. The choice of the model affects the precision in the estimation, so the target of the MOO analysis. Since this approach could be really high time- and data-consumption tool, the target was set to drive the design process and provide a first valuation.

Particular attention has been given to the Series Resonant (SR) converter class because shows many advantages, e.g. inherent short circuit protection, higher operation frequency with reduced electromagnetic interferences, soft-switching transitions of both switches and/or diodes, thus allowing to develop high-efficiency and high power-density DC-DC converters. An innovative mathematical framework that rearranges the State Plane analysis of the SR converter has been proposed to obtain the steady-state characteristic function, e.g. voltage conversion ratio and transferred power, in a single matrix formulation. This framework has allowed also the analysis of complex topologies avoiding simulation-based or approximated analysis, however, maintaining the same degree of complexity and accuracy. The validation of the proposed tool was obtained by means of both theoretical, simulation and experimental comparison.

The MOO approach has been tested through the design of the Power Factor Correction (PFC) Boost stage in a Solid State Transformer. The analysis has been used to validate the implementation of the iTTCM solution to reduce the switching losses in the switches as

it promised. The outcomes of the analysis have confirmed the efficiency improvement for high frequencies design but the proposed solution doesn't represent a crossing point of the State of Art. This analysis have also confirmed how much is important and necessary the performance estimation in the EPC design to reach innovative, high efficiency and high power density solutions.

Bibliography

- [1] D. Boroyevich, I. Cvetkovic, D. Dong, R. Burgos, F. Wang, and F. Lee, “Future electronic power distribution systems a contemplative view,” in *2010 12th International Conference on Optimization of Electrical and Electronic Equipment*. IEEE, may 2010.
- [2] I. E. Agency, “Technology roadmap - smart grids,” *OECD/IEA, Paris.*, 2011.
- [3] —, “Next generation wind and solar power: from cost to value.” *OECD/IEA, Paris.*, 2016.
- [4] Arup and S. Infrastructure, “Distributed energy system,” Siemens, Tech. Rep., 2017. [Online]. Available: www.siemens.com/intelligent-infrastructure
- [5] C. Hwang, S. Paidy, A. Masud, and K. Yoon, *Multiple Objective Decision Making Methods and Applications: A State-of-the-Art Survey*, ser. Lecture Notes in Economics and Mathematical Systems. Springer Berlin Heidelberg, 2012.
- [6] Y. Sawaragi, H. Nakayama, and T. Tanino, *Theory of Multiobjective Optimization*, ser. Mathematics in science and engineering. Academic Press, 1985.
- [7] I. Siwale, “Practical multi-objective programming,” Apex Research Ltd, Tech. Rep., 2014.
- [8] R. Marler and J. Arora, “Survey of multi-objective optimization methods for engineering,” *Structural and Multidisciplinary Optimization*, vol. 26, no. 6, pp. 369–395, apr 2004.

- [9] V. L. Vachhani, V. K. Dabhi, and H. B. Prajapati, "Survey of multi objective evolutionary algorithms," in *2015 International Conference on Circuits, Power and Computing Technologies [ICCPCT-2015]*, March 2015, pp. 1–9.
- [10] B. Xue, M. Zhang, W. N. Browne, and X. Yao, "A survey on evolutionary computation approaches to feature selection," *IEEE Transactions on Evolutionary Computation*, vol. 20, no. 4, pp. 606–626, Aug 2016.
- [11] J. W. Kolar, J. Biela, S. Waffler, T. Friedli, and U. Badstuebner, "Performance trends and limitations of power electronic systems," in *2010 6th International Conference on Integrated Power Electronics Systems*, March 2010, pp. 1–20.
- [12] H. Uemura, F. Krismer, Y. Okuma, and J. W. Kolar, " $\eta - \rho$ pareto optimization of 3-phase 3-level t-type ac-dc-ac converter comprising si and sic hybrid power stage," in *2014 International Power Electronics Conference (IPEC-Hiroshima 2014 - ECCE ASIA)*, May 2014, pp. 2834–2841.
- [13] J. Biela, U. Badstuebner, and J. W. Kolar, "Impact of power density maximization on efficiency of dc-dc converter systems," *IEEE Transactions on Power Electronics*, vol. 24, no. 1, pp. 288–300, Jan 2009.
- [14] J. W. Kolar, J. Biela, and J. Minibock, "Exploring the pareto front of multi-objective single-phase pfc rectifier design optimization - 99.2efficiency vs. 7kw/din3 power density," in *2009 IEEE 6th International Power Electronics and Motion Control Conference*, May 2009, pp. 1–21.
- [15] J. W. Kolar, T. Friedli, F. Krismer, A. Looser, M. Schweizer, R. A. Friedemann, P. K. Steimer, and J. B. Bevirt, "Conceptualization and multiobjective optimization of the electric system of an airborne wind turbine," *IEEE Journal of Emerging and Selected Topics in Power Electronics*, vol. 1, no. 2, pp. 73–103, June 2013.
- [16] J. Mühlthaler, "Modeling and multi-objective optimization of inductive power components," Ph.D. dissertation, ETH Zürich, 2012.

- [17] J. W. Kolar, U. Drofenik, J. Biela, M. L. Heldwein, H. Ertl, T. Friedli, and S. D. Round, "Pwm converter power density barriers," in *2007 Power Conversion Conference - Nagoya*, April 2007, pp. P-9-P-29.
- [18] D. Costinett, D. Maksimovic, and R. Zane, "Circuit-oriented treatment of nonlinear capacitances in switched-mode power supplies," *IEEE Transactions on Power Electronics*, vol. 30, no. 2, pp. 985-995, Feb 2015.
- [19] Y. Ren, M. Xu, J. Zhou, and F. C. Lee, "Analytical loss model of power mosfet," *IEEE Transactions on Power Electronics*, vol. 21, no. 2, pp. 310-319, March 2006.
- [20] M. Kasper, R. M. Burkart, G. Deboy, and J. W. Kolar, "Zvs of power mosfets revisited," *IEEE Transactions on Power Electronics*, vol. 31, no. 12, pp. 8063-8067, Dec 2016.
- [21] G. Bertotti, *Hysteresis in Magnetism: For Physicists, Materials Scientists, and Engineers*, ser. Academic Press series in electromagnetism. Academic Press, 1998.
- [22] J. Mccord, "Progress in magnetic domain observation by advanced magneto-optical microscopy," *Journal of Physics D: Applied Physics*, vol. 48, 08 2015.
- [23] G. Bertotti, "General properties of power losses in soft ferromagnetic materials," *IEEE Transactions on Magnetics*, vol. 24, no. 1, pp. 621-630, Jan 1988.
- [24] J. Li, T. Abdallah, and C. R. Sullivan, "Improved calculation of core loss with nonsinusoidal waveforms," in *Conference Record of the 2001 IEEE Industry Applications Conference. 36th IAS Annual Meeting (Cat. No.01CH37248)*, vol. 4, Sept 2001, pp. 2203-2210 vol.4.
- [25] J. Reinert, A. Brockmeyer, and R. W. A. A. D. Doncker, "Calculation of losses in ferro- and ferrimagnetic materials based on the modified steinmetz equation," *IEEE Transactions on Industry Applications*, vol. 37, no. 4, pp. 1055-1061, Jul 2001.
- [26] K. Venkatachalam, C. R. Sullivan, T. Abdallah, and H. Tacca, "Accurate prediction of ferrite core loss with nonsinusoidal waveforms using only steinmetz parameters," in

- 2002 *IEEE Workshop on Computers in Power Electronics, 2002. Proceedings.*, June 2002, pp. 36–41.
- [27] A. P. V. den Bossche, D. M. V. de Sype, and V. C. Valchev, “Ferrite loss measurement and models in half bridge and full bridge waveforms,” in *2005 IEEE 36th Power Electronics Specialists Conference*, June 2005, pp. 1535–1539.
- [28] J. B. Goodenough, “Summary of losses in magnetic materials,” *IEEE Transactions on Magnetics*, vol. 38, no. 5, pp. 3398–3408, Sep 2002.
- [29] J. Muhlethaler, J. Biela, J. W. Kolar, and A. Ecklebe, “Improved core-loss calculation for magnetic components employed in power electronic systems,” *IEEE Transactions on Power Electronics*, vol. 27, no. 2, pp. 964–973, Feb 2012.
- [30] W. Roshen, “Ferrite core loss for power magnetic components design,” *IEEE Transactions on Magnetics*, vol. 27, no. 6, pp. 4407–4415, Nov 1991.
- [31] A. A. Adly and I. D. Mayergoyz, “Accurate modeling of vector hysteresis using a superposition of preisach-type models,” *IEEE Transactions on Magnetics*, vol. 33, no. 5, pp. 4155–4157, Sep 1997.
- [32] X. Nan and C. R. Sullivan, “An improved calculation of proximity-effect loss in high-frequency windings of round conductors,” in *Power Electronics Specialist Conference, 2003. PESC '03. 2003 IEEE 34th Annual*, vol. 2, June 2003, pp. 853–860 vol.2.
- [33] J. A. Ferreira, “Improved analytical modeling of conductive losses in magnetic components,” *IEEE Transactions on Power Electronics*, vol. 9, no. 1, pp. 127–131, Jan 1994.
- [34] J. Lammeraner and M. Štafl, *Eddy currents*, ser. International scientific series. CRC Press, 1966.
- [35] I. Jitaru, “A 3 kw soft switching dc-dc converter,” in *Applied Power Electronics Conference and Exposition, 2000. APEC 2000. Fifteenth Annual IEEE*, vol. 1, 2000, pp. 86–92 vol.1.

- [36] F. Krismer and J. Kolar, "Closed form solution for minimum conduction loss modulation of dab converters," *Power Electronics, IEEE Transactions on*, vol. 27, no. 1, pp. 174–188, Jan 2012.
- [37] H. Bai and C. Mi, "Eliminate reactive power and increase system efficiency of isolated bidirectional dual-active-bridge dc-dc converters using novel dual-phase-shift control," *Power Electronics, IEEE Transactions on*, vol. 23, no. 6, pp. 2905–2914, Nov 2008.
- [38] ———, "Correction to "eliminate reactive power and increase system efficiency of isolated bidirectional dual-active-bridge dc-dc converters using novel dual-phase-shift control" [nov 08 2905-2914]," *IEEE Transactions on Power Electronics*, vol. 27, no. 9, pp. 4177–4177, Sept 2012.
- [39] L. Cao, K. Loo, and Y. Lai, "Output-impedance shaping of bidirectional dab dc-dc converter using double-proportional-integral feedback for near-ripple-free dc bus voltage regulation in renewable energy systems," *Power Electronics, IEEE Transactions on*, vol. 31, no. 3, pp. 2187–2199, March 2016.
- [40] W. Choi, K.-M. Rho, and B.-H. Cho, "Fundamental duty modulation of dual-active-bridge converter for wide-range operation," *Power Electronics, IEEE Transactions on*, vol. 31, no. 6, pp. 4048–4064, June 2016.
- [41] J. Everts, F. Krismer, J. Van den Keybus, J. Driesen, and J. Kolar, "Optimal zvs modulation of single-phase single-stage bidirectional dab ac-dc converters," *Power Electronics, IEEE Transactions on*, vol. 29, no. 8, pp. 3954–3970, Aug 2014.
- [42] F. Krismer and J. Kolar, "Efficiency-optimized high-current dual active bridge converter for automotive applications," *Industrial Electronics, IEEE Transactions on*, vol. 59, no. 7, pp. 2745–2760, July 2012.
- [43] B. Farhangi and H. Toliyat, "Piecewise linear model for snubberless dual active bridge commutation," *Industry Applications, IEEE Transactions on*, vol. 51, no. 5, pp. 4072–4078, Sept 2015.

- [44] S. J. Jang, C. Y. Won, B. K. Lee, and J. Hur, "Fuel cell generation system with a new active clamping current-fed half-bridge converter," *IEEE Transactions on Energy Conversion*, vol. 22, no. 2, pp. 332–340, June 2007.
- [45] G. Spiazzi and S. Buso, "Analysis of the interleaved isolated boost converter with coupled inductors," *Industrial Electronics, IEEE Transactions on*, vol. 62, no. 7, pp. 4481–4491, July 2015.
- [46] Y. Zhao, W. Li, Y. Deng, and X. He, "Analysis, design, and experimentation of an isolated zvt boost converter with coupled inductors," *Power Electronics, IEEE Transactions on*, vol. 26, no. 2, pp. 541–550, Feb 2011.
- [47] W. Li, L. Fan, Y. Zhao, X. He, D. Xu, and B. Wu, "High-step-up and high-efficiency fuel-cell power-generation system with active-clamp flyback-forward converter," *Industrial Electronics, IEEE Transactions on*, vol. 59, no. 1, pp. 599–610, Jan 2012.
- [48] Y. Zhao, X. Xiang, W. Li, X. He, and C. Xia, "Advanced symmetrical voltage quadrupler rectifiers for high step-up and high output-voltage converters," *Power Electronics, IEEE Transactions on*, vol. 28, no. 4, pp. 1622–1631, April 2013.
- [49] W. Li, H. Wu, H. Yu, and X. He, "Isolated winding-coupled bidirectional zvs converter with pwm plus phase-shift (pps) control strategy," *Power Electronics, IEEE Transactions on*, vol. 26, no. 12, pp. 3560–3570, Dec 2011.
- [50] X. Sun, X. Wu, Y. Shen, X. Li, and Z. Lu, "A current-fed isolated bidirectional dc-dc converter," *IEEE Transactions on Power Electronics*, vol. 32, no. 9, pp. 6882–6895, Sept 2017.
- [51] F. Z. Peng, H. Li, G.-J. Su, and J. S. Lawler, "A new zvs bidirectional dc-dc converter for fuel cell and battery application," *IEEE Transactions on Power Electronics*, vol. 19, no. 1, pp. 54–65, Jan 2004.
- [52] X. Li and A. K. S. Bhat, "Analysis and design of high-frequency isolated dual-bridge series resonant dc/dc converter," *IEEE Transactions on Power Electronics*, vol. 25, no. 4, pp. 850–862, April 2010.

- [53] J. Kan, S. Xie, Y. Tang, and Y. Wu, "Voltage-fed dual active bridge bidirectional dc/dc converter with an immittance network," *Power Electronics, IEEE Transactions on*, vol. 29, no. 7, pp. 3582–3590, July 2014.
- [54] R. Twinaime, D. Thrimawithana, U. Madawala, and C. Baguley, "A new resonant bidirectional dc-dc converter topology," *Power Electronics, IEEE Transactions on*, vol. 29, no. 9, pp. 4733–4740, Sept 2014.
- [55] A. A. Aboushady, K. H. Ahmed, S. J. Finney, and B. W. Williams, "Steady-state analysis of full-bridge series resonant converter with phase-shift and frequency control," in *5th IET International Conference on Power Electronics, Machines and Drives (PEMD 2010)*, April 2010, pp. 1–6.
- [56] L. Corradini, D. Seltzer, D. Bloomquist, R. Zane, D. Maksimovic, and B. Jacobson, "Minimum current operation of bidirectional dual-bridge series resonant dc/dc converters," *IEEE Transactions on Power Electronics*, vol. 27, no. 7, pp. 3266–3276, July 2012.
- [57] F. Martin Ibanez, J. Martin Echeverria, J. Vadillo, and L. Fontan, "A step-up bidirectional series resonant dc/dc converter using a continuous current mode," *Power Electronics, IEEE Transactions on*, vol. 30, no. 3, pp. 1393–1402, March 2015.
- [58] F. Ibanez, J. M. Echeverria, and L. Fontan, "Novel technique for bidirectional series-resonant dc/dc converter in discontinuous mode," *IET Power Electronics*, vol. 6, no. 5, pp. 1019–1028, May 2013.
- [59] B. S. Nathan and V. Ramanarayanan, "Analysis, simulation and design of series resonant converter for high voltage applications," in *Proceedings of IEEE International Conference on Industrial Technology 2000 (IEEE Cat. No.00TH8482)*, vol. 1, Jan 2000, pp. 688–693 vol.2.
- [60] A. Safaee, P. Jain, and A. Bakhshai, "Time-domain steady-state analysis of fixed-frequency series resonant converters with phase-shift modulation," in *2014 IEEE Transportation Electrification Conference and Expo (ITEC)*, June 2014, pp. 1–7.

- [61] A. Safaee, M. Karimi-Ghartemani, P. K. Jain, and A. Bakhshai, "Time-domain analysis of a phase-shift-modulated series resonant converter with an adaptive passive auxiliary circuit," *IEEE Transactions on Power Electronics*, vol. 31, no. 11, pp. 7714–7734, Nov 2016.
- [62] F. M. Ibanez, J. M. Echeverria, J. Vadillo, and L. Fontan, "State-plane analysis of anomalous step-up behavior in series-resonant converters," *IEEE Journal of Emerging and Selected Topics in Power Electronics*, vol. 4, no. 3, pp. 1026–1035, Sept 2016.
- [63] J.-M. Kwon and B.-H. Kwon, "High step-up active-clamp converter with input-current doubler and output-voltage doubler for fuel cell power systems," *Power Electronics, IEEE Transactions on*, vol. 24, no. 1, pp. 108–115, Jan 2009.
- [64] J.-M. Kwon, K. Eung-Ho, B.-H. Kwon, and K.-H. Nam, "High-efficiency fuel cell power conditioning system with input current ripple reduction," *Industrial Electronics, IEEE Transactions on*, vol. 56, no. 3, pp. 826–834, March 2009.
- [65] G. Spiazzi, F. Sichirollo, and F. Goncalves, "Efficiency analysis of an isolated high voltage gain converter operating in resonant and non-resonant mode," in *Energy Conversion Congress and Exposition (ECCE), 2012 IEEE*, Sept 2012, pp. 3875–3881.
- [66] J. Hiltunen, V. Visnen, and P. Silventoinen, "A bidirectional current-fed resonant push-pull converter for low voltage, high current applications," in *2013 IEEE Energy Conversion Congress and Exposition*, Sept 2013, pp. 4770–4774.
- [67] Y. Li, Y. Xing, Y. Lu, H. Wu, and P. Xu, "Performance analysis of a current-fed bidirectional llc resonant converter," in *IECON 2016 - 42nd Annual Conference of the IEEE Industrial Electronics Society*, Oct 2016, pp. 2486–2491.
- [68] R. L. Steigerwald, "A comparison of half-bridge resonant converter topologies," in *1987 2nd IEEE Applied Power Electronics Conference and Exposition*, March 1987, pp. 135–144.

- [69] G. Spiazzi, S. Buso, and D. Biadene, "Efficient high step-up topology for renewable energy source interfacing," in *2015 IEEE Applied Power Electronics Conference and Exposition (APEC)*, March 2015, pp. 1137–1144.
- [70] Y. Kashihara, Y. Nemoto, W. Qichen, S. Fujita, R. Yamada, and Y. Okuma, "An isolated medium-voltage ac/dc power supply based on multil-cell converter topology," in *2017 IEEE Applied Power Electronics Conference and Exposition (APEC)*, March 2017, pp. 2187–2192.
- [71] S. Zhao, Q. Li, and F. C. Lee, "High frequency transformer design for modular power conversion from medium voltage ac to 400v dc," in *2017 IEEE Applied Power Electronics Conference and Exposition (APEC)*, March 2017, pp. 2894–2901.
- [72] J. E. Huber and J. W. Kolar, "Solid-state transformers: On the origins and evolution of key concepts," *IEEE Industrial Electronics Magazine*, vol. 10, no. 3, pp. 19–28, Sept 2016.
- [73] H. Asai, I. Nashiyama, K. Sugimoto, K. Shiba, Y. Sakaide, Y. Ishimaru, Y. Okazaki, K. Noguchi, and T. Morimura, "Tolerance against terrestrial neutron-induced single-event burnout in sic mosfets," *IEEE Transactions on Nuclear Science*, vol. 61, no. 6, pp. 3109–3114, Dec 2014.
- [74] D. Holmes and T. Lipo, *Pulse Width Modulation for Power Converters: Principles and Practice*, ser. IEEE Press Series on Power Engineering. John Wiley & Sons, 2003. [Online]. Available: <https://books.google.it/books?id=8LGi1AjSfpcC>
- [75] M. van der Berg and J. A. Ferreira, "A family of low emi, unity power factor converters," in *PESC Record. 27th Annual IEEE Power Electronics Specialists Conference*, vol. 2, Jun 1996, pp. 1120–1127 vol.2.
- [76] D. Zhang, D. Y. Chen, and F. C. Lee, "An experimental comparison of conducted emi emissions between a zero-voltage transition circuit and a hard switching circuit," in *PESC Record. 27th Annual IEEE Power Electronics Specialists Conference*, vol. 2, Jun 1996, pp. 1992–1997 vol.2.

- [77] W. Hurley and W. Wölfle, *Transformers and Inductors for Power Electronics: Theory, Design and Applications*, ser. EngineeringPro collection. Wiley, 2013.
- [78] W. G. Hurley, W. H. Wolfle, and J. G. Breslin, “Optimized transformer design: inclusive of high-frequency effects,” *IEEE Transactions on Power Electronics*, vol. 13, no. 4, pp. 651–659, Jul 1998.